



KTH ROYAL INSTITUTE  
OF TECHNOLOGY

Doctoral Thesis in Information and Communication Technology

# Spintronic and Electronic Oscillators for Magnetic Field Sensing and Ising Machines

DAGUR INGI ALBERTSSON

# **Spintronic and Electronic Oscillators for Magnetic Field Sensing and Ising Machines**

**DAGUR INGI ALBERTSSON**

Academic Dissertation which, with due permission of the KTH Royal Institute of Technology,  
is submitted for public defence for the Degree of Doctor of Philosophy on Monday the 12th June  
2023, at 13:00 in Sal C, Electrum, Kistagången 16, Kista.

Doctoral Thesis in Information and Communication Technology  
KTH Royal Institute of Technology  
Stockholm, Sweden 2023

© Dagur Ingi Albertsson  
© Paper I, Mohammad Zahedinejad, Johan Åkerman, Saul Rodriguez, Ana Rusu  
© Paper II, Johan Åkerman, Ana Rusu  
© Paper III, Mohammad Zahedinejad, Afshin Houshang, Roman Khymyn, Johan Åkerman, Ana Rusu  
© Paper IV, Ana Rusu  
© Paper V, Ana Rusu

ISBN 978-91-8040-592-8  
TRITA-EECS-AVL-2023:45

Printed by: Universitetsservice US-AB, Sweden 2023

## Abstract

Oscillators can exhibit a range of complex dynamics which are often encountered in nature. These characteristics include synchronization, injection locking, chaos, bifurcations, etc. To date, the applications of electronic oscillators has mostly been limited to communication systems. However, in recent years, the possibility of using the rich dynamics of oscillators in unconventional applications, including time-based information processing and computational applications, has been also explored. In this thesis, this potential is investigated using emerging spintronic oscillators and established electronic oscillators.

The first part of this thesis targets emerging spintronic oscillators, which exhibit a range of attractive features, including GHz operating frequency, wide tunability and nanoscale size. To explore the potential of these devices, an electrical behavioural model was developed for the promising three-terminal spin-Hall nano-oscillator. The behavioural model is based on the macrospin approximation, which is commonly used to describe the operation principles of spintronic oscillators, and it was implemented in Verilog-A. Moreover, the behavioural model was verified against experimental measurements from literature, demonstrating that the most important characteristics of three-terminal spin-Hall nano-oscillators are accurately captured. Subsequently, two potential applications that could benefit from the unique characteristics of spintronic oscillators were identified and explored. First, a magnetic field sensing system, which takes advantage of the wide frequency tunability of spintronic oscillators as a function of externally applied magnetic field, was proposed and demonstrated. This sensing system, inspired by voltage-controlled oscillator analog-to-digital converters, shows performance similar to the state-of-the-art magnetic field sensors, making it a promising application for spintronic oscillators. Next, the possibility of utilizing spintronic oscillators to realize Ising machines (IMs) was explored and demonstrated with numerical simulations. This was the first-time demonstration of spintronic oscillator-based Ising machines. The numerical simulation results show that spintronic oscillators are a promising device to realize ultra-fast Ising Machines able to solve complex combinatorial optimization problems on nano-second time scale.

The second part of the thesis extends on the idea of oscillator-based IMs, but using electronic oscillators. The potential of realizing highly reconfigurable oscillator-based IMs based on quasiperiodically modulated coupling was explored. The advantages and potential challenges associated with this approach were highlighted, and a proof-of-concept IM using CMOS ring oscillators was proposed and simulated. Finally, a completely new type of IMs based on bifurcations in a network of coupled Duffing oscillators was proposed and developed. This work highlights a new research direction based on using dynamical systems implemented with analog circuits to realize IMs.

**Keywords:** Spintronic Oscillator, Behavioural Modeling, Macrospin Approximation, Magnetic Field Sensor, Ising Machine, Duffing Oscillator, Kuramoto Model.

## Sammanfattning

Oscillatorer har en mycket rik och komplex dynamik som ofta kan observeras i naturen. Dessa egenskaper inkluderar synkronisering, injektionslåsning, kaos, bifurkationer, etc. Hittills har tillämpningarna av elektroniska oscillatorer mestadels varit begränsade till kommunikationssystem. Under senare år har möjligheten att utnyttja oscillatorernas rika dynamik i okonventionella tillämpningar inklusive tidsbaserad informationsbehandling och för beräkningstillämpningar undersökts. I denna avhandling utforskas denna potential både med hjälp av nya spintroniska oscillatorer och etablerade elektro-niska oscillatorer.

Den första delen av avhandlingen är inriktad på framväxande spintroniska oscillatorer, som har en rad attraktiva egenskaper, inklusive GHz-frekvenser, bred avstämbarhet och storlek i nano-skala. För att utforska potentialen hos dessa oscillatorer utvecklades en elektrisk modell för den lovande tre-terminals spin-Hall nano-oscillatoren. Modellen är baserad på makrospin-approximationen, som vanligtvis används för att beskriva den principiella funktionen av spintroniska oscillatorer, och den implementerades i Verilog-A. Dessutom verifierades modellen mot experimentella mätningar från litteraturen, vilket visar att modellen kan beskriva de viktigaste egenskaperna hos tre-terminala spin-Hall nano-oscillatorer. Därefter identifierades och utforskades två potentiella tillämpningar som kan dra nytta av de unika egenskaperna hos spintroniska oscillatorer. Först föreslogs ett magnetfälts-avkänningssystem, baserat på den breda frekvensavstämningen hos spintroniska oscillatorer som en funktion av externt applicerat magnetfält. Systemet är inspirerat av spänningsstyrda oscillatorer analog-till-digital-omvandlare och kan ge fördelar jämfört med andra tillvägagångssätt. Därefter undersöktes möjligheten att använda spintroniska oscillatorer för att realisera oscillator-baserade Ising-maskiner (IMs) och detta demonstrerades med simuleringar. IM är hårdvaruarkitekturen som specifikt inriktar sig på svåra kombinatoriska optimeringsproblem, som är utmanande att lösa på den konventionella von-Neumann arkitekturen.

Den andra delen av avhandlingen utvidgar idén om oscillator-baserade IM, men med hjälp av elektroniska oscillatorer. Potentialen med att realisera mycket konfigurerbara oscillator-IMs baserade på kvasiperiodiskt modulerad koppling undersöktes. Fördelarna och de potentiella utmaningarna med detta tillvägagångssätt lyftes fram, och en proof-of-concept IM med CMOS-ring oscillatorer föreslogs och simulerades. Slutligen föreslogs och utvecklades en ny typ av IM baserade på bifurkationer i ett nätverk av kopplade Duffing-oscillatorer.

# Acknowledgements

First and foremost, I would like to thank my main supervisor, Prof. Ana Rusu for giving me the opportunity to work on this thesis within her group. I am deeply grateful for all of her guidance, research advice and continuous support during the last couple of years. The last five years have undoubtedly been the most challenging years of my career but she has always supported me and been extremely patient and professional. I have grown both personally and professionally by having the opportunity to work with her and without her guidance, this thesis would not have been possible.

I would also like to acknowledge my co-supervisor Prof. Johan Åkerman for valuable discussions and research input. Additionally, I would like to thank him for allowing me to visit his group at Gothenburg University.

I gratefully acknowledge the Swedish Research Council (VR), projects 2016-05980 and 2022-02990, for financially supporting my research.

A big thank you goes to my former office mate Dr. Panagiotis Chaourani who was a massive source of advice during my first year. Also, to my current office mate and good friend, thank you Alejandro Fernandez Schrunder for all the valuable discussions and suggestions over the years. I could always rely on you for a good laugh even during very challenging times. I would also like thank all the current and former members of the Mixed-Signal Integrated Circuits and Systems group during my time there, Assoc. Prof. Saul Rodriguez, Yu-Kai Huang, Dr. Nikola Ivanisevic and Dr. Muhammad Waqar for all our discussions and input. Additionally, I would like to thank Dr. Tingsu Chen for laying the foundation of my work and Dr. Mohammad Zahedinejad for our discussions and helpful advice on spintronic oscillators. I would also like to thank my other co-authors Dr. Afshin Houshang and Dr. Roman Khymyn for our discussions on spintronic oscillators and Ising machines.

My sincerest gratitude goes to Prof. Carl-Mikael Zetterling, the head of EES division, for creating a great working environment and helping with logistics. To my other friends and colleagues in Kista. Corrado Carlo Maria Capriata, Viktoriia Mishukova, Alexey Metreveli, Dr. Laura Zurauskaite, Dr. Ahmad Abedin, Dr. Dimitrios Stathis, Dr. Yu Yang, Zimo Yuan and Dr. Mattias Ekström, thank you all for the fun discussions and lunch breaks.

My appreciation also goes to my close friends in Sweden. Rúnar, Dr. Pia De-

sai, Alexander, Louise, Hergils and Liljar, thank you for your continuous encouragement and support. You have certainly made my time in Sweden memorable.

A huge appreciation goes to my girlfriend, Rakel Ósk who has been extremely patient and understanding. Thank you for all our late night discussions and for tolerating me throughout this period, even-though it might have been challenging at times.

Last but certainly not least, I would like to thank my parents, my brother and my parents-in-law. My deepest gratitude goes to all of them, but specifically my parents for continuously supporting and helping me. This would not have been possible without your immense amount of help.

# Contents

<b>Contents</b>	<b>v</b>
<b>List of Acronyms</b>	<b>vii</b>
<b>List of Publications</b>	<b>ix</b>
<b>Summary of Appended Papers</b>	<b>xi</b>
<b>1 Introduction</b>	<b>1</b>
1.1 Beyond Conventional Oscillators and their Applications . . . . .	3
1.2 Motivation . . . . .	6
1.3 Research Objectives . . . . .	6
1.4 Research Contributions . . . . .	7
1.5 Thesis Organization . . . . .	7
<b>2 Spintronic Oscillators - Modelling and Applications</b>	<b>9</b>
2.1 Spintronic Oscillators . . . . .	9
2.1.1 Magnetoresistance . . . . .	10
2.1.2 Operation of STNOs and SHNOs . . . . .	12
2.1.3 State-of-the-Art Spintronic Oscillators and Applications . . .	14
2.2 Modeling of Three-terminal SHNOs . . . . .	15
2.2.1 Universal Auto-oscillator . . . . .	17
2.2.2 Effective Magnetic Field . . . . .	18
2.2.3 DC Operating Point . . . . .	19
2.2.4 Operating Frequency . . . . .	20
2.2.5 Output Power . . . . .	21
2.2.6 Linewidth . . . . .	22
2.2.7 Verilog Implementation and Cadence Simulation Results . . .	23
2.2.8 Limitations and Future Work . . . . .	25
2.3 Magnetic Field-to-Digital Conversion using Spintronic Oscillators .	25
2.3.1 Magnetic Field Sensors . . . . .	26
2.3.2 Spintronic Oscillators as Magnetic Field Sensors . . . . .	28
2.3.3 VCO-based ADCs . . . . .	29

2.3.4	Proposed Implementation and Simulation Results . . . . .	31
2.3.5	Limitation and Future Work . . . . .	35
<b>3</b>	<b>Ising Machines using Networks of Coupled Oscillators</b>	<b>37</b>
3.1	Ising Machines . . . . .	38
3.1.1	Optimization Problems . . . . .	38
3.1.2	Ising Model . . . . .	39
3.1.3	State-of-the-Art Ising Machines . . . . .	41
3.1.4	Coupled Kuramoto Oscillators . . . . .	45
3.1.5	Second Harmonic Injection Locking . . . . .	47
3.1.6	Oscillator-based Ising Machines . . . . .	49
3.2	Spintronic Oscillator-based Ising Machine . . . . .	51
3.2.1	Impact of Nonlinearity on the Phase Dynamics of Coupled Spintronic Oscillators . . . . .	52
3.2.2	Numerical Simulation Approach . . . . .	54
3.2.3	Simulation Results . . . . .	54
3.2.4	Limitations and Future Work . . . . .	58
3.3	Reconfigurable Ring Oscillator-based Ising Machine . . . . .	58
3.3.1	Proposed Architecture . . . . .	59
3.3.2	Comparison with Conventional Oscillator-based IMs . . . . .	61
3.3.3	Weighted Graphs . . . . .	64
3.3.4	Scalability . . . . .	65
3.3.5	Proof-of-Concept, Limitations and Future Work . . . . .	67
3.4	Duffing Oscillator-based Ising Machines . . . . .	67
3.4.1	Duffing Oscillators . . . . .	68
3.4.2	Simulated Bifurcation . . . . .	70
3.4.3	Analog Circuit Implementation of Duffing Oscillators . . . . .	72
3.4.4	Proof-of-Concept Prototype and Experimental Results . . . . .	75
3.4.5	Limitations and Future Work . . . . .	80
<b>4</b>	<b>Conclusions and Future Work</b>	<b>81</b>
<b>References</b>		<b>85</b>

# List of Acronyms

List of commonly used acronyms:

<b>ADC</b>	Analog-to-Digital Converter
<b>AFM</b>	AntiFerroMagnetic
<b>AMR</b>	Anisotropic MagnetoResistance
<b>ASIC</b>	Application Specific Integrated Circuit
<b>CIM</b>	Coherent Ising Machine
<b>CMOS</b>	Complementary Metal-Oxide Semiconductor
<b>CO</b>	Combinatorial Optimization
<b>DE</b>	Differential Equation
<b>DOPO</b>	Degenerate Optical Parametric Oscillators
<b>EDA</b>	Electronic Design Automation
<b>FFT</b>	Fast Fourier Transform
<b>FM</b>	FerroMagnetic
<b>FPGA</b>	Field Programmable Gate Array
<b>GMR</b>	Giant MagnetoResistance
<b>GMI</b>	Giant MagnetoImpedance
<b>GPU</b>	Graphics Processing Unit
<b>HM</b>	Heavy Metal
<b>IC</b>	Integrated Circuit
<b>IM</b>	Ising Machine
<b>IoT</b>	Internet-of-Things
<b>LNA</b>	Low-Noise Amplifier

<b>MC</b>	Monte Carlo
<b>MR</b>	MagnetoResistance
<b>MRAM</b>	Magnetic Random-Access Memory
<b>MTJ</b>	Magnetic Tunnel Junction
<b>NP</b>	Nondeterministic Polynomial
<b>PSD</b>	Power-Spectral-Density
<b>RF</b>	Radio Frequency
<b>SA</b>	Simulated Annealing
<b>SB</b>	Simulated Bifurcation
<b>SHE</b>	Spin-Hall Effect
<b>SHIL</b>	Second Harmonic Injection Locking
<b>SHNO</b>	Spin-Hall Nano-Oscillators
<b>SNDR</b>	Signal-to-Noise and Distortion Ratio
<b>SNR</b>	Signal-to-Noise Ratio
<b>SQNR</b>	Signal-to-Quantization Noise Ratio
<b>STNO</b>	Spin-Torque Nano-Oscillator
<b>STT</b>	Spin-Transfer Torque
<b>TMR</b>	Tunneling MagnetoResistance
<b>TSP</b>	Traveling Salesman Problem
<b>VCO</b>	Voltage-Controlled Oscillator

# List of Publications

## Appended Papers

- I D. I. Albertsson, M. Zahedinejad, J. Åkerman, S. Rodriguez and A. Rusu, "Compact Macrospin-Based Model of Three-Terminal Spin-Hall Nano Oscillators," in *IEEE Transactions on Magnetics*, vol. 55, no. 10, Oct. 2019.
- II D. I. Albertsson, J. Åkerman and A. Rusu, "A Magnetic Field-to-Digital Converter Employing a Spin-Torque Nano-Oscillator," in *IEEE Transactions on Nanotechnology*, vol. 19, pp. 565-570, July 2020.
- III D. I. Albertsson, M. Zahedinejad, A. Houshang, R. Khymyn, J. Åkerman, and A. Rusu , "Ultrafast Ising Machines using spin torque nano-oscillators", in *Appl. Phys. Lett.* 118, 112404, March 2021.
- IV D. I. Albertsson, and A. Rusu, "Highly Reconfigurable Oscillator-Based Ising Machine Through Quasiperiodic Modulation of Coupling Strength", in *Sci Rep* 13, 4005, March 2023.
- V D. I. Albertsson, and A. Rusu , "Ising Machine Based on Bifurcations in a Network of Duffing Oscillators", *IEEE International Symposium on Circuits and Systems (ISCAS)*, Monterey, CA, USA, May 2023.



# Summary of Appended Papers

- [Paper I] D. I. Albertsson, M. Zahedinejad, J. Åkerman, S. Rodriguez and A. Rusu, "Compact Macrospin-Based Model of Three-Terminal Spin-Hall Nano Oscillators," in *IEEE Transactions on Magnetics*, vol. 55, no. 10, Oct. 2019.

**Summary:** This paper presents a behavioural model of three-terminal spin-Hall nano-oscillators. Important characteristics such as operating frequency, DC-operating point, phase noise and output power are captured and verified against experimental data. Finally, the behavioural model is implemented in Verilog-A which allows for co-simulation with electronic circuits.

**Author's Contribution:** Model development and implementation in Verilog-A, verification against experimental data and writing the manuscript draft.

- [Paper II] D. I. Albertsson, J. Åkerman and A. Rusu, "A Magnetic Field-to-Digital Converter Employing a Spin-Torque Nano-Oscillator," in *IEEE Transactions on Nanotechnology*, vol. 19, pp. 565-570, July 2020.

*T-NANO Best Paper of the Year Award, 2020.*

**Summary:** This paper presents a magnetic field-to-digital converter using a spin-torque nano-oscillator (STNOs). The system is inspired by time-based ADCs which encode data in frequency/phase rather than voltage. The spin-torque nano-oscillator acts as a magnetic field sensor that reacts to a change in magnetic field by adjusting its frequency. Cadence behavioural simulations of a spin-torque nano-oscillator and the associated CMOS circuitry are performed to evaluate the performance of the system. We identify that the performance is limited by phase noise and discuss how this challenge can potentially be overcome. The results show that, even with the current maturity of spintronic oscillators, comparable performance to state-of-the-art magnetic field sensors can potentially be achieved, making it a promising application for spintronic oscillators.

**Author's Contribution:** Design and simulations, analysis and writing the manuscript draft.

- [Paper III] D. I. Albertsson, M. Zahedinejad, A. Houshang, R. Khymyn, J. Åkerman, and A. Rusu , "Ultrafast Ising Machines using spin torque nano-oscillators", *Appl. Phys. Lett.* 118, 112404, March 2021.

**Summary:** In this paper, the potential of realizing IMs based on a network of coupled spin-torque nano-oscillators (STNOs) is explored. This is the first proposal targeting spintronic oscillators to realize Ising Machines. The paper focuses on demonstrating that STNOs exhibit all the desired characteristics needed to realize oscillator-based IMs. This is accomplished by performing numerical simulations of the differential equations describing injection locked and ferromagnetically/antiferromagnetically coupled STNOs, using the universal auto-oscillator model. Subsequently, numerical simulations of the differential equations describing an STNO based IM solving various Max-Cut problems are performed. This work demonstrates that spintronic oscillators are promising candidates for implementing future IMs.

**Author's Contribution:** Numerical simulations and analysis, writing the manuscript draft.

- [Paper IV] D. I. Albertsson, and A. Rusu, "Highly Reconfigurable Oscillator-Based Ising Machine Through Quasiperiodic Modulation of Coupling Strength", in *Sci Rep* 13, 4005, March 2023.

**Summary:** In this paper, the possibility of using coupled oscillators, operating at distinct frequencies, as a highly reconfigurable Ising machine is explored. Firstly, the approach is analyzed based on numerical simulations of differential equations describing phase coupled Kuramoto oscillators, and subsequently, proof-of-concept circuit simulations based on a network of coupled ring oscillators are performed. Finally, the limitations of the proposed approach are identified and discussed.

**Author's Contribution:** Numerical and circuit simulations, analysis and writing the manuscript draft.

- [Paper V] D. I. Albertsson, and A. Rusu , "Ising Machine Based on Bifurcations in a Network of Duffing Oscillators", *IEEE International Symposium on Circuits and Systems (ISCAS)*, Monterey, CA, USA, May 2023.

**Summary:** This paper explores the possibility of realizing Ising machines based on bifurcations in Duffing oscillators. To verify the feasibility of this approach, a circuit implementation of Duffing oscillators exhibiting bifurcations is proposed and numerically analysed. The proposed IM is then successfully demonstrated through simulations of differential equations describing large coupled Duffing Oscillator networks solving various Max-Cut problems. This work opens a new research direction for realizing analog IMs.

**Author's Contribution:** Numerical simulations and analysis, writing the manuscript draft.

# Chapter 1

## Introduction

Electronics have transformed the society over the last decades and the same trend is expected to continue in the coming years. For more than 50 years, the number of transistors per unit area has doubled roughly every two years, as predicted by the famously known Moore's law [1]. This scaling of the transistor dimensions results in a better performance-to-cost ratio and consequently, in an exponential growth of the semiconductor industry [2]. Although Moore's law has held up, novel technology advancements were needed to continue this trend. For example, the switch from bipolar transistors (BJT) to complementary metal-oxide transistors (CMOS) in the 1980s and from planar CMOS to 3D finFETs are just some of the innovations that have kept Moore's law alive for so long [3]. In the near future, large semiconductor companies are expected to continue this trend by transitioning to gate-all-around FETs (GAAFET) with commercial production already started for the 3nm process [4, 5]. This continuous scaling of the transistor dimensions is generally referred to as "More Moore". However, the feature sizes of CMOS transistors are approaching the size of silicon atoms, which inherently poses a fundamental limit to scaling. Additionally, the time to develop the tools required to fabricate smaller nodes is increasing, leading to increased cost and production overhead [2, 3]. These drawbacks have sparked an interest in alternative approaches to develop next generation electronic systems, such as "More than Moore" and "Beyond CMOS".

Modern electronic systems generally include a processing unit that requires various peripherals to achieve its purpose. These peripherals can be sensors, actuators, passive components, radio frequency (RF)/analog and mixed-signal integrated circuits (ICs), etc. The processing unit and the peripherals are generally placed together on a printed circuit board (PCB). The idea behind "More than Moore" is to instead integrate all of these functionalities in a single package or even on a single chip [2]. Since "More than Moore" deals with scaling from a completely different angle (compared to "More Moore"), it is not considered to be a direct competitor, but an alternative approach to scaling. Alternatively,

"Beyond CMOS" is concerned with new devices including alternative transistors such as tunneling field-effect (TFETs) [7] or piezo-electric transistors (PFETs) [8] as well as completely different technologies based on spintronics [9] or memristors [10, 11], etc. [6]. The applications of beyond CMOS devices is twofold as stated in the international roadmap for devices and systems [6]. Firstly, extending the functionality of CMOS technology via heterogeneous integration of new technologies ("Beyond CMOS devices"). This approach has already seen commercial success for example with magnetic random-access memories (MRAM) based on spintronics [12] but continues to be an important research direction. Secondly, completely new information processing architectures, which include for example quantum and neuromorphic computing. The relationship between these two domains and "More Moore" is presented in Fig. 1.1(a). It is increasingly difficult for the "More Moore" trend to keep up with the performance requirements of emerging applications such as big data, internet-of-things (IoT), artificial intelligence and exascale supercomputing [6]. This is where "Beyond CMOS" devices could contribute with the performance required for future electronic systems. However, innovation at device and material level is only one of the directions needing further development. In the long-term future, more efficient electronic systems will require innovation in other domains, such as architecture/packaging along with computational/information processing paradigms [3]. In Fig. 1.1(b) these

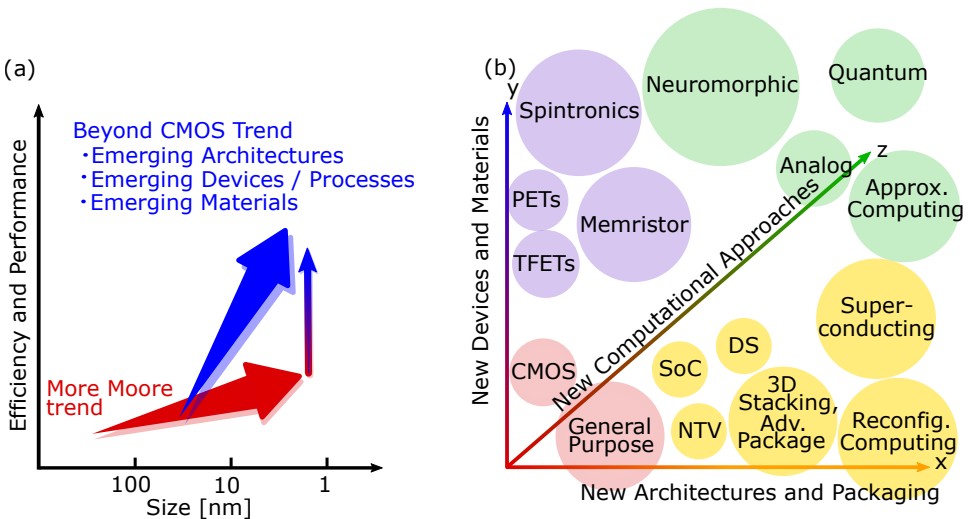


Figure 1.1: (a) Illustration of the relationship between More Moore and Beyond CMOS trends (adapted from Figure BC1.1 in the international roadmap for devices and systems [6]) and (b) 3 domains of innovation for the future of computing beyond Moore's Law (adapted from Figure 3 in [3], NTV: Near threshold voltage, SoC: System-on-chip, DS: Dark silicon.)

domains are presented as a 3D plot extending from conventional CMOS at the origin. The three domains of innovation are predicted to be: new architectures and packaging solutions, new devices and materials (Beyond CMOS), and new computational approaches [3]. Innovations in these domains has the potential to not only improve the core computational units, such as CPUs or MCUs, but also other information processing units including analog-to-digital converters (ADCs), filters, amplifiers, etc. To continue developments in these three domains for both computational and information processing large efforts in fundamental science and engineering are necessary.

In order to fulfill the performance requirements of future applications, various approaches are being considered, such as using time or phase-based information encoding instead of amplitude-based. Specifically, encoding or computing is performed by using the phase/time of digital or analog signals rather than amplitude. In these systems, the conversion to time/phase-based information is commonly done using oscillators, such as ring oscillators. This approach was inspired from communication systems where oscillator frequency or phase is extensively used instead of amplitude. The main motivations behind this approach are the following. Firstly, in small technology nodes, the signal-to-noise ratio (SNR) of analog circuits degrade as a consequence of lower supply voltages. To address this issue, the voltage amplitudes can be converted to time/phase-based information, to partially avoid the degradation of SNR. This approach has been employed and demonstrated in time-based ADCs [13], operational amplifiers [14], filters [14, 15] and even time-based neural networks [16]. Secondly, the phase dynamics in networks of coupled oscillators can be mapped to computational problems [17, 18], such as to perform convolution [19], implement neural networks [20] or solving optimization problems [21]. Consequently, complex problems can be solved using a relatively simple network of low power coupled oscillators. These applications, in combination with emerging "Beyond CMOS" oscillators that have been developed in recent years, open up an interesting approach to develop next generation electronic systems and computing architectures. Specifically, extending electronics to use phase-/time-based information beyond their conventional use in communication systems.

## **1.1 Beyond Conventional Oscillators and their Applications**

Modern electronic oscillators are generally harmonic or relaxation oscillators, depending on their characteristics, and are fundamental building blocks in communication systems or for clock generation. These oscillators range from typical ring or Colpitts oscillators to microwave oscillators based on gallium arsenide (GaAs) or indium phosphide (InP) [22, 23]. The choice of oscillator heavily depends on the application since each type of oscillator has trade-offs in terms of area, power consumption, cost and other performance metrics. With the rapid increase in the number of connected devices required by the IoT applications,

academia and industry continue to explore various types of oscillators that can meet these demands [24, 25]. For instance, in recent years, spintronic oscillators have been studied for this purpose [26–30] due to their promising properties, including small size, GHz tunability, nanosecond turn-on times and relatively low power consumption [31]. However, they also come with challenges, such as low output power and poor phase noise performance, which limit them from wide-spread use in communication systems. This has lead the research community to explore alternative applications that could benefit from nano-scaled spintronic oscillators.

It has long been known that analog computers are specifically well suited for solving differential equations (DEs) [32]. The simplest example of this approach is how a mass oscillating at the end of a spring can be "simulated" using a basic LC circuit. Extending on this and other similar ideas, complex systems have been simulated using analog circuits [33]. However, the advantage of using analog computers has been out-weighted by the simplicity and accuracy of their digital counterparts. Recently, the interest for developing unconventional computing architectures targeting very specific applications, which are challenging to implement on conventional hardware, has sparked a revival of customized analog or mixed-signal computing approaches. This interest is driven by emerging applications which could potentially benefit from analog/mixed-signal implementations, including neural networks [34], neuromorphic computing [35], optimization accelerators [36], etc.

Inspired by neuromorphic computing and communication between neurons in the brain, one of these approaches is using the rich phase dynamics of coupled oscillator networks for computational tasks [17]. In these systems, the information is generally communicated in phase, frequency and potentially amplitude, which opens up new possibilities compared to conventional digital architectures. The simplest idea of using such a dynamical network is the direct implementation of digital logic, but using phase of oscillators rather than level-based digital logic. This approach is directly inspired by Von Neumann's idea of oscillatory logic and has been further explored in recent years [37, 38]. Other unconventional applications, such as pattern recognition or neuromorphic computing using coupled oscillator systems, has been investigated and demonstrated with both CMOS oscillators [39, 40] and emerging devices such as phase-transition [41] or spintronic oscillators [42, 43]. Additionally, the possibility of realizing neural networks based on coupled layers of oscillators has been explored experimentally for CMOS [19, 44] and phase-transition oscillators [45–47], and theoretically, for spintronic oscillators [48, 49]. Moreover, the ring oscillator-based implementation proposed in [19] shows comparable performance to advanced digital implementations, which highlights the potential of employing oscillator networks to perform computational tasks. A more recent demonstration of using networks of coupled oscillators for computing is the so-called Ising machine (IM), which have been most extensively explored using quantum computers, generally referred to as quantum annealers. IMs are hardware architectures targeting complex com-

Table 1.1: Comparison of different oscillators for unconventional computing.

Oscillator	Frequency [GHz]	Area	Energy/cycle [J]	Coupling mechanism	Availability
Ring [19]	Up to $\approx 10 \text{ GHz}$	$10 \mu\text{m}^2$ *	$10^{-15}$	Electrical	Commercial
Schmitt trigger [50, 51]	Up to $\approx 10 \text{ GHz}$	$74 \mu\text{m}^2$ **	$10^{-9}$	Electrical	Commercial
Spintronic [52]	Upward of $50 \text{ GHz}$	$0.01 \mu\text{m}^2$	$10^{-15}$	Electrical, magnetic, spin wave	Emerging
Phase-transition*** [53]	Up to $\approx 10 \text{ GHz}$	$0.001 \mu\text{m}^2$	$10^{-17}$	Electrical	Emerging

\*Estimated from [19], implemented in  $22 \text{ nm}$  technology

\*\*Implemented in  $65 \text{ nm}$  technology

\*\*\*Predicted if the dimensions are scaled to  $< 10 \text{ nm}$

binatorial optimization (CO) problems, which are extremely challenging to solve on conventional von Neumann computers. The state-of-the art research results on IMs indicate that IMs could provide great potential benefits in terms of speed as compared to conventional computing approaches.

To realize large scale networks of coupled oscillators for computing or time/phased-based information processing, the choice of oscillator is imperative. The oscillator needs to have a small area, be energy efficient and allow for coupled networks to be realized. Additionally, operating frequency, tunability and noise are also important performance metrics, which depend on the application. In table 1.1, a summary of commonly used oscillators for computing is presented. Both ring and Schmitt trigger oscillators are intriguing options as they can readily be designed using commercially available CMOS technologies, are scalable and simple to design. Emerging oscillators such as spintronic and phase-transition oscillators also have interesting characteristics for computing. Spintronics is an emerging field where both the electron charge and spin are employed to realize new devices. Specifically, spintronic oscillators are a class of devices where a spin polarized current is used to excite a precession in a ferromagnetic (FM) stack, leading to the generation of a microwave voltage [31]. Spintronic oscillators have been realized with extremely high operating frequencies, upwards of  $50 \text{ GHz}$  and can potentially be extended to terahertz range [52, 54]. Additionally, they can be coupled together in various ways using electrical, magnetic or spin wave couplings (or even a combination of some or all), which is a unique feature of these devices. However, due to the low output power of these devices, an amplifier (e.g. CMOS amplifier) is generally needed to interface spintronic oscillators with external circuitry. This is a major disadvantage since in many applications, the power consumption and area will be dominated by the amplifier. Additionally, as previously mentioned, the phase noise of spintronic oscillators is also a concern and device variability. Finally, a recently developed technology based on phase-transitions in vanadium dioxide ( $\text{VO}_2$ ) or alternatively niobium dioxide ( $\text{NbO}_2$ ) has been used to realize energy efficient and compact oscillators for computing [45, 46, 53, 55, 56]. The development of these oscillators is still in early stages and the data presented in Table 1.1 is the predicted behaviour (by the authors in [53]), if the dimensions of these devices would be scaled down below  $10 \text{ nm}$  in size.

Recently developed oscillators as well as traditional oscillators based on various modern technologies drove the development of the previously discussed emerg-

ing oscillator-based applications. Consequently, there is immense room to explore the potential of these oscillators for computational and information processing applications. An interdisciplinary contribution from different fields, including electrical engineering, physics and mathematics is required to develop such applications.

## 1.2 Motivation

The continuous demand for increased computation and information capacity of electronic systems is currently driven by emerging applications including IoT, neural networks, virtual reality and various other similar tasks. This has lead to increased focus on developing extremely customized electronic systems, which are tailored to very specific applications to achieve the best possible performance. Moreover, this has sparked an interest in relatively unconventional approaches, compared to standard digital/analog systems, such as using oscillators beyond their regular use in communication systems. Oscillators can be realized using relatively simple circuit elements and can exhibit complex behaviour especially when combined with harmonic injection locking and frequency/amplitude modulation. This opens the question whether oscillator-based information processing paradigm, using the frequency, phase and/or amplitude of oscillators, can bring potential benefits in next generation computation architectures and electronic systems. Additionally, various spintronic oscillators have been developed in recent years. These emerging devices exhibit promising characteristics, but also come with their drawbacks and challenges. However, with the continuous efforts on improving their performance, spintronic oscillators could be a promising candidate for future information processing systems based on oscillators. Considering the societal and industrial needs for efficient computation and information processing, as well as the promising characteristics of electronic and spintronic oscillators, this thesis aims at investigating the potential of these oscillators for developing applications which could benefit from being processed in phase/frequency domain or exploit unique characteristics of unconventional oscillators.

## 1.3 Research Objectives

The primary goal of this thesis is to investigate the applications of both CMOS oscillators and emerging spintronic oscillators for information processing paradigms. These applications extend beyond their conventional use in communication systems or for clock generation.

- **Objective 1:** Develop the required spintronic oscillator models to allow for co-simulations with CMOS circuits.
- **Objective 2:** Identify suitable applications for spintronic oscillators and demonstrate them.

- **Objective 3:** Explore unconventional computing approaches based on oscillators, evaluate them through numerical and/or circuit simulations and demonstrate proof-of-concepts.

## 1.4 Research Contributions

The contributions addressing the research objectives are listed as follows:

- **Contribution 1 [Paper I]:** A behavioural model of a promising spintronic oscillator, the three-terminal spin-Hall nano-oscillators (SHNOs), is proposed and verified against experimental results. The behavioural model is compatible with industry standard electronic design automation (EDA) tools and captures the most important characteristics of the three-terminal SHNOs. This contribution is a step towards further exploring hybrid spintronic-CMOS systems.
- **Contribution 2 [Paper II and III]:** Two new potential applications of spintronic oscillators are identified and explored. First, the possibility of utilizing spintronic oscillators as frequency based magnetic field sensors is explored. The proposed architecture is inspired by time-based ADCs and differs drastically from previous studies and proposals. Secondly, the possibility of utilizing spintronic oscillators to realize IMs is identified. It is demonstrated that spintronic oscillators exhibit all the fundamental characteristics which are needed to realize oscillator-based IMs.
- **Contribution 3 [Paper III, IV and V]:** IMs based on different types of oscillators are studied. Specifically, it is demonstrated that large networks of coupled spintronic oscillators can be operated as IMs for solving optimization problems. Additionally, the potential of realizing a highly reconfigurable oscillator-based IM is studied and demonstrated. Finally, a new type of oscillator-based IM using Duffing oscillators is investigated and demonstrated.

## 1.5 Thesis Organization

The thesis is organized into four chapters with the following structure:

- **Chapter 1** presents the background and puts the work into context with respect to the current research trends in electronics. Additionally, the work is motivated and the objectives and contributions are presented.
- **Chapter 2** presents an overview of spintronic oscillators, their operation and state-of-the-art. Thereafter, the proposed behavioural model of three-terminal SHNOs is presented. Finally, the potential of employing spintronic oscillators to realize magnetic field sensors, inspired by time-based ADCs, is presented.

- **Chapter 3** introduces IMs and presents an overview of different technologies used to realize IMs. The theory behind oscillator-based IMs, the core of this chapter, is introduced in detail. Next, the potential of realizing IMs based on spintronic oscillators is discussed, and a reconfigurable oscillator-based IM is presented. Finally, the proposed IM based on bifurcations in a network of coupled Duffing oscillators is introduced and a proof-of-concept is presented.
- **Chapter 4** concludes the thesis work and presents possible future research directions.

## Chapter 2

# Spintronic Oscillators - Modelling and Applications

Spintronics is a technology that uses the spin of electrons, e.g. spin currents in semiconductors, metals or magnetic insulators, to realize new devices. The origin of this approach can be traced back to the 1990s, when two papers by Slonczewski [57] and Berger [58] predicted that spin-polarized current could be used to change the orientation of a local magnetization, called spin-transfer torque (STT). This is a consequence of the transfer of angular momentum from a spin-polarized current to the local magnetization. This phenomena was experimentally demonstrated a couple of years later in [59, 60]. Moreover, in specially designed material stacks, the STT can be used to either excite magnetization precession or switch the magnetization orientation (similar to flipping a bit from zero to one). These characteristics were used to develop a new memory technology called STT - magnetic random-access memory (STT-MRAM) [12] and microwave oscillators [31, 61]. While STT-MRAM is currently commercially available and in recent years there has been extensive research on a new spintronic MRAM, called spin-orbit torque MRAM [62], spintronic oscillators have currently not reached the same level of maturity.

In this chapter, spintronic oscillators will be discussed. Specifically, the theory behind the operation and different architectures will be presented. Thereafter, the behavioural model of a three-terminal SHNO, presented in [**Paper I**], will be elaborated in detail. Finally, the potential of using spintronic oscillators for time-based magnetic field sensing, as presented in [**Paper II**], will be discussed.

### 2.1 Spintronic Oscillators

Spintronic oscillators are generally categorized based on the material stack, geometry and the underlying physics governing the operation. State-of-the-art devices and their geometries are presented in Fig. 2.1 [31]. Among those, the nanopillar

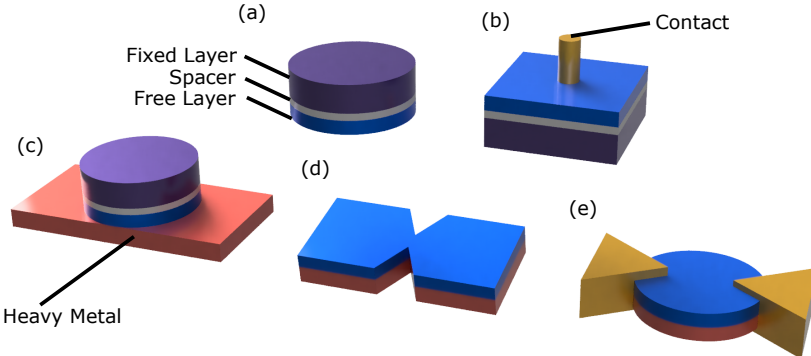


Figure 2.1: Geometries of different spintronic oscillators: (a) nanopillar STNO, (b) nanocontact STNO, (c) three-terminal SHNO, (d) nanoconstriction SHNO and (e) nanogap SHNO.

spin-torque nano-oscillators (STNOs), presented in Fig. 2.1 (a) [63, 64], are the most widely known. The STNO's geometry is generally realized using a circular pillar of multi-layers consisting of a fixed (polarized) FM/spacer layer/free FM layer. The material used in the spacer can either be a magnetic material (e.g. Cu) or an insulator (e.g. MgO). Depending on the spacer material, these are referred to as a spin valve or magnetic tunnel junction (MTJ) STNOs, respectively. An alternative geometry, the nanocontact STNO [65, 66] is presented in Fig. 2.1 (b). These devices share many similarities with the nanopillar STNOs, but instead of having a circular pillar, the current is applied through a nano-sized contact to a multilayer film as shown in Fig. 2.1 (b). The current is largely confined in the area below the contact, where the precession takes place. Since the volume of the magnetization involved in the precession is larger than in nanopillar devices, nanocontact STNOs generally require 1-2 orders of magnitude higher current densities to operate [31]. Lastly, Figs. 2.1 (c)-(e) present different types of SHNOs [67–69]. The major difference between these devices and the nanopillar STNOs or nanocontact STNOs is that instead of using STT to excite the precession, the so-called spin-Hall effect (SHE) generates the spin-current, similar to how spin-orbit torque MRAMs operate [70, 71]. In the following sections, the physics covering the operation of these spintronic oscillators will be discussed. Specifically, giant magnetoresistance (GMR)/tunneling magnetoresistance (TMR) and STT for STNOs, while anisotropic magnetoresistance (AMR) and the SHE for SHNOs will be discussed.

### 2.1.1 Magnetoresistance

Magnetoresistance (MR) generally refers to a change in a material or a multilayer conductance depending on the applied magnetic field or the magnetization direc-

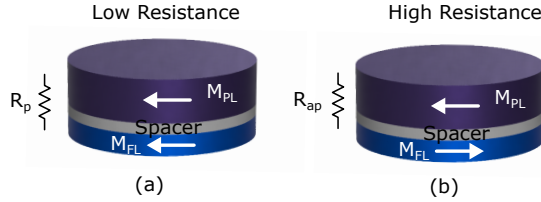


Figure 2.2: The GMR/TMR effect: (a) low resistance and (b) high resistance state.

tion. The AMR was the first MR effect discovered in 1857 by Lord Kelvin [72]. This effect describes the change in a FM material conduction depending on the orientation of the magnetization relative to the current direction. This change in the conductance is usually only a few percent at room temperature [73, 74] and has long been used in magnetic field sensors.

Alternatively, a much larger conductance change is associated with the GMR and TMR effects, which are observed in magnetic multilayers, as presented in Fig. 2.2. The GMR effect was first discovered by Peter Grunberg and Albert Fert, which received the Nobel prize in physics for this discovery [75, 76]. In a magnetic multilayer consisting of a fixed FM/metallic spacer/free FM layers, i.e. a spin-valve, they observed that when a current is applied to the device, the resistance changes drastically depending on the magnetization orientation between the FM layers. Specifically, if the FM layers have a parallel alignment, the resistance is significantly lower than if they are anti-parallel, as presented in Fig. 2.2. Moreover, the resistance  $R$  of the device has a strong dependence on the angle  $\phi_t$  between the magnetization direction of the layers, which can be described as [77, 78]:

$$R = \frac{R_{ap} + R_p}{2} - \frac{R_{ap} - R_p}{2} \cos(\phi_t) \quad (2.1)$$

where  $R_{ap}$  and  $R_p$  are the resistance of the spin-valve, when the magnetization is anti-parallel or parallel, respectively. This effect is attributed to a change in the conductance of FM material depending on the spin states of the electrons. The TMR effect is very similar to the GMR, but the material stack consists of fixed FM/insulator (spacer)/free FM layers (MTJ) [78]. The major difference between the two is that the metallic spacer is replaced by a thin,  $\approx 1\text{ nm}$ , insulator. The change in conductance between the parallel and anti-parallel states for both GMR and TMR is generally characterized in terms of MR ratio:

$$MR = (R_{ap} - R_p)/R_p \quad (2.2)$$

with MR ratios of spin-valves generally in the range of  $\approx 10\%-20\%$ , while MTJs have shown much higher MR ratios [79, 80](up to  $\approx 600\%$  in [80]). In spintronic oscillators, the MR ratio is proportional to the output power and consequently a high MR ratio is desirable. For this reason, MTJ STNOs based on the TMR effect have received more interest from the research community in recent years.

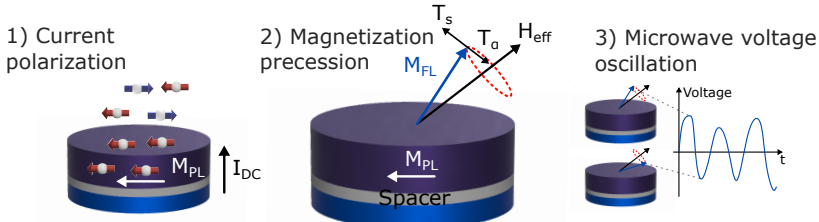


Figure 2.3: Operating principles of STNOs.

### 2.1.2 Operation of STNOs and SHNOs

The operation principles of STNOs are determined by two phenomena: the previously discussed GMR/TMR (for spin-valve/MTJ STNOs) and exciting a magnetization precession using STT. Different modes of oscillations can be excited in STNOs, including a vortex and uniform precession [31], but here the discussion is limited to uniform precession in MTJ STNOs since these are the main focus of this work. Consequently, for the remainder of the chapter, if it is not explicitly stated as a vortex or spin-valve STNO, the discussion applies to uniform MTJ STNOs. It is worth highlighting that the operating principles of spin-valve based STNOs result in very similar behaviour as is discussed below for MTJ STNOs.

When a DC current  $I_{DC}$  is applied to a MTJ, the electrons become spin-polarized in the fixed FM layer  $M_{PL}$  as shown in Fig. 2.3 1) and subsequently, tunnel through the insulating barrier. Since the current is spin-polarized, angular momentum is transferred to the free layer as the electrons pass through the MTJ. This transfer of angular momentum induces a torque which can be used to cancel out the intrinsic magnetization damping in the free layer and excite steady state precession of the magnetization  $M_{FL}$  as presented in Fig. 2.3 2) [81]. Since there is current flow through the MTJ, the TMR effect translates the magnetization precession into an oscillating microwave voltage as in Fig. 2.3 3). The excitation of  $M_{FL}$  to a steady state precession can be understood using the Landau-Lifshitz-Gilbert equation with an additional Slonczewski STT term as [57, 82, 83]:

$$\frac{d\mathbf{M}_{FL}}{dt} = -\gamma [\mathbf{M}_{FL} \times \mathbf{H}_{eff}] + \mathbf{T}_\alpha + \mathbf{T}_S \quad (2.3)$$

where  $\mathbf{M}_{FL}$  is the magnetization vector of the free layer,  $\gamma$  is the gyromagnetic ratio,  $\mathbf{H}_{eff}$  is the effective magnetic field,  $\mathbf{T}_\alpha$  is the intrinsic damping term and  $\mathbf{T}_S$  is the STT term. Specifically, the effective field  $\mathbf{H}_{eff}$  can consist of contributions from an applied external field  $\mathbf{H}_{ext}$ , anisotropy field  $\mathbf{H}_A$ , interlayer exchange field  $\mathbf{H}_{int}$ , etc [81]. The first term on the right hand side of (2.3), consisting of the cross-product of  $\mathbf{M}_{FL}$  and  $\mathbf{H}_{eff}$ , describes a Larmor precession of  $\mathbf{M}_{FL}$  around  $\mathbf{H}_{eff}$ . The damping term can be explicitly written as [81, 82]:

$$\mathbf{T}_\alpha = -\frac{\lambda}{M_s} \mathbf{M}_{FL} \times (\mathbf{M}_{FL} \times \mathbf{H}_{eff}) \quad (2.4)$$

where  $\lambda$  is a damping coefficient and  $M_s$  is the saturation magnetization. In the absence of STT, i.e.  $\mathbf{T}_S = 0$ , the precession is damped and  $\mathbf{M}_{FL}$  quickly settles to a fixed direction. Alternatively, if  $\mathbf{T}_S \neq 0$ , the STT term can be written as [57, 83]:

$$\mathbf{T}_S = \frac{\sigma I}{M_s} \mathbf{M}_{FL} \times (\mathbf{M}_{FL} \times \mathbf{e}_p) \quad (2.5)$$

where  $\sigma$  is a coefficient describing the magnitude of STT,  $I$  is the applied current and  $\mathbf{e}_p$  is a unit vector in the direction of STT. This STT term can be used to cancel out the damping term  $\mathbf{T}_\alpha$  and excite steady state magnetization precession as it's presented in Fig. 2.3. This magnetization precession is translated into a microwave voltage through the GMR/TMR effect which can be written as [84]:

$$V_{STNO} = V_{dc} + R_{prec} I_{MTJ} \cos(\omega_p t + \psi(t)) \quad (2.6)$$

where  $V_{dc}$  is a DC component,  $R_{prec}$  is the amplitude of the resistance change,  $I_{MTJ}$  is the DC current through the MTJ,  $\omega_p$  is the operating frequency and  $\psi(t)$  is the phase noise. It is worth highlighting that  $V_{dc}$ ,  $R_{prec}$ ,  $\omega_g$  and  $\psi(t)$  are all dependent on the applied DC current, as well as the magnitude and direction of  $\mathbf{H}_{eff}$ .

Three-terminal SHNOs, presented in Fig. 2.3 (c), share many similarities with the nanopillar STNOs. These devices, explored for the first time in [67], consist of the same pillar structure as MTJ STNOs, but additionally a heavy metal (HM) strip, e.g. Tantalum (Ta) or Tungsten (W), is placed adjacent to the free FM layer. As previously mentioned, SHNOs utilize the SHE to cancel the damping term in (2.3). The Hall-effect is a widely known effect that appears when a current in a conductor is exposed to a perpendicular magnetic field. Under these conditions, a potential difference (voltage) appears transverse to the current flow [85]. This effect was first discovered by Edwin Hall in 1879 [85], and it has been extensively used to realize magnetic field sensors, so called Hall-effect sensors [73]. The SHE is similar to the Hall-effect, but instead of a charge imbalance leading to a voltage difference across the conductor, there is a spin-imbalance between the edges. This leads to a pure spin-current being generated on the surface of the conductor [70]. The SHE is most pronounced in HM as a consequence of their strong spin-orbit interaction and is generally quantified in terms of the spin-Hall angle  $\theta_{SH} = I_{spin}/I_{HM}$ , which is the ratio of DC current through the HM,  $I_{HM}$ , to spin-current,  $I_{spin}$  [71]. In three-terminal SHNOs, this effect is used to cancel out the damping term and excite magnetization precession by applying a current  $I_{HM}$  through the HM that is adjacent to the free layer. A small sensing current is then applied through the MTJ, which translates the magnetization precession into a voltage based on the TMR effect [67]. Hence, excitation and detection of the magnetization dynamics is de-coupled to two different input terminals (the third is a common ground). A more detailed description of the operating principles of three-terminal SHNOs is presented in [Paper I]. Two terminal SHNOs, such as the nanoconstriction and nanogap SHNOs presented in Fig. 2.1 (d) and (e),

are also based on the SHE, but in these devices the magnetization dynamics are detected through the AMR effect [68, 69, 74]. Consequently, these devices have a relatively low output power compared to three-terminal SHNOs or MTJ STNOs. However, nanoconstriction SHNOs can be easily fabricated and have been demonstrated in large arrays [86], which is beneficial for two reasons. Firstly, the linewidth is reduced and the output power increases in arrays of synchronized spintronic oscillators compared to a stand-alone device. Secondly, this makes nanoconstriction SHNOs an intriguing option for applications requiring a large number of interacting oscillators, such as neuromorphic computing, as it will be discussed in the next section.

### 2.1.3 State-of-the-Art Spintronic Oscillators and Applications

In this section, the most important performance metrics of spintronic oscillators are highlighted and state-of-the-art is briefly discussed. The most relevant performance metrics of spintronic oscillators are the operating frequency, frequency tunability, output power and linewidth. The operating frequency drastically depends on the implementation of spintronic oscillators, ranging from hundreds of  $MHz$  for vortex-based STNOs to tens of  $GHz$  for spin-valve STNOs and nanoconstriction SHNOs. The frequency tunability is generally determined by the spintronic oscillator type and the used materials, and it ranges from tens of  $MHz$  to hundreds of  $MHz$ , for each milliampere of change in the applied biasing current [31]. The output power also depends on the type of spintronic oscillator and it is generally in the range from  $pW$  to  $\mu W$  with linewidths usually from a few  $MHz$  to hundreds of  $MHz$ .

Arguably, spintronic oscillators are not currently utilized in commercial applications due to their relatively low output power and large linewidth. The first experimental demonstrations of spintronic oscillators, which were based on nanopillar spin-valve STNOs had an output power less than or around  $100\ pW$ . Fortunately, with the continuous efforts of the research community, in recent years, this has been increased to the  $\mu W$  range, with the highest reported output power of  $10.1\ \mu W$  for a vortex MTJ STNO [87]. However, vortex STNOs also bring disadvantages compared to conventional uniform STNOs. These disadvantages include significantly lower operating frequency, usually  $< 1\ GHz$ , and larger size, up to 10 times larger area compared to uniform MTJ STNOs. For uniform STNOs, an output power of  $2.4\ \mu W$  was demonstrated in [66] for a nanocontact MTJ STNO, and an output power of  $550\ nW$  was presented in [64] for a nanopillar MTJ STNO with uniform precision. A comprehensive comparison of different STNOs (e.g. vortex, uniform spin-valve, uniform MTJ) and their output power and linewidth is presented in [88]. Both nanoconstriction and nanogap SHNOs generally have much lower output power compared to STNOs, since they are based on the AMR effect instead of the TMR or GMR effect. Consequently, the SHNOs output power is generally in the  $pW$  range [68, 74, 89]. Alternatively,

three-terminal SHNOs, which consist of a MTJ placed on top of the HM, could potentially overcome this issue of two terminal SHNOs [90].

Another major disadvantage of spintronic oscillators is the need for an external magnetic field. Most of the spintronic oscillators studied so far require an external magnetic field to excite the oscillations. However, field-free implementations have also been experimentally demonstrated [91–93], but the output power of these implementations is in the  $pW$  or  $nW$  range. In recent years, the possibility of synchronizing multiple STNOs or SHNOs to increase the output power and reduce the linewidth has been also extensively explored [94–97].

As previously mentioned, spintronic oscillators were originally considered as a potential candidate to replace voltage-controlled oscillators (VCOs) in communication systems. This application of spintronic oscillators has been extensively explored in literature [26–30, 98]. Currently, the performance of STNOs is significantly lower compared to conventional CMOS-based VCOs, especially in terms of phase noise and output power. This has lead the research community to explore alternative applications that could benefit from the high operating frequency and nano-scale size of spintronic oscillators. Many of these applications are targeting unconventional computing approaches, including machine learning [99, 100], neuromorphic computing [42, 86, 101–105] and IMs [106–108]. For example, in [102] a network of four coupled STNOs was trained to recognize various different vowels and in [86] a similar task was performed using an array of 16 nanoconstriction SHNOs. Alternatively, utilizing STNOs in microwave assisted magnetic recording for hard disk drives is a promising application. In these hard disk drives, the microwave magnetic field generated by the STNO is used to assist with switching the state of the magnetic medium. This approach has the potential of increasing the density of hard disk drives even further and has been extensively studied [109]. Finally, since spintronic oscillators are extremely sensitive to changes in both applied magnetic field (direction and strength) and current, using this property to develop a new type of magnetic field or current sensor has been explored [110–113].

## 2.2 Modeling of Three-terminal SHNOs

The most extensively studied spintronic oscillators are STNOs and in recent years nanoconstriction SHNOs. While STNOs have the largest output power among spintronic oscillators, nanoconstriction SHNOs have received increased interest since they can be easily fabricated in large arrays and synchronized, as presented in Fig. 2.4 (a) [86]. Moreover, gate control of nanoconstriction SHNOs, which has recently been demonstrated, could potentially allow for individual control of frequencies and/or couplings in an array [114–116]. These important properties are required to further explore the potential of using spintronic oscillators for implementing neuromorphic or unconventional computing, since many of these implementations are based on coupled oscillator networks. As previously discussed, the major disadvantage of these devices is their relatively low output power. The

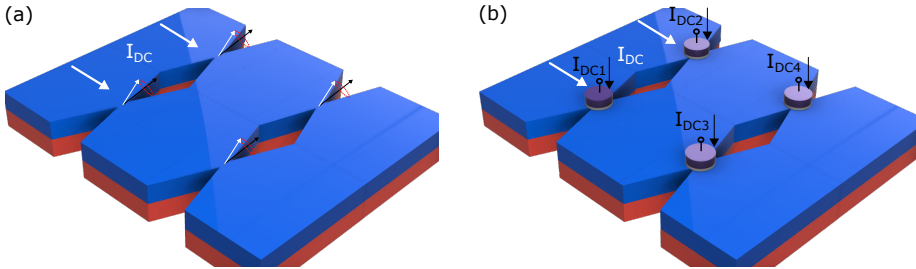


Figure 2.4: Networks of spintronic oscillators based on (a) nanoconstriction SHNOs and (b) nanoconstriction SHNOs with an MTJ on top (i.e. three-terminal SHNO)

three-terminal SHNO has the potential to overcome this issue since it shares many similarities with both STNOs and the nanoconstriction SHNO. As it was mentioned, the tree-terminal SHNO is a MTJ-based device and consequently, its output power is much higher than that of constriction-based SHNOs (100  $nW$  in [90]). Additionally, three-terminal SHNOs could potentially be realized in arrays similar to the nanoconstriction array, but by additionally placing the MTJ on top of the constriction, as shown in Fig. 2.4 (b). This implementation combines the high output power of MTJ STNOs with the ease of realising large nanoconstriction arrays. However, the implementation in Fig. 2.4 (b) has not been experimentally demonstrated yet, but only studied theoretically [117–119]. Finally, three-terminal SHNOs provide increased control compared to both STNOs and two-terminal SHNOs since the excitation of the magnetization dynamics and read-out is separated to two different terminals. Consequently, three-terminal SHNOs could be a promising option for future electronic systems based on spintronic oscillators. As a first step towards further exploring the potential applications of three-terminal SHNOs, a behavioural model of three-terminal SHNOs was developed in [\[Paper I\]](#) and compared to the experimental results in [67]. This is the first three-terminal SHNO model compatible with EDA tools. It was implemented in Verilog-A to allow for co-simulations in Cadence together with CMOS supporting circuitry. The model is based on the macrospin approximation of spintronic oscillators developed in a series of papers by Slavin and Tiberkevich and summarized in [81], and the behavioural STNO model developed in [84, 120]. The macrospin approximation is an analytical approach to describe the operating principles of spintronic oscillators and it is derived from the DEs (2.3), (2.4) and (2.5). However, the macrospin theory lacks various characteristics that are needed to allow for electrical simulations of three-terminal SHNOs together with CMOS circuits. Consequently, the model was developed to capture other necessary characteristics such as DC operating point and output power similar to what was done for STNOs in [84, 120]. In this chapter, the macrospin approximation will be briefly introduced in Section 2.2.1 and supporting information for the behavioural model in [\[Paper I\]](#) presented in the following sections.

### 2.2.1 Universal Auto-oscillator

An auto-oscillator can generally be identified based on the following three elements: 1) a resonant element, 2) a dissipative element which introduces damping, and 3) an active element which compensates the damping term and excites auto-oscillations [81]. The effect introduced by the active elements can often be described as a "negative damping", i.e. as a term having similar form as the dissipative term, but a negative sign. Under these conditions, a nonlinear oscillator model describing auto-oscillators, regardless of physical implementation, can be written as [81]:

$$\frac{dc}{dt} + i\omega_p(|c|^2)c + \Gamma_+ (|c|^2)c - \Gamma_- (|c|^2)c = f(t) \quad (2.7)$$

where  $c$  is the complex amplitude,  $\omega(|c|^2)$  is the resonance frequency,  $\Gamma_+ (|c|^2)$  is the damping rate describing the dissipative element,  $\Gamma_- (|c|^2)$  the negative damping rate describing the active element and  $f(t)$  is an additional term which can be used to take into account perturbations from an external signal or thermal fluctuations. The complex amplitude  $c$  captures both the power and phase of the oscillations as  $p = |c|^2$  and  $\phi = \arg(c)$ , respectively. As it can be seen from (2.7), the resonance frequency and damping rates are both functions of the power  $p$ , which makes this DE a nonlinear dynamical system. This model can be applied to describe the behaviour of a variety of oscillators, as long as they have the three elements (1)-(3), independent of their physical realization. For the case of a uniform STNO, approximate expressions of the terms in (2.7) are found in [81] as:

$$\omega_p(p) \approx \omega_0 + Np \quad (2.8a)$$

$$\Gamma_+(p) \approx \Gamma_G(1 + Qp) \quad (2.8b)$$

$$\Gamma_-(p) \approx \sigma I(1 - p) \quad (2.8c)$$

where  $\omega_0$  is the FM resonance frequency,  $N$  is the nonlinear frequency shift coefficient,  $\Gamma_G$  is the damping torque,  $Q$  is the nonlinear damping coefficient,  $\sigma$  is a coefficient describing the magnitude of STT and  $I$  is the applied current. All of the expressions entering (2.8) are provided in Appendix I in [81]. Utilizing these approximate expressions of the operating frequency and damping terms, a purely analytical approach to describe the operating principles of spintronic oscillators is possible. The macrospin approximation is based on this approach. It is worth highlighting that (2.8a)-(2.8c) are found assuming a weakly nonlinear behaviour. Consequently, this theoretical framework might differ from experimental results if the STNO is strongly nonlinear. However, this approach eliminates the need to solve the DEs describing the magnetization dynamics of the system in (2.3) and consequently, it allows for fast behavioural simulations utilizing EDA tools such as Cadence.

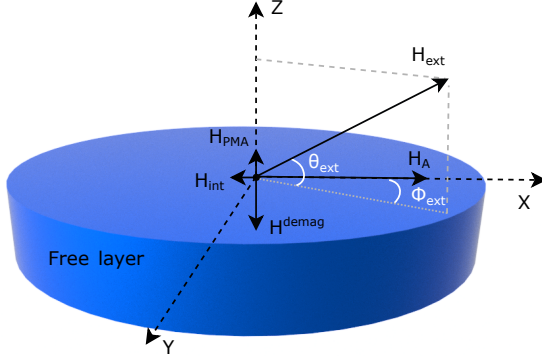


Figure 2.5: Summary of fields contributing to  $H_{eff}$ .

### 2.2.2 Effective Magnetic Field

To accurately model the characteristics of the three-terminal SHNO, the first step is to determine the magnitude and orientation of the effective magnetic field  $H_{eff}$ . The externally applied magnetic field  $H_{ext}$  is applied with an in-plane angle  $\phi_{ext}$  relative to the x-axis and an out-of-plane angle  $\theta_{ext}$  relative to the z-axis, as it is shown in Fig. 2.5. The combination of  $H_{ext}$  and other field contributions results in an effective magnetic field  $H_{eff}$  with angles  $\phi_{eff}$  and  $\theta_{eff}$  which could deviate slightly from  $H_{ext}$  in both magnitude and direction. The magnetization dynamics take place around this axis. The contributions to the effective magnetic field considered in [Paper I] consist of  $H_{ext}$ ,  $H_A$  within the plane anisotropy field, the interlayer coupling field  $H_{int}$  introduced by coupling between the free and fixed layers, and the effective demagnetization field  $H_{eff}^{demag}$  [67, 81, 121]. All of these contributions are considered as input parameters of the behavioural model, which need to be determined from experimental measurements. These contributions to  $H_{eff}$  are relatively standard and are considered for modeling spintronic oscillators, as in [81] and [84], except the effective demagnetization field. Specifically, the device explored in [67] has a significant perpendicular magnetic anisotropy  $H_{PMA}$ , which can be used to reduce the out-of-plane demagnetization field  $H^{demag} = 4\pi M_s$ . Moreover, as it is shown in [67], the magnitude of  $H_{PMA}$  shows a dependence on the voltage across the MTJ,  $V_{MTJ}$ . To accurately model the three-terminal SHNO, this characteristic needs to be taken into account. Inspired by the analysis in [67], the effective demagnetization field was modeled as:

$$H_{eff}^{demag} = H^{demag} - H_{PMA} + \frac{dH_{PMA}}{dV_{MTJ}} V_{MTJ} \quad (2.9)$$

where  $dH_{PMA}/dV_{MTJ}$  is the rate of change of the perpendicular magnetic anisotropy as a function of  $V_{MTJ}$ . As it is shown in [67] and highlighted below, this voltage control of the PMA (often called voltage controlled magnetic anisotropy) leads to a drastic modulation in the operating frequency for small changes in the applied

current through the MTJ. Consequently, the equations used to calculate  $H_{eff}$  in [81] and [84] are re-written to include the effect of  $H_{eff}^{demag}$ , resulting in eq. (2) in [Paper I]. It is worth highlighting that both  $H_{PMA}$  and  $dH_{PMA}/dV_{MTJ}$  can vary between devices and consequently, are considered as input parameters for the behavioural model, as shown in Table I in [Paper I]. Finally, the equations for the effective magnetic field are further simplified considering that  $\theta_{ext} = 0$ , which is the case for the three-terminal SHNO in [67]. This simplification results in eq. (4) in [Paper I] where  $\phi_{eff}$  and  $H_{eff}$  can readily be found using standard numerical solvers. Specifically,  $\phi_{eff}$  is found from eq. 4(a) in [Paper I], while  $H_{eff}$  is computed with eq. 4(b).

### 2.2.3 DC Operating Point

As it was previously discussed, the output signal of spintronic oscillators consists of a DC and an AC component, as presented in Fig. 2.6. As it was already highlighted, the current applied through the HM,  $I_{HM}$ , generates a spin current on its surface, transverse to the direction of electron flow, and it excites a magnetization precession in the adjacent free layer. To detect the precession, the current  $I_{MTJ}$  is applied through the MTJ, which results in a voltage  $V_{out} = V_{DC} + V_{AC}$ . The AC signal will be discussed in detail in a separate section, so for now, the AC components are neglected ( $V_{AC} = R_{prec} = 0$ ) in Fig. 2.6(a). The DC voltage appearing at  $V_{out}$  consists of two components and it can be written as in [Paper I]:

$$V_{DC} = V_{MTJ} + \frac{R_{HM}}{2}(I_{MTJ} + I_{HM}) \quad (2.10)$$

where  $V_{MTJ} = I_{MTJ}R_{MTJ-DC}$ ,  $R_{MTJ-DC}$  is the resistance of the MTJ and  $R_{HM}$  is the resistance of the HM strip. While  $I_{HM}$ ,  $I_{MTJ}$  and  $R_{HM}$  are all known and constant quantities,  $R_{MTJ-DC}$  has a strong dependence on both the applied current,  $I_{MTJ}$ , and the effective magnetic field angle,  $\phi_{eff}$  (through the angle between the fixed and free-layer). For the applied current, the resistance,

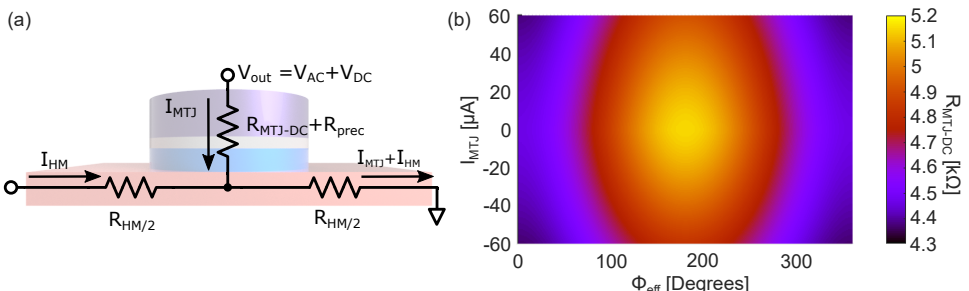


Figure 2.6: (a) Electrical model of the three-terminal SHNO and (b)  $R_{MTJ-DC}$  as a function of external field angle  $\phi_{eff}$  and applied MTJ current  $I_{MTJ}$ .

$R_p$  in the parallel, and  $R_{ap}$  the anti-parallel state, strongly depends on the current  $I_{MTJ}$  (or equivalently  $V_{MTJ}$ ). Moreover, the dependence is asymmetric with the sign of  $I_{MTJ}$ . Computing this dependence along with  $R_p$  and  $R_{ap}$  is a challenging quantum mechanical problem, and consequently, it is not a viable problem to solve in a behavioural model [122, 123]. Therefore,  $R_p$  and  $R_{ap}$  are introduced as input parameters to the behavioural model (obtained from experimental data), while the dependence on  $I_{MTJ}$  is taken into account using a fitting function, as it is presented in detail in [Paper I]. The scaled values of  $R_p$  and  $R_{ap}$ , taking into account the dependence on the applied current, are presented as  $R_{ps}$  and  $R_{aps}$  in [Paper I]. Finally, the DC resistance as a function of  $\phi_{eff}$  can be analytically modeled using (2.1) (or equivalently, written in an alternate form as (10) in [Paper I]). For the parameters presented in Table I in [Paper I], the dependence of  $R_{MTJ-DC}$  as a function of  $\phi_{eff}$  and  $I_{MTJ}$  is presented in Fig. 2.6(b). As it can be observed, the DC resistance is highly dependent on both  $\phi_{eff}$  and  $I_{DC}$ .

## 2.2.4 Operating Frequency

The operating frequency and its nonlinear dependence on both the applied current and the external magnetic field is one of the most important characteristics of spintronic oscillators. Their operating frequency can be calculated with (2.8a) from the macrospin approximation. It is worth highlighting that the mean power

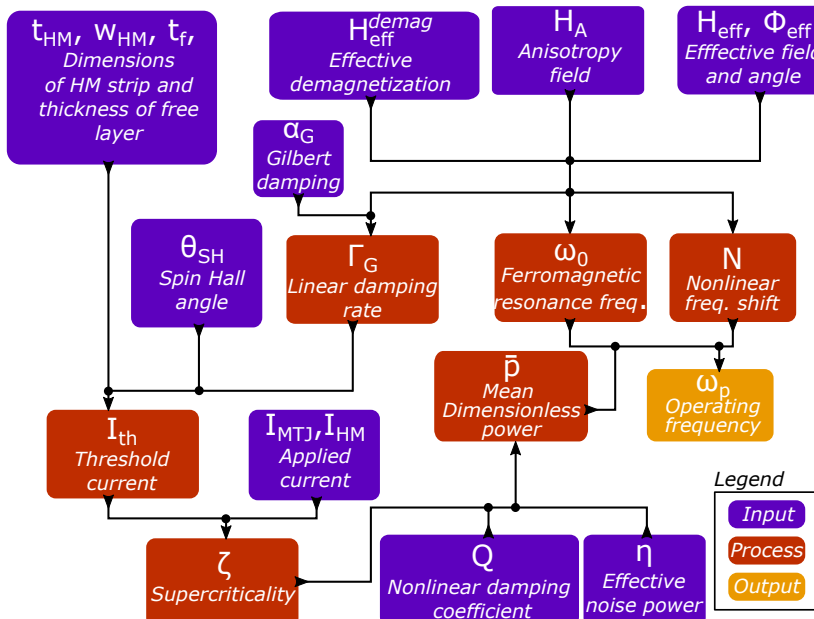


Figure 2.7: Flowchart for calculating the operating frequency.

$\bar{p}$  calculated according to eq. (84b) in [81], which includes the effect of thermal fluctuation, is used in (2.8a) instead of  $p$ . To distinguish between these two variables,  $p_0$  and  $\bar{p}$  will be used to annotate the stationary power and the mean power in the presence of thermal fluctuations, respectively. To find  $\omega_0$ ,  $N$  and  $\bar{p}$ , various other intermediate parameters need to be found from the input parameters in Table I, in [Paper I]. A detailed description of the equations is provided in [Paper I]. In Fig. 2.7, a flow chart is presented, describing the process of finding the operating frequency  $\omega_p$ . It is obvious that some of the input parameters are known quantities, e.g. the dimensions of the device and the applied current. The effective demagnetization field, the anisotropy field and the effective field have already been discussed in detail in Section 2.2.2. Here, the additional input parameters are the spin-hall angle  $\theta_{SH}$ , the Gilbert damping  $\alpha_G$ , the nonlinear damping coefficient  $Q$  and the effective noise power  $\eta$  [81].  $\theta_{SH}$  and  $\alpha_G$  are material dependent parameters which are generally obtained by characterization of the spintronic oscillator, while  $Q$  and  $\eta$  are considered fitting parameters in the macrospin approximation.

### 2.2.5 Output Power

The frequency of the AC component is determined by  $\omega_p$ . Now, the focus will be on the amplitude of  $V_{AC}$  which is set by the peak precession resistance. This AC component of the output voltage presented in Fig. 2.6(a) is generated by an oscillation of the magnetization around the effective magnetic field angle,  $\phi_{eff}$ . This oscillation is induced by cancelling the magnetization damping utilizing the spin current generated by the SHE, as it has been previously discussed. The time-dependent angle between the fixed and the free-layer magnetization can consequently be written as:

$$\phi_t = \phi_{eff} + \phi_{prec} \sin(\omega_p t) \quad (2.11)$$

where  $\phi_{prec}$  is the precision angle of the magnetization, which can be found as  $\phi_{prec} = 2\sin^{-1}(\sqrt{\bar{p}})$ . Introducing this in (2.1), the resistance of the MTJ can be written as:

$$R = \frac{R_{aps} + R_{ps}}{2} - \frac{R_{aps} - R_{ps}}{2} \cos(\phi_{eff} + \phi_{prec} \sin(\omega_p t)) \quad (2.12)$$

which can be expanded in terms of Bessel function of the first kind  $J_n(\phi_{prec})$  as [124]:

$$R = \left( \frac{R_{aps} - R_{ps}}{2} - \frac{R_{aps} - R_{ps}}{2} J_0(\phi_{prec}) \cos(\phi_{eff}) \right) + \\ (R_{aps} - R_{ps}) \cdot J_1(\phi_{prec}) \sin(\phi_{eff}) \sin(\omega_p t) - \\ (R_{aps} - R_{ps}) \cdot J_2(\phi_{prec}) \cos(\phi_{eff}) \cos(2\omega_p t) + \dots \quad (2.13)$$

where the first term on the right-hand side of the equation is the DC resistance (which is equal to (2.1), assuming a small  $\phi_{prec}$ ) and the second and third terms correspond to the first and second harmonic oscillations, respectively. From these expressions, the peak power of the first  $P(\omega_p)$  and second harmonic  $P(2\omega_p)$  delivered to a matched load can be found as it is shown in [124]. These equations allow us to extract the peak resistance precession for the first and second harmonic as (20a) and (20b), respectively in [Paper I] [84]. Based on these equations, the output voltage swing can be written as (22) in [Paper I], which includes contributions from both the first and second harmonic. Since the equations for the peak resistance include Bessel functions, which are not accessible in Verilog-A, the Bessel functions are approximated in terms of trigonometric functions [125].

### 2.2.6 Linewidth

The linewidth characterizes the phase noise of spintronic oscillators, which is important for accurate behavioural modeling. The linewidth is defined as the width of the frequency spectrum at half the maximum power. The phase noise is usually determined by the thermal noise and the  $1/f$  noise. Thermal noise generally dominates the phase noise in spintronic oscillators for shorter time-scales, while  $1/f$  noise can contribute significantly on longer time-scales (i.e. at small offset frequencies from the fundamental) [126, 127]. Thermal noise properties

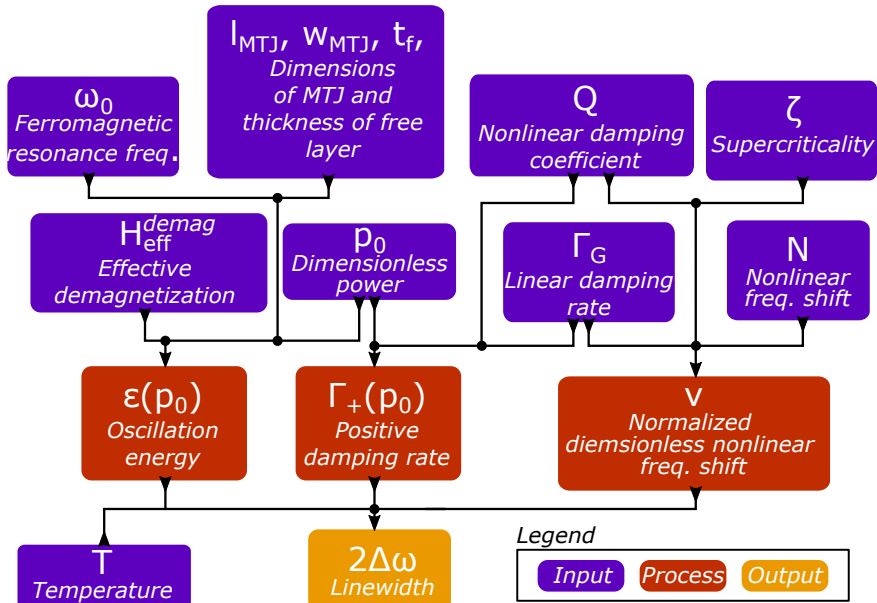


Figure 2.8: Flowchart for calculating the linewidth.

of spintronic oscillators have been extensively studied both experimentally [128] and theoretically [81], while the impact of  $1/f$  noise has been studied only recently [126, 127]. In [Paper I], the thermal noise has been considered to be the dominant noise contributor, the same as in other previously developed spintronic oscillator models. However, the  $1/f$  noise can play an important role, especially on longer time-scales. This results in a power-spectral-density (PSD) that resembles a Gaussian distribution rather than the Lorentz form that it is generally observed when only thermal noise is considered [127]. The behavioural model proposed here could be easily extended to include the effects of  $1/f$  noise.

To model the linewidth, the same approach as in [84], which is based on the macrospin approximation in [81], is employed. The characteristics of the phase noise are divided into three different regions, the sub-threshold region for  $I_{HM\text{-eff}} < I_{th}$ , the near-threshold region for  $I_{HM\text{-eff}} \approx I_{th}$  and the above-threshold region for  $I_{HM\text{-eff}} > I_{th}$ . A detailed presentation of the equations describing the linewidth in each of these regions is provided in [Paper I]. Similarly to the operating frequency, multiple intermediate parameters need to be calculated based on the macrospin approximation before the linewidth can be found. A flowchart describing the process of calculating the linewidth is presented in Fig. 2.8.

### 2.2.7 Verilog Implementation and Cadence Simulation Results

The described behavioural model was implemented in Verilog-A, which allows for Cadence simulations together with CMOS circuits. Verilog-A is a standard behavioral hardware description language used to model analog electrical circuits and devices. All the input parameters to the behavioural model are listed in Table I in [Paper I]. As previously highlighted, these parameters are either material characteristics obtained from experimental measurements or fitting parameters. By using these parameters along with the previously presented equations, all the values entering the expression for  $V_{out}$  (equation (22) in [Paper I]) are found.

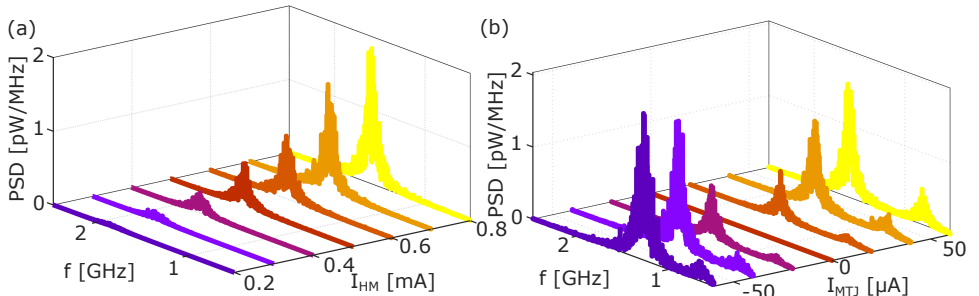


Figure 2.9: PSD of the output (a)  $I_{MTJ} = 60 \mu\text{A}$  and (b)  $I_{HM} = 0.8 \text{ mA}$  while sweeping  $I_{HM}$  and  $I_{MTJ}$ , respectively.

These calculations are performed during an initial step, before the transient Cadence simulation starts, which allows for rapid simulations compared to having to re-calculate all the values at each step [120]. However, the disadvantage of this approach is that the parameters, such as the applied current or applied magnetic field, can not be changed during the transient Cadence simulations. This can be addressed at the cost of significantly longer simulation times as it will be discussed in Section 2.3.4.

After the initialization step when all parameters are calculated, an output voltage using (22) in **[Paper I]** is generated at each simulation time-step,  $\Delta_t$ . The PSD of  $V_{out}$  as a function of the currents  $I_{HM}$  and  $I_{MTJ}$  are presented in Fig. 2.9. As it is discussed in detail in **[Paper I]** the main characteristics, such as frequency, power and linewidth of the modeled device are extracted and compared to the measurement results in [67]. This is done by sweeping  $I_{MTJ}$  from  $-60 \mu A$  to  $60 \mu A$  while keeping  $I_{HM} = 0.8 mA$  constant and subsequently keeping  $I_{MTJ} = 60 \mu A$  constant while sweeping  $I_{HM}$  from  $0.2 mA$  to  $0.8 mA$ . These current sweeps are performed at  $\phi_{ext} = 2^\circ$  and  $\phi_{ext} = 8^\circ$ , respectively as it is highlighted in **[Paper I]**. Comparing these PSDs to the measurement results presented in [67], it demonstrates that the overall behaviour closely resembles the measurement results. Specifically, the peak at the fundamental, which is also present in the experimental measurements when  $I_{MTJ}$  is swept, is accurately captured with the behavioural model. This characteristic is also evident in the transient response presented in Fig. 2.10, where the second harmonic is dominant for small  $\phi_{ext}$ , while the fundamental and second harmonic contribute to the output signal at moderate  $\phi_{ext}$ . Finally, for moderately large external angles,  $\phi_{ext} \geq 20^\circ$ , the fundamental dominates and the second harmonic is completely suppressed. This behaviour is also consistent with other measurement results from literature based on MTJ STNOs [129], when  $\phi_{ext}$  is increased from  $\approx 0$  to higher angles, and it is a consequence of the behaviour described by (20a) and (20b) in **[Paper I]**. This behaviour is generally called intrinsic frequency

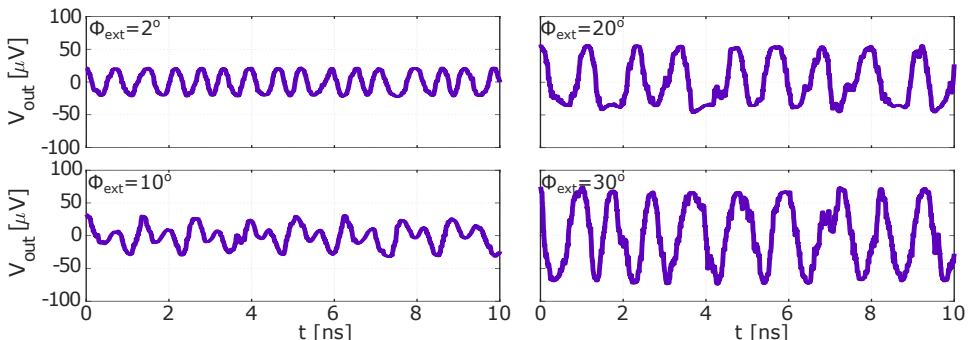


Figure 2.10: Transient of the output signal for different external field angles  $\phi_{ext}$  (DC component has been left out for clarity).

doubling, as it is discussed in detail in [Paper I] [129].

### 2.2.8 Limitations and Future Work

The proposed behavioural model can accurately capture all of the major characteristics of three-terminal SHNOs and the Cadence simulation results closely resemble the experimental results from [67]. However, as it was previously mentioned, the behavioural model has certain limitations. Arguably, the most important limitation is the lack of dynamically adjusting the parameters, including the applied current or external magnetic field as a function of time. As it has been mentioned, this can be addressed at the cost of longer simulation times, by slightly modifying the behavioural model. Additionally, the proposed behavioural model was only verified against one measured device from literature. To further validate the proposed model, fitting the model to other experimental results of three-terminal SHNOs is required. Finally, to analyse the behaviour of coupled networks of three-terminal SHNOs, as previously discussed, the behavioural model needs to be extended to include characteristics such as synchronization properties.

## 2.3 Magnetic Field-to-Digital Conversion using Spintronic Oscillators

Spintronic oscillators exhibit various promising characteristics, including high operating frequency, nanoscale size and nanosecond turn on times, as previously discussed. However, with the current maturity of the technology, many applications are limited by their disadvantages, including low output power, the need for an external magnetic field and the poor phase noise performance. A potential application that could benefit from the current maturity of spintronic oscillators is the magnetic field sensor. The possibility of realizing a magnetic field sensor based on spintronic oscillators was explored and proposed in [110]. Since spintronic oscillators are extremely sensitive to changes in the applied magnetic field, as it has been shown in literature (also, seen in e.g. Fig. 5 in [Paper I]), the proposal in [110] is based around using this property to realize magnetic field sensors.

In [Paper II] the possibility of realizing a magnetic field sensing system based on spintronic oscillators is explored. Most magnetic field sensors used in modern applications are based on voltage or current changes as a function of measured magnetic field. On the other hand, spintronic oscillators respond to variations in the external magnetic field through a change in their operating frequency. This change in the operating frequency can be multi GHz for relatively small variations in the applied field. This property in combination with the extremely small size of spintronic oscillators make it a promising technology to realize magnetic field sensors. However, the need to continuously extract the instantaneous operating

frequency of the spintronic oscillator could introduce significant complexity in the read-out (compared to voltage or current based sensors). In [Paper II], the possibility of addressing this challenge is explored by inspiring from time-based ADCs which also bring the advantages of noise-shaping. In this section, the most commonly used magnetic field sensors are first discussed and the STNOs properties for magnetic field sensors are introduced. Next, the fundamentals of time-based ADCs are introduced and their advantages and challenges are briefly discussed. Finally, the main idea explored in [Paper II], a magnetic field sensor, which takes advantage of VCO-based ADCs properties and the operation of spintronic oscillators as magnetic field sensor, is discussed.

### 2.3.1 Magnetic Field Sensors

Magnetic field sensors have been explored for various applications, including position sensing [130–132], nondestructive evaluation/monitoring [133, 134], biomedical [135, 136] and vehicular [130] applications, etc. Hall-effect, AMR, GMR, TMR and giant magnetoimpedance (GMI) sensors [137, 138] are the most popular sensors explored for many of the previously discussed applications, requiring reasonable performance and a compact area. Consequently, the focus of this section is limited to these sensors.

The most extensively used magnetic field sensors are Hall-effect sensors. Hall-effect sensors are based on the Lorentz force exerted on electrons flowing in a conductor, which is exposed to an external magnetic field. As was discussed in relation to the SHE, this results in a measurable voltage transverse to the current flow, as presented in Fig. 2.11(a). The material of the conductor (usually a semiconductor) largely determines the sensitivity and performance of the sensor. Currently, the most popular implementation is employing silicon instead of other materials which exhibit in principle better characteristics for Hall-effect sensors (e.g. GaAs or InAs), due to its compatibility with CMOS technology [138]. Hall-effect sensors also have various disadvantages, including a small output signal and temperature drift, which require amplification and calibrations in the sensor read-out.

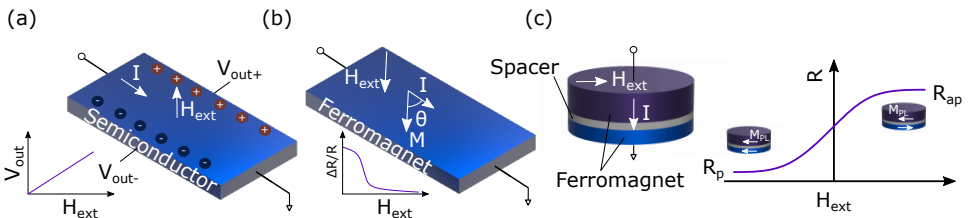


Figure 2.11: Illustrations of different magnetic field sensors (a) Hall-effect, (b) AMR and (c) GMR/TMR.

The AMR, GMR and TMR effects have previously been introduced in relation to STNOs and SHNOs, but will be briefly highlighted again here with special focus on how they are employed for magnetic field sensing applications. When these effects are used to realize magnetic field sensors, no magnetization precession is excited. Instead, the DC resistance of the device (for AMR a FM stripe, for GMR a spin-valve and for TMR a MTJ) is simply used to detect either the orientation or the magnitude of the applied magnetic field. The AMR effect is based on a change in the FM conductance depending on the angle between the magnetization  $M$  and the direction of the current flow  $I$ . Since the direction of the magnetization depends on the external magnetic field  $H_{ext}$ , this property can be used to realize magnetic field sensors. A simple illustration of the AMR effect is presented in Fig. 2.11(b). The most popular material used to realize AMR sensors is a composition of iron and nickel, generally referred to as Permalloy. AMR sensors are cheap and can be easily fabricated, but generally exhibit lower sensitivities compared to the more expensive counterparts, GMR and TMR based sensors. As previously discussed, the GMR and TMR effects exhibit very similar characteristics, but are realized in different material stacks (with a metallic or insulating spacer, respectively). The basic operating principles of GMR and TMR sensors are presented in Fig. 2.11(c), highlighting that a parallel and antiparallel magnetization orientation in the two FM layers results in a change in the overall resistance of the device. Consequently, when a magnetic field is applied, the device shows a gradual transition from a low resistance state  $R_p$  to a high resistance state  $R_{ap}$ , which is a function of the applied magnetic field. The major advantage of GMR/TMR effect based sensors is that they can be realized in extremely compact form factors with  $\mu\text{m}$  sizes. Moreover, TMR sensors generally have the best performance out of MR sensors, but are also the most expensive. As a consequence of the compact form factor, the TMR and GMR devices have been realized in arrays to increase the performance compared to a single stand-alone device, or to explore applications benefiting from spatial resolution [133]. Other applications of GMR and TMR sensors include crank shaft speed or rotor position measurements in vehicles, eddy current testing, space applications and many more [130].

Finally, GMI sensors are based on the impedance change of a FM conductor carrying an AC current, in the presence of a magnetic field. This phenomena is a result of the skin-effect and its dependence on the magnetic permeability. Among all magnetic field sensors discussed in this section, only this one is based on applying an AC signal to read-out the strength of the applied magnetic field. GMI sensors can generally detect smaller magnetic fields than the previously discussed MR sensors, but their size is also in the millimeter range [138].

A comparison, in terms of measurement range and size, between the magnetic field sensors discussed in this section is presented in Fig. 2.12 along with superconducting magnetic field sensors (SQUIDS) and flux gate sensors which are generally used in high resolution applications and are consequently targeted at different applications [138].

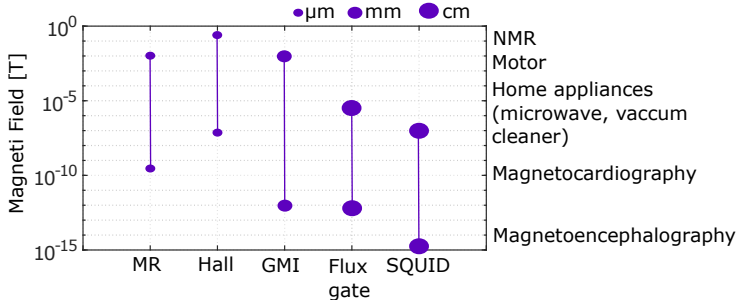


Figure 2.12: Comparison of magnetic field sensors typical range and size (inspired by Fig. 21 in [138])

### 2.3.2 Spintronic Oscillators as Magnetic Field Sensors

The possibility of using spintronic oscillators as magnetic field detectors in different applications has been studied. Specifically, utilizing spintronic oscillators as magnetic read heads in hard-disk drives [110,139–141], as biosensors [113,136,142] and for scanning probe nanoscale magnetometry [143] has been explored. Moreover, in [143] the possibility of improving the performance of spintronic oscillator magnetic field sensors by synchronizing four nanoconstriction SHNOs was explored. This approach reduces the phase noise compared to a single standalone oscillator, which translates to a better performance. This implementation showed promising performance, outperforming many TMR, GMR and Hall-effect sensors in terms of resolution in a small sensing area as it is shown in [143].

Spintronic oscillator-based magnetic field sensors are based on changes in the operating frequency as a function of the applied magnetic field, as it is shown in Fig. 2.13. Consequently, the achievable resolution is proportional to the frequency tunability  $K_{STNO} = df_{STNO}/dH_{ext}$ , with  $f_{STNO} = 2\pi \cdot \omega_p(p)$  being the operating frequency and  $H_{ext}$ , the applied field. Experimentally,  $K_{STNO}$  values approaching 180 GHz/T have been demonstrated for optimized geometries and materials [110,144]. Another important performance metric of spintronic oscillators for magnetic field sensing is the phase noise. As it is detailed in [110], the

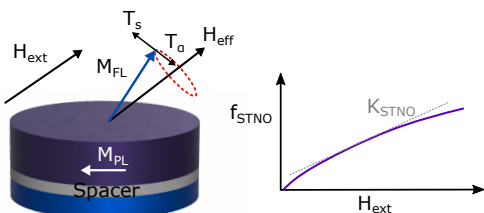


Figure 2.13: STNO as a magnetic field sensor.

achievable SNR is inversely proportion to the linewidth  $\Delta f = 2\pi \cdot (2\Delta\omega)$  and consequently, achieving a large ratio of  $K_{STNO}/\Delta f$  is important for high resolution applications. Although spintronic oscillators exhibit relatively poor phase noise performance, the continuous efforts to reduce the phase noise using synchronization among multiple oscillators or by other methods, make them an interesting candidate for next generation magnetic field sensors.

Spintronic oscillator-based magnetic field sensors inherently respond to a change in the magnetic field with a change in frequency, which makes them very different than the previously discussed magnetic field sensors. As previously highlighted, to detect/sense or measure a change in the magnetic field, the frequency of the oscillator consequently needs to be extracted. The most straightforward way to achieve this, is by digitizing the STNO output signal and taking the Fourier transform. However, this is a cumbersome task that requires RF frequency ADCs, or alternatively, a frequency-to-voltage converter followed by an ADC. An alternative and potentially more efficient approach, which is based on so-called VCO-based ADCs, is explored in [Paper II] and discussed in the following subsections.

### 2.3.3 VCO-based ADCs

Analog-to-digital converters play a key role in modern electronic systems with applications that include data acquisition, communications, measurement and instrumentation, sensing, etc. With the continuously smaller MOSFET transistor dimensions, implementing high performance ADCs becomes challenging. Specifically, the lower intrinsic gain of short channel transistors can potentially lead to increased circuit complexity and higher power consumption to meet the design constraints. Secondly, the supply voltage decreases in smaller technology nodes, which limits the achievable voltage swing and consequently the SNR. In addition, mismatches and noise introduce additional challenges when designing analog circuits in advanced CMOS technology nodes [13, 145]. Among traditional ADC architectures, the successive approximation register (SAR) ADC overcomes many of these challenges due to its highly digital nature and resilience to low supply voltages [145, 146]. In the last decade, new ADC architectures, generally called time-based ADCs have received a significant interest from the research community, due to their potential to provide energy-efficient solutions. The main idea behind this approach is to process analog signals in time domain as it is

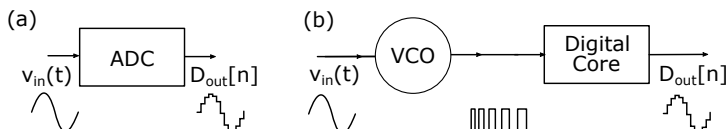


Figure 2.14: (a) Conventional ADC and (b) VCO-based ADC.

presented in Fig. 2.14 rather than voltage domain. Consequently, time-based ADCs can benefit from advanced CMOS technology nodes since the gate delay of digital gates reduces in smaller nodes which leads to increased resolution in time [145]. Since time-based ADCs utilize delay cells and ring oscillators to encode information, reduced gate delay generally improves the achievable performance. However, in advanced technology nodes the performance becomes limited by mismatch which is the main bottleneck of many time-based ADCs.

There exist a vast amount of time-based ADC architectures, based on VCOs [147] or delay cells [148] or even a combination of time-domain approaches with traditional ADC architectures, such as SAR ADC [145]. For the purpose of magnetic field sensing using spintronic oscillators, VCO-based ADCs are of interest. Consequently, this section focuses on the simple open-loop VCO-based ADC architecture presented in Fig. 2.15(a). The operation of this ADC is explained in detail in [Paper II]. In brief, the VCO translates the input voltage  $v_{in}(t)$  into a frequency modulated signal  $f_{VCO}(t)$  through  $K_{VCO} = df_{VCO}/dV_{in}$  which is the frequency tunability of the VCO as a function of  $v_{in}$  (frequency gain), as it is presented in Fig. 2.15(b). This frequency modulated signal is then applied to a counter which is sampled by a clock  $f_s$ . The count within each sampling period is proportional to the average analog input voltage during the period  $T_s = 1/f_s$ . As it is highlighted in [Paper II] and in the equivalent frequency domain model in Fig. 2.15 (a), the VCO acts like a time domain integrator since the residual phase during the previous sampling period  $T_s$  inherently becomes the initial phase of the current period. Consequently, the counter acts like a time or phase domain quantizer, which has a quantization step of  $2\pi$ . As it has been shown [149] and it is also highlighted in [Paper II] and Fig. 2.15, this simple open-loop VCO-based ADC provides noise-shaping of the quantization noise and consequently, resembles a noise-shaping ADC behaviour. Specifically, the signal-to-quantization noise ratio (SQNR) of these architectures can be derived as [150]:

$$SQNR \approx 6.02N_q - 3.41 + 30\log_{10}(OSR) \quad (2.14)$$

where OSR is the oversampling ratio  $OSR = f_s/(2f_{bw})$ ,  $f_{bw}$  is the signal band-

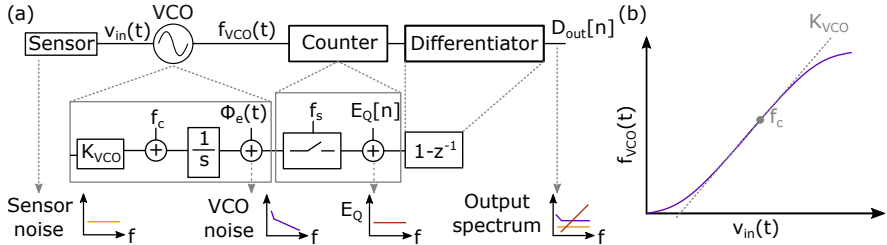


Figure 2.15: (a) VCO-based ADC and equivalent frequency domain model highlighting different noise sources and (b) transfer characteristics of a VCO from voltage to phase domain.

width,  $N_q = \log_2(2AK_{VCO}/f_s)$  is the quantizer resolution and A is the maximum amplitude of the sensor voltage  $v_{in}(t)$ . From this expression, it can be observed that VCO-based ADCs can benefit from a large  $K_{VCO}$  and sampling frequency  $f_s$ . Specifically, doubling  $K_{VCO}$  results in a 6 dB (1 bit) improvement of SQNR, and by doubling also  $f_s$  results in a total improvement of SQNR by 9 dB (1.5 bit) [13]. It is worth highlighting that VCO-based ADCs can be designed to operate in either oversampling mode, when  $f_s >> 2f_{bw}$ , or in Nyquist mode, depending on the application and desired characteristics [149]. However, VCO-based ADCs also suffer from various challenges. Since the analog input voltage is effectively encoded into the edge positions of a square wave, phase noise impacts the operating behaviour in a similar way as thermal or flicker noise in conventional ADCs [13]. Moreover, nonlinearity in the voltage-to-frequency conversion  $K_{VCO}$  introduces distortions at harmonics of the fundamental, which can significantly deteriorate the performance of VCO-based ADCs. To address this nonlinearity, calibration techniques for open-loop VCO-based ADCs are generally employed [147, 149]. Alternatively, another approach is based on closing the loop, which introduces a feedback loop with a DAC, leading to increased complexity [150]. However, considering their highly digital nature, the time-based ADCs are a promising approach for realizing high performance ADCs in advanced CMOS technology nodes.

The resemblance between the VCO-based ADC and a spintronic oscillator operating as a magnetic field sensor is relatively obvious. In VCO-based ADCs, the sensor in combination with the VCO translates the quantity to be measured to a frequency modulated signal. Similarly, as it was presented in the previous section and it is highlighted in Fig. 2.13, spintronic oscillators convert the externally applied magnetic field into a frequency modulated signal when the biasing current of the oscillator is fixed. Consequently, a spintronic oscillator-based magnetic field sensing system can be realized by simply replacing the sensor and VCO in time-based ADCs by a spintronic oscillator. In this way, the magnetic field-to-digital conversion is directly realized by using the frequency modulated output of the spintronic oscillator. This is the fundamental idea explored in [Paper II].

### 2.3.4 Proposed Implementation and Simulation Results

As it is highlighted in Fig. 3 in [Paper II], the proposed architecture consists of an STNO, a low-noise amplifier (LNA)+amplifier chain and a digital core, which performs quantization and signal conditioning. It is worth highlighting that the MTJ STNO was employed in this architecture rather than e.g. three-terminal SHNOs or nanoconstriction SHNOs since MTJ STNOs have been studied for longer and consequently, can be considered as relatively mature compared to the other spintronic oscillators (although all spintronic oscillators are in general an emerging technology compared to e.g. CMOS). The LNA+amplifier chain providing the required gain, is followed by the digital core consisting of a counter, decoder and differentiator (sampling flops and subtractor). The basic operation

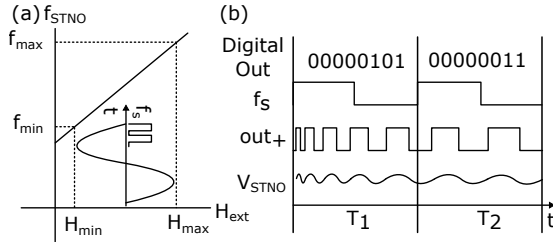


Figure 2.16: (a) Magnetic field to frequency conversion using an STNO and (b) signals at different points in the proposed architecture presented in Fig. 3 in [Paper II].

behaviour of this system is shown in Fig. 2.16, which presents the signal at different stages in the proposed architecture. Fig. 2.16(a) shows how the STNO converts the magnetic field to a frequency modulated signal through  $K_{STNO} = df_{STNO}/dH_{ext}$ . The STNO is assumed to be biased with a DC magnetic field that is half way between a minimum  $H_{min}$  and a maximum  $H_{max}$  applied field, which results in a free running frequency  $f_c$ , when  $H_{ext} = 0 \text{ Oe}$ . Consequently, the STNO converts the applied magnetic field  $H_{ext}$  into a frequency modulated signal  $V_{STNO}(f_{STNO})$ , where  $f_{STNO} = f_c + K_{STNO}H_{ext}$ , similar to how VCO-based ADCs convert the input voltage to a frequency modulated voltage signal. This voltage is then amplified by the LNA+amplifier chain and fed to a counter sampled at a frequency  $f_s$ , as presented in Fig. 2.16(b). Finally, the differentiator extracts the number of rising edges that arrived during the sampling period, which is proportional to the applied magnetic field. Moreover, similar to the VCO-based ADC, both the quantization and phase noise are noise-shaped by this architecture which could bring additional advantages compared to a more conventional read-out as previously discussed.

As it is presented in detail in [Paper II], behavioural simulations in Cadence were performed to validate the functionality of the proposed architecture and to demonstrate the potential of employing STNOs as magnetic field sensors (or magnetic field-to-digital converter). The behavioural model of MTJ STNOs previously developed within the group was considered [84, 120] for this purpose. However, this behavioural model was designed only considering steady state transient simulations, i.e. it was not possible to adjust the biasing current or the externally applied magnetic field during transient simulations in Cadence. The most straightforward way to allow for dynamically changing the applied field, is to simply calculate all of the parameters in the behavioural model during each simulation step  $\Delta t$  and integrate the instantaneous frequency,  $f_{STNO}(t)$ . However, this results in extremely long simulation times since the simulation time step  $\Delta t$  is fixed to values  $\ll 1/f_{STNO}$ , for generating the phase noise in the output signal (as it is discussed in [120]). To overcome this issue, the MTJ STNO behavioural model was re-designed in the form of a look-up table (LUT). Specifically, before

the start of the Cadence simulation, the parameters entering the expression for  $V_{STNO}$ , for different values of  $H_{ext}$ , are stored in a table. Then, during the simulations, the instantaneous  $V_{STNO}(t)$  is simply found by interpolating the values in the LUT. This allows for significantly faster Cadence simulations compared to calculating all of the parameters during each simulation step. However, as it is discussed in [Paper II], the Cadence simulations for extracting the output spectra are still extremely long, as a consequence of the phase noise generation. This limits the analysis to spectra with relatively few fast Fourier transform (FFT) points, e.g. the data in [Paper II] is extracted with  $NFFT = 4096$ .

The main focus of this study was to explore the potential of using spintronic oscillators as magnetic field sensors and it was expected that the STNO phase noise would be the limiting factor of the design. Therefore, relatively simplistic behavioural models of the read-out were employed. The LNA's behavioural model is based on [151], but with parameters inspired by an LNA+amplifier chain, which was previously developed within the group for STNOs [152]. As it is discussed in [Paper II], the digital core can be implemented using a high-speed asynchronous ripple counter in combination with asynchronous double sampling [147]. As it is detailed in [147], this counter can operate at extremely high frequencies (up to 15 GHz). However, since the counter operates asynchronously relative to the sampling clock, special measures must be taken to prevent metastability in the sampled values. In [147], this is addressed utilizing a fast differential sampling flip-flop in combination with asynchronous double sampling. However, for the purpose of exploring the proposed architecture, the digital core was modeled using ideal digital cells. All Cadence simulations and analysis are presented in [Paper II] and it demonstrates that the achievable performance is limited by phase noise. This can be further confirmed by simulating the architecture in the absence of any phase noise, i.e. assuming the linewidth  $\Delta f = 0 \text{ Hz}$ . Since this approach allows for much faster Cadence simulations, it can also be performed for a much higher number of NFFT. The PSD of the output signal in the absence of phase

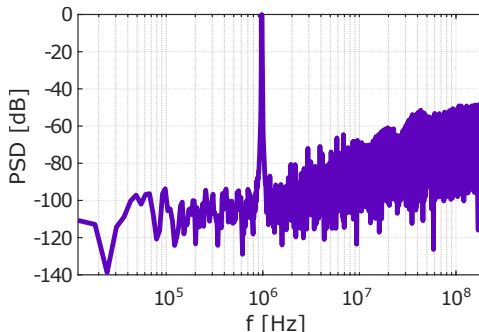


Figure 2.17: Output spectrum of the proposed architecture for  $f_{in} \approx 1 \text{ MHz}$ ,  $f_s = 400 \text{ MHz}$  and  $NFFT = 65536$  in the absence of phase noise, i.e.  $\Delta f = 0$ .

noise is presented in Fig. 2.17. Comparing Fig. 2.17 to Fig. 6 in [Paper II], the impact of the phase noise can be clearly observed. Specifically, the phase noise raises the noise floor, limiting the achievable SNR performance. These results are consistent with analysis of phase noise in VCO-based ADCs [150]. Additionally, the noise-shaping of the quantization noise in Fig. 6, in [Paper II] is not very apparent as a consequence of the phase noise, but in Fig. 2.17, it clearly exhibits a 20 dB/dec slope as expected for the 1st order noise-shaping.

Based on the analysis in [Paper II], additional conclusions about the proposed architecture can be drawn by interpolating the results using the theoretical equations. Specifically, for the phase noise considered in [Paper II], the proposed architecture benefits negligibly from oversampling unless it is for extremely wide bandwidth applications, where SQNR starts impacting the overall performance. However, with the continuous efforts to reduce the phase noise of spintronic oscillators, it is expected that the linewidth will be decreased in future implementations. Consequently, it was decided to further explore this potential. If the phase noise decreases, the benefit of oversampling becomes apparent for reasonable bandwidths as it is presented in Fig. 2.18 for two different  $f_{bw}$  and four different values of the phase noise. From these results, it can be concluded that applications requiring wide bandwidth benefit from oversampling. It is worth highlighting that the simulations in Fig. 2.18 are for the SNR (quantization and phase noise) and do not consider distortions. For narrow bandwidth applications, the architecture can be operated in the Nyquist-sampling mode since oversampling provides negligible performance enhancements for typical STNO phase noise characteristics. In Fig. 2.19, the SNR is calculated for lower  $f_{bw}$  than are analyzed in [Paper II] utilizing the analytical equations. As it can be seen in this figure, the SNR approaches 70 dB for  $f_{bw} = 10 \text{ kHz}$  which corresponds to a quantization step of  $\approx 30 \mu\text{T}$ , assuming that distortions can be calibrated out. However, since the resolution of the quantizer (the counter) is proportional to  $f_{STNO}/f_s$ , this

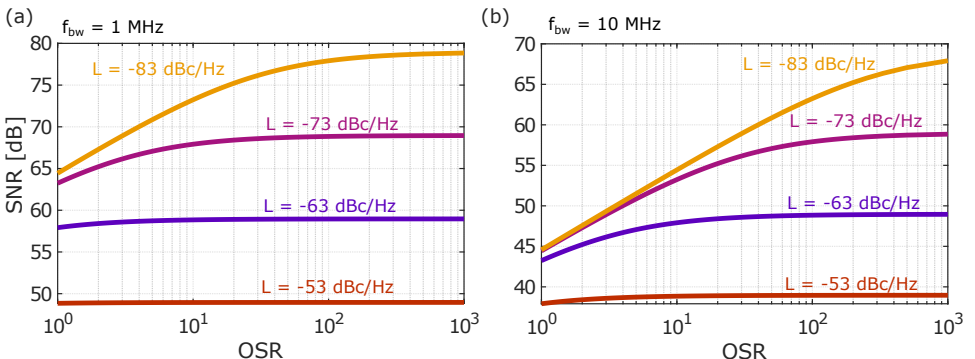


Figure 2.18: Achievable SNR as a function of the phase-noise at 1 MHz offset for (a)  $f_{bw} = 1 \text{ MHz}$  and (b) 10 MHz.

approach would require a high number of bits in the counter ( higher than the 8-bits used in the Cadence behavioural simulations) and consequently, increased area.

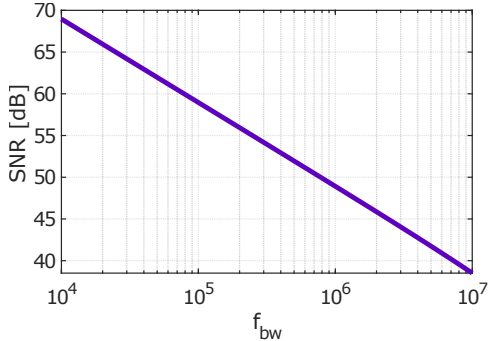


Figure 2.19: SNR as a function of  $f_{bw}$  assuming  $f_s = 5f_{bw}$  calculated with equations (6)-(9) in [\[Paper II\]](#).

### 2.3.5 Limitation and Future Work

The possibility of utilizing spintronic oscillators as magnetic field sensors has been explored. As it was highlighted by the behavioural simulation results from Cadence, the resolution of the proposed system is limited by the STNO phase noise. To be able to evaluate the performance of the proposed magnetic field sensing system, the detectivity of the architecture can be approximated from the PSD in Fig. 6 in [\[Paper II\]](#) as  $\approx 3 \mu T/\sqrt{Hz}$  which is comparable to the implementation based on four nanoconstrictions SHNOs in [143]. Compared to state-of-the-art magnetic field sensors based on the previously discussed MR effects, this approach has comparable performance with magnetic field sensors of similar size [143]. However, as it was previously discussed, the performance of the proposed implementation can be improved by using networks of synchronized oscillators to reduce the phase noise and/or by optimizing the geometry and material parameters, to increase  $K_{STNO}$ . Consequently, with further developments, spintronic oscillator-based magnetic field sensors could potentially outperform currently available magnetic field sensors.



## Chapter 3

# Ising Machines using Networks of Coupled Oscillators

In recent years, the interest in unconventional computing, such as analog or probabilistic computing has surged. This is partially motivated by the immense interest in machine learning. However, specialized architectures, such as IMs, targeting hard CO problems have also received increased interest. IMs are hardware architectures designed to solve the Ising model, which is a mathematical model from statistical mechanics. This interest is motivated by the fact that recently, it was shown that many practically relevant optimization problems can be mapped to the Ising model [153]. Consequently, if a hardware architecture can solve the Ising model efficiently, many other practically relevant problems can also be solved using the same hardware. As it was also recently demonstrated, coupled oscillator networks can be used to realize IMs [21]. This approach is based on the dynamics of coupled oscillator networks when phases are binarized using second harmonic injection locking (SHIL).

In this chapter, the Ising model and IMs will be reviewed. The fundamental concepts governing the operation principles and state-of-the-art IMs will be presented, with a special focus on oscillator-based IMs which are the topics of **[Paper III]** and **[Paper IV]**. Specifically, **[Paper III]** explores the possibility of realizing oscillator-based IMs using spintronic oscillators, while in **[Paper IV]** a new implementation of oscillator-based IMs, targeting reconfigurability, is explored. A new approach for implementing IMs based on coupled Duffing oscillators, presented in **[Paper V]**, is finally discussed. Supporting information and additional results to these papers are presented in the following sections.

## 3.1 Ising Machines

### 3.1.1 Optimization Problems

CO problems are known for being extremely challenging to solve. The difficulty of solving these problems, called nondeterministic polynomial time (NP) CO problems, appears as a result of the immense amount of resources required, as the problem becomes bigger [154]. The most widely known NP-hard CO problem is the traveling salesman problem (TSP) which is illustrated in Fig. 3.1(a). The TSP consists of finding the shortest possible route between  $N$  cities, which are located a distance  $D$  apart, when starting and ending in the same point. Another popular CO problem is the knapsack problem which involves ordering items in a bag, maximizing the worth  $\$$  of the items, while the total weight cannot exceed a certain amount  $W_{max}$  [154]. This is illustrated in Fig. 3.1(b) along with one possible solution. Various other problems include number or graph partitioning, graph coloring, satisfiability problems, etc [153]. While the description of these problems is relatively simple, calculating all the possible solutions and finding the optimal choice becomes intractable even for moderately small problems. Exact algorithms, such as variation of the branch-and-bound and cutting planes algorithms, avoid having to use the brute force method of calculating all possible solutions, but they often scale inefficiently with problem size [155]. Alternative approaches, which are commonly used for moderate to large problems to speed up finding the solution, are so-called heuristic algorithms, e.g. Simulated Annealing (SA) [156]. These algorithms try to approximate the optimal solution, but do not guarantee it. While the previously discussed problems are popular examples to demonstrate the challenges associated with solving CO problems, they appear in various practically relevant applications including scheduling/planning tasks [157, 158], machine learning [159, 160], chemistry [161, 162], etc. Consequently, it is extremely desirable to have a general purpose and efficient approach which can be applied to a wide range of CO problems.

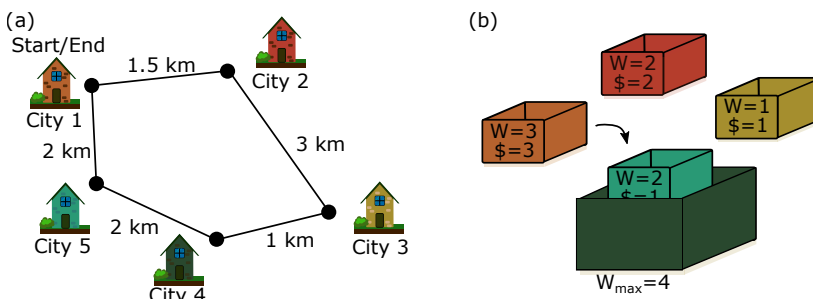


Figure 3.1: (a) The TSP problem for 5 cities and one possible route (b) the knapsack problem.

All previously discussed algorithms have in common that they are generally run on conventional von Neuman computing architectures and consequently, mostly serially executed. However, in recent years the possibility of developing new hardware architectures, which are highly parallel and specifically designed to speed up the time to solve CO problems, have received interest from the research community. IMs are among these hardware architectures, which have shown promising performance, drastically outperforming algorithmic approaches such as SA running on conventional hardware. This emerging approach will be introduced in the following sections.

### 3.1.2 Ising Model

The Ising model was first explored by Ernst Ising in the 1920s [163]. Primarily, this model is used to study ferromagnetism and considers a system of  $N$  discrete variables, referred to as spins. The Ising Hamiltonian, which describes the Ising model, can be written as

$$H(s) = -\frac{1}{2} \sum_{i,j,j \neq i}^N J_{ij} s_i s_j - \sum_{i=1}^N h_i s_i \quad (3.1)$$

where  $N$  is the total number of spins,  $J_{ij}$  is the coupling between spins,  $s_i/s_j$  are spin variables defining the state of spin  $i/j$  taking a value of 1 or  $-1$ , and  $h_i$  is generally referred to as the external field term. The coupling between spins in (3.1) is FM (i.e. spins prefer to align in the same direction) if  $J_{ij} > 0$ , while it is antiferromagnetic (AFM) (prefer to align in the opposite direction) if  $J_{ij} < 0$ . The field term,  $h_i$ , describes a bias of spin  $i$  to favor one of the two possible states  $1/-1$ . The solution (ground-state) of the Ising Hamiltonian refers to the state of the variables  $s$  that minimizes  $H(s)$  for a certain set of couplings  $J_{ij}$  and field terms  $h_i$  and it is generally an NP-hard problem [164]. A simple example consisting of

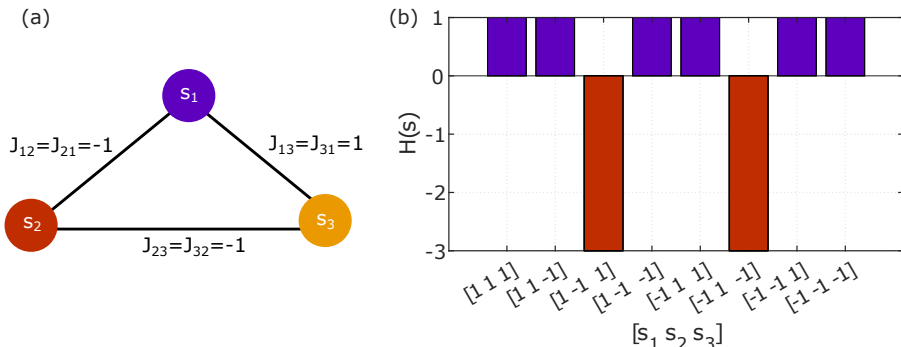


Figure 3.2: (a) A simple three spin system and (b) the energy  $H(s)$  associated with different spins configurations.

3 coupled spins is presented in Fig. 3.2 (a) where  $h_i = 0$ . For simplicity, the field term  $h_i$  has been fixed at zero and consequently, the Hamiltonian can be written as:

$$H(s) = -\frac{1}{2} \sum_{i,j, j \neq i} J_{ij} s_i s_j \quad (3.2)$$

All possible spin configurations for the 3 spin system are presented in Fig. 3.2 (b) along with the associated energy  $H(s)$  calculated with (3.2). As it can be seen in Fig. 3.2 (b), this example has two ground states that minimize  $H(s)$ , to  $H(s) = -3$ . Moreover, these two ground states are degenerate states since  $[1, -1, 1] = (-1) \cdot [-1, 1, -1]$  and effectively correspond to the same solution. For such a small problem, exploring all possible spin configurations is simple to do, as it was shown here, but the number of configurations grows as  $2^N$  with increasing size. Therefore, this approach becomes quickly impractical even for moderately small spin networks. For example, a spin network of  $N = 100$  has  $\approx 1.27 \cdot 10^{30}$  possible configurations. Consequently, more advanced methods are generally employed to find the ground-state of (3.2). SA [156], which emulates the physical equivalent of heating a material and then cooling it to minimize the energy of the system, is one of the most common approaches for finding the ground state. Alternatively, Monte Carlo (MC) algorithms, such as parallel tempering MC [165] and population MC [166] are commonly used for solving the Ising model and can provide advantages over SA.

The previously presented example in Fig. 3.2(a) consists of a coupled spin network defined by the Ising Hamiltonian in (3.2). However, it has been shown that various practically relevant problems can be mapped to the Ising Hamiltonian by representing them as spin networks [153]. The simplest optimization problem to map to the Ising Hamiltonian is the Max-Cut problem. The Max-Cut problem is a NP-hard optimization problem, which has applications in very large scale inte-

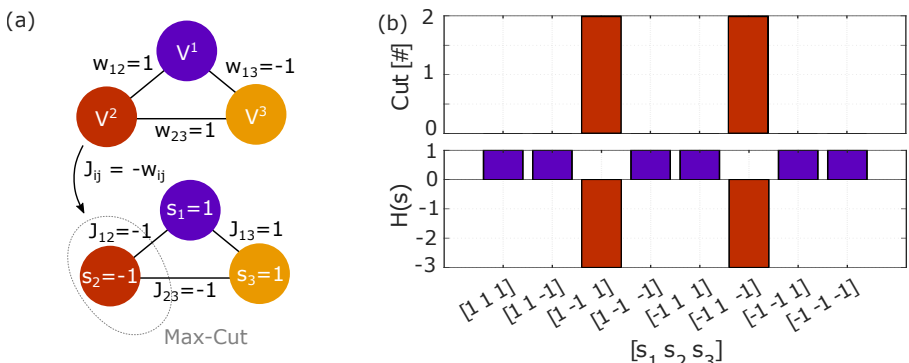


Figure 3.3: (a) Mapping of a Max-Cut problem to the Ising model and (b) correspondence between the ground state and Max-Cut solution.

gration (VLSI) and printed-circuit-board design [167, 168], machine learning [169], data clustering [170], etc. This problem is formulated by a set of nodes  $V$  that are interconnected by edges  $E$  with weights  $w_{ij}$ . The Max-Cut problem consists of ordering the nodes  $V$  into two subsets that maximizes the sum of weights crossing between the two subsets. This problem is easily mapped to the Ising Hamiltonian by assigning the couplings as  $J_{ij} = -1 \cdot w_{ij}$ ; the spins represent the nodes and the spin states  $-1/1$  determine which of the two sets, a particular spin belongs to. This mapping is graphically illustrated in Fig. 3.3 (a), where nodes  $V^i$  are mapped to spins  $s_i$ , and weights  $w_{ij}$  to  $J_{ij}$ . For this simple example, it can easily be seen that the Max-Cut solution consists of  $V^2$  ( $s_2$ ) in one set, while  $V^1$  ( $s_1$ ) and  $V^3$  ( $s_3$ ) are in the other set, as presented in Fig. 3.3 (a) with the dashed gray line. This Max-Cut solution has a cut value of  $w_{12} + w_{23} = 2$ . By plotting all possible configurations of the vertices  $V$  into the two subsets and calculating the cut value, a direct comparison between the energy states of the Ising Hamiltonian and the cut values can be made, as it is presented in Fig. 3.3(b). This shows that when a Max-Cut problem is mapped to the Ising Hamiltonian, the Max-Cut solution coincides with the ground state of the Ising Hamiltonian. Consequently, finding the ground state is equivalent to finding the Max-Cut solution (when the problem is correctly mapped to the architecture). Since the Max-Cut problem is the simplest problem to map to the Ising Hamiltonian, this problem has become the standard for benchmarking different IMs. However, various other problems can be mapped in a similar (although a bit more complicated) way to the Hamiltonian, as it is discussed in detail in [153]. This shows that by developing an architecture that can efficiently solve the Ising model (e.g. IMs), practically relevant problems can be solved using the same architecture, by a correct mapping to the Ising Hamiltonian. The properties of these architectures will be discussed in the following section along with state-of-the-art IMs.

### 3.1.3 State-of-the-Art Ising Machines

In recent years, Ising Machines have gained an immense amount of interest both from academia and industry. Specifically, various technologies including quantum,

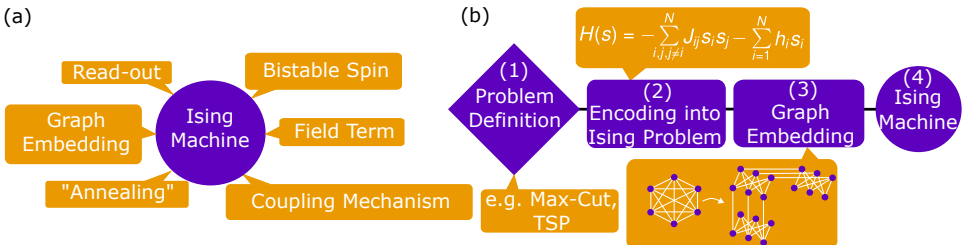


Figure 3.4: (a) Similar characteristics of IMs independent of technology and (b) the process of solving a practical problem utilizing IMs.

optical and electrical approaches have been explored as potential candidates to realize IMs [36]. Most or even all of these technologies have certain common characteristics, which make them suitable to develop IMs. These characteristics are summarized in Fig. 3.4 (a). The fundamental building block of IMs is generally a bistable element that emulates the behaviour of spins in the Ising Hamiltonian and can switch between two stable states. The element emulating the spin also needs to have the possibility of being coupled to other spins to realize the  $J_{ij}$  term and biased to prefer one of the two states, to realize  $h_i$ . For a general purpose IM, both reconfigurable and tunable coupling elements are needed to allow arbitrary problems to be mapped to IMs. To solve a particular problem on an IM, the process generally consists of initializing the system in a certain state and then, gradually change a control parameter such that the IM searches for the ground state of the Hamiltonian. In a very broad sense, this will be referred to as "annealing". It is worth mentioning that in the context that annealing is used here, it does not necessarily refer to a gradual change in temperature (as it is commonly associated with the word annealing). Instead, annealing is used to describe the quantity or the parameter that is changed over time to search for the ground state and return a solution. How the IM searches for the ground state is arguably the most important difference between IMs based on different technologies, and largely determines the performance and quality of a solution for a particular implementation. Consequently, various IMs have been explored in recent years, as it is discussed in detail below. In some IM architectures (to date mostly quantum annealers), the underlying graph of the hardware spins is not all-to-all connected, but only locally connected to nearest neighbours in a systematic way. This introduces an additional step, graph embedding, which is mapping the graph defining the problem to the graph of the hardware. This technique will be discussed in more detail in relation to **[Paper IV]**. After the annealing has taken place, a read-out of the spin states is necessary to extract the solution. In Fig. 3.4 (b), the steps needed to solve a particular problem using an IM are summarized as follows: (1) the problem definition which defines what type a problem is supposed be solved (e.g. Max-Cut or TSP), (2) mapping or encoding the problem using the Ising Hamiltonian as it was previously demonstrated, (3) in some cases, graph embedding is needed to map the Ising Hamiltonian to the underlying hardware and (4) solving the problem by using annealing on the IM. It is worth highlighting that generally, finding the solution to the Ising model using an IM is a statistical process (i.e. it is a heuristic approach). Consequently, a particular problem is solved by performing annealing multiple times, and picking the best solution. The discussion presented so far in this chapter is mostly general and independent of the underlying hardware that emulates the Hamiltonian. Now, the discussion will be shifted towards different technologies and their advantages/disadvantages for implementing IMs.

Quantum annealers [171,172] are probably the most widely known IMs. These architectures are among the first efforts to realize quantum computers for real world practical problems. It is important to note that quantum annealers are

different than the more commonly known quantum "gate" computers since they are specifically designed to solve the Ising model, while quantum "gate" computers are designed using qubit gates, similar to digital gates [173]. Quantum annealers are commonly based on superconducting qubits [172, 174], which emulate the spin in the Ising Hamiltonian and the coupling is realized using Josephson-junctions couplers [175]. The annealing is performed by initializing the system in the known ground state of a Hamiltonian  $H_0$  and slowly reweighting the Hamiltonian of the system to the problem Hamiltonian  $H_P$ , by ramping a control parameter  $\lambda(t)$  from zero to one [36, 172]:

$$H(t) = (1 - \lambda(t))H_0 + \lambda(t)H_P \quad (3.3)$$

This process introduces quantum fluctuations in the qubits and according to the quantum adiabatic theorem, the system remains in the ground state of the instantaneous Hamiltonian  $H(t)$  [172, 176]. Consequently, at the end of the annealing period  $t$ , when  $\lambda(t) = 1$ , the ground state of the problem/Ising Hamiltonian  $H_p$  is found. This is a relatively simplistic description of the actual operation principle of quantum annealers and for a more detailed description, the reader is referred to literature [172, 173, 176]. Since the operation of quantum annealers is based on quantum fluctuations and tunneling, a quantum speed-up can be achieved in theory, compared to classical approaches. However, this potential quantum speedup has not been yet demonstrated and is still debated [173]. Nonetheless, quantum annealers are currently commercially available by D-Wave Systems. The most recent D-wave architecture "Advantage" includes more than 5000 qubits and can work with up to half a million variables when its combined with their software [177]. Consequently, D-Wave's architecture is approaching sizes needed to tackle practically relevant problems. However, quantum annealers come with various challenges. Since they are based on superconducting qubits, they need to be cooled to cryogenic temperatures ( $mK$  range) [172] to function properly and consume large amount of power (in the kW range). Additionally, quantum annealers are generally stored in large room sized chambers. Consequently, with the current state of quantum annealers there is little hope for miniaturization.

Optical IMs, generally referred to as coherent Ising machines (CIMs), are an alternative approach which has been extensively studied in literature [178–181]. This approach is based on degenerate optical parametric oscillators (DOPOs), which are driven optical oscillators. In this approach, the spins  $s_i$  in the Hamiltonian are encoded in the phase of light. In CIMs, the phase of the optical oscillations is forced to settle to 0 or  $\pi$  relative to a pump light driving the DOPO. These two phase states are then mapped to the spin states  $s_i = 1/-1$  in the Ising Hamiltonian (3.1). Consequently, each DOPO is used to represent a single spin in the Ising model. The operating principles of CIMs can be understood by highlighting that the coupling introduces a loss term proportional to  $J_{ij}$ . This additional loss term affects the gain required to get the DOPOs to oscillate, i.e. the threshold of oscillations. Based on this, it can be concluded that the lowest threshold of oscillations in the DOPO network is when the terms corresponding

to the Hamiltonian are minimized [36]. Consequently, a solution to the Ising model is found by ramping the gain term from below to above the threshold, and analysing which DOPOs settle to  $0/\pi$ . Ideally, the first phase state of the DOPOs as the gain passes the threshold should guarantee the ground state solution of the Ising Hamiltonian. However, this is generally not the case, since noise along with other nonidealities such as amplitude heterogeneity limit the solution quality [180]. In recent years, large CIMs with tens of thousands of spin variables [181] using time-multiplexing as a method to represent a large number of spins, have been demonstrated. However, CIMs generally require long optical cables ( $20\text{ km}$  in [181]) and large optical setups. However, this is a promising approach.

Lately, there has been a surge in more "classical" approaches to implement IMs able to counteract the challenges that quantum annealers and optical IMs bring. These approaches include more conventional technologies, such as digital and/or analog CMOS circuits. The digital implementations proposed in literature are commonly inspired by algorithmic approaches (such as parallel tempering), which can take advantage of highly parallel digital application specific ICs (ASICs) or field-programmable gate arrays (FPGAs). For example in [182, 183], a MC type approach using the Metropolis algorithm is implemented on an ASIC. From a simplistic view, the Metropolis algorithm is based on starting from an initial state, randomly flipping the state of spins and checking if this reduces the overall energy of the system. Consequently, Metropolis algorithm dynamically guides the Ising model towards the ground state. Similar implementations based on slightly different hardware architectures or slightly modified algorithms are presented in [184–187]. However, the applied algorithms scale inefficiently with increased connectivity between spins and therefore, these implementations are mostly limited to sparsely connected Ising Hamiltonians. Nevertheless, recent works try to address these challenges [188]. Alternatively, a completely new algorithm called Simulated Bifurcation (SB) has recently been proposed and implemented on FPGAs [189]. This algorithm is inspired by quantum mechanical equations describing the operating behaviour of a quantum annealer based on Josephson parametric oscillators. In [190], Goto et. al. simplify the quantum mechanical dynamics to a remarkably simple system of classical DEs. By solving this system of equations, a solution to the Ising Hamiltonian can be found. The advantage of this algorithm is that it can be highly parallelized. Finally, the potential of realizing IMs using Network-on-Chip has also been recently explored [191].

Similarly, analog CMOS IMs have also been explored in recent years. Analog oscillator-based IMs are among the first explorations of this approach. In [21], Wang et. al. show that the phase dynamics of coupled oscillators under SHIL has a global Lyapunov function equivalent to the Ising Hamiltonian. Consequently, the oscillator network naturally tends to minimize the Lyapunov function/Ising Hamiltonian. In this implementation, the SHIL binarizes the phases to  $0$  or  $\pi$  (which represent the spin states  $s_i = 1/-1$ ), similar to what pump light is doing in CIMs. Each oscillator represents a single spin in the Hamiltonian and the

coupling is realized by resistive or capacitive coupling between the oscillators. The ground state is then found by initializing the system in a random state and gradually increasing the SHIL strength to force the network to a binarized state. This approach has been extensively studied in recent years [192], using various types of oscillators including LC [193,194], ring [195] and Schmitt trigger [196,197] oscillators. While this approach is promising, since it can be implemented using readily available CMOS oscillators, more work is needed to be able to benchmark it against other implementations on large problems. However, in [21] the DEs describing the phase dynamics of a network of coupled Kuramoto oscillators were simulated (similarly to how the SB algorithm is used). The simulation of the DEs outperformed algorithms, such as SA and scatter-search, on finding the ground state of the Hamiltonian, demonstrating that oscillator-based IMs have the potential to outperform conventional approaches. Finally, IMs based on other analog implementations [198,199] and emerging technologies such as memristors [200, 201], MTJs [202, 203] and phase transition oscillators [204, 205] have been also explored.

### 3.1.4 Coupled Kuramoto Oscillators

The operation principles of oscillator-based IMs proposed in [**Paper III**] and [**Paper IV**] is best understood through the Kuramoto model. This section and the following sections are dedicated to introducing the fundamentals of the Kuramoto model. This model was originally developed by Kuramoto in 1975 [206] and it is extensively used to model phase coupled oscillators. In its simplest form, the Kuramoto model can be written as [206]:

$$\frac{d\phi_i}{dt} = \omega_i + K \sum_{j=1, j \neq i}^N \sin(\phi_j - \phi_i) \quad (3.4)$$

describing the phase dynamics of a network of coupled oscillators with operating frequencies  $\omega_i$ .  $\phi_i$  is the phase of oscillator  $i$ ,  $i = 1, 2, 3, \dots, N$ , and  $K$  is the coupling strength between oscillators. This simple model has been applied to study various types of weakly coupled oscillator networks and describes their synchronization properties [207].

One of the most important behaviours that this model describes is the synchronization of oscillators, in phase and frequency. To demonstrate this behaviour, consider the simplest possible example, consisting of two oscillators with operating frequencies  $\omega_1$  and  $\omega_2$ . In this case, (3.4) can be written as:

$$\frac{d\phi_1}{dt} = \omega_1 + K \sin(\phi_2 - \phi_1) \quad (3.5a)$$

$$\frac{d\phi_2}{dt} = \omega_2 + K \sin(\phi_1 - \phi_2) \quad (3.5b)$$

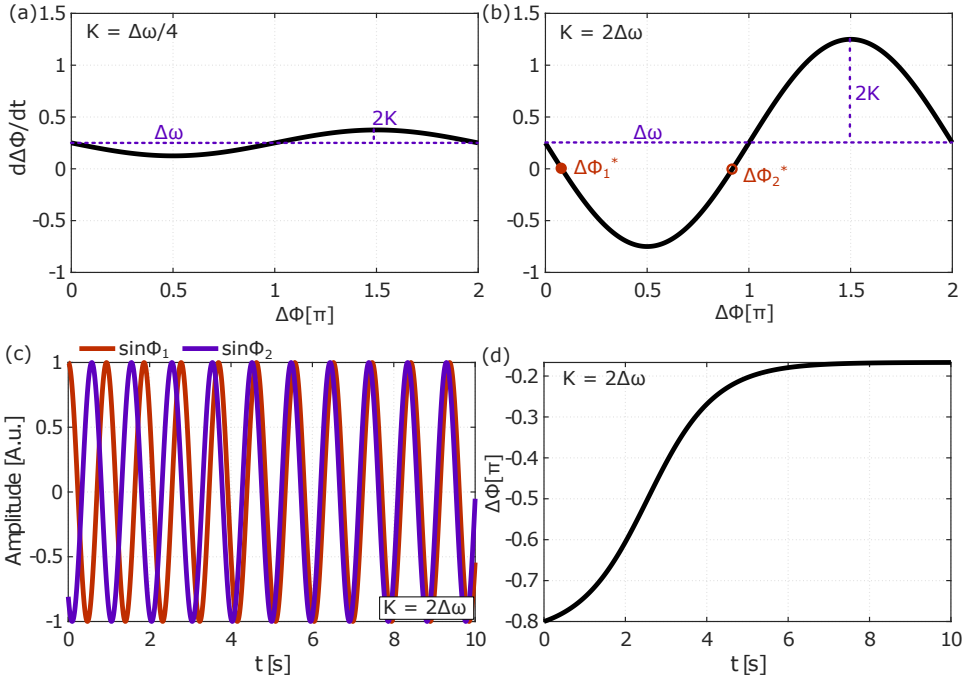


Figure 3.5: Graphical illustration of (3.7) for (a)  $K = \Delta\omega/4$  and (b)  $K = 2\Delta\omega$ , and numerical simulations of DEs for two FM coupled oscillators using (c) (3.5) and (d) (3.7).

By taking the difference of (3.5a) and (3.5b), the phase difference  $\Delta\phi = \phi_1 - \phi_2$  as a function of time can be written as:

$$\frac{d(\phi_1 - \phi_2)}{dt} = (\omega_1 - \omega_2) - 2K \sin(\phi_1 - \phi_2) \quad (3.6)$$

which can be further rewritten as:

$$\frac{d\Delta\phi}{dt} = \Delta\omega - 2K \sin(\Delta\phi) \quad (3.7)$$

where  $\Delta\omega = \omega_1 - \omega_2$ . The fixed points  $\Delta\phi^*$  of this DE can be found by setting  $d\Delta\phi/dt = 0$ , so (3.7) can be written as:

$$\frac{\Delta\omega}{2K} = \sin(\Delta\phi^*) \quad (3.8)$$

A real solution to (3.8) exists only if:

$$\left| \frac{\Delta\omega}{2K} \right| \leq 1 \quad (3.9)$$

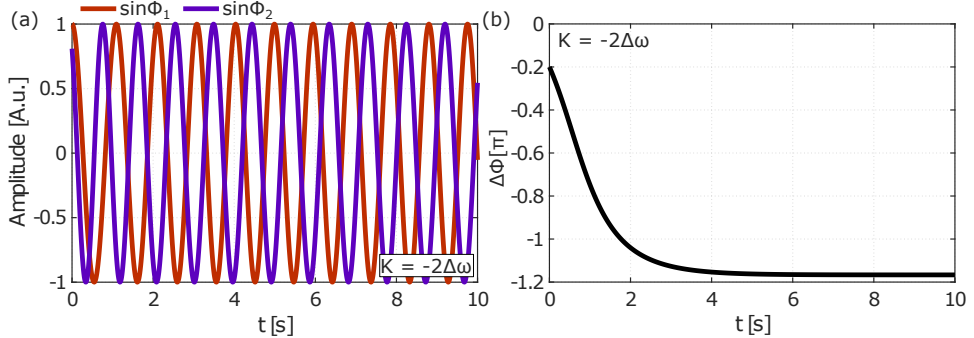


Figure 3.6: Numerical simulations of two AFM coupled oscillators using DEs (a) (3.5) and (b) (3.7).

Consequently, a steady phase difference (fixed point)  $\Delta\phi^*$  is achieved only if  $K \geq \Delta\omega/2$ . This steady phase difference corresponds to a synchronization in frequency with a finite phase difference  $\Delta\phi^*$ . This is further demonstrated in Fig. 3.5(a) and (b) where (3.7) is plotted for two different values of  $K$ . For  $K < \Delta\omega/2$ ,  $d\Delta\phi/dt$  is never equal to zero, indicating that no real solution exists, but for  $K > \Delta\omega/2$ , there are two solutions. As it can also be seen from Fig. 3.5, for the special case when  $\Delta\omega = 0$  (or  $K \gg \Delta\omega/2$ ), (3.8) has two solutions corresponding to  $\Delta\phi_1^* = 0$  and  $\Delta\phi_2^* = \pi$ . By analysing the derivatives of (3.7), it can be easily shown that  $\Delta\phi_1^*$  is stable, while  $\Delta\phi_2^*$  is unstable. The stable fixed point corresponds to the case when both oscillators are synchronized in frequency with zero phase difference. This behaviour is further highlighted by the numerical simulations in Fig. 3.5(c) and (d), where the DEs (3.5) and (3.7) are numerically simulated using a standard explicit Runge-Kutta method, ODE45 from Matlab, which will be used throughout this and the following sections. The numerical simulations of the DEs show that the oscillators synchronize in frequency with  $\Delta\phi \approx -0.2\pi$  for  $K = 2\Delta\omega$ . It is worth highlighting that by flipping the sign of  $K$  in (3.4), exactly the same behaviour is observed in frequency, but the oscillators synchronize out-of-phase with a phase difference of  $\approx \pi$  since the stability of the fixed points is effectively switched (since  $2K\sin(\Delta\phi) = -2K\sin(\Delta\phi - \pi)$ ). Numerical simulations of the DEs describing this case are presented in Fig. 3.6. This case is generally called AFM coupling and it is used in oscillator-based IMs to realize the negative signs of  $J_{ij}$  in the Ising Hamiltonian.

### 3.1.5 Second Harmonic Injection Locking

Injection locking has been studied extensively to realize frequency dividers in phase-locked loops [208]. Moreover, injection locking, as a method to reduce the phase noise in spintronic oscillators, has been also explored [209]. Injection locking occurs when a signal close to the fundamental or a harmonic of the fundamental

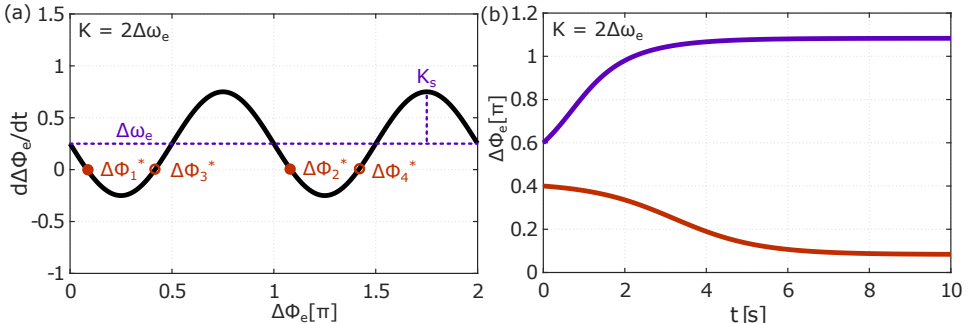


Figure 3.7: (a) Graphical illustration of the fixed points and (b) numerical simulations of the DE (3.11).

is injected into an oscillator. This behaviour can be described in a similar way to the Kuramoto model, but for a single oscillator perturbed by an external signal  $\omega_e$ :

$$\frac{d\phi}{dt} = \omega + K_s \sin(\omega_e t - \phi) \quad (3.10)$$

where  $K_s$  is the coupling strength to the injected signal. Making the substitution  $\Delta\phi_e = \omega_e t - \phi$ , similar to what was done for the coupled Kuramoto oscillators in the previous section, (3.10) becomes:

$$\frac{d\Delta\phi_e}{dt} = \Delta\omega_e - K_s \sin(\Delta\phi_e) \quad (3.11)$$

where  $\Delta\omega_e = \omega_e - \omega$ . This expression exactly matches the previously analysed example for the case of two coupled Kuramoto oscillators, except the coupling strength is now  $K_s$ . This is expected, since intuitively, the external signal serves a similar purpose as  $\phi_2$  in (3.5a) (or equivalently,  $\phi_1$  in (3.5b)), except that it has a fixed phase. Consequently, the analysis results in similar conclusions as for the previously discussed two coupled Kuramoto oscillators.

For oscillator-based IMs, the case when  $\omega_e = 2\omega$  is of interest. This case is generally referred to as SHIL, which occurs when the external perturbation signal is close to twice the fundamental of the oscillator. As it is discussed in detail in [21], it has been experimentally shown that under these conditions, oscillators synchronize in frequency to  $\omega_e/2$  with a phase difference of  $\Delta\phi_e = 0$  or  $\Delta\phi_e = \pi$ . This indicates that the second term on the right hand side of (3.11) is  $\pi$  periodic. Under these conditions, (3.11) becomes:

$$\frac{d\Delta\phi_e}{dt} = \Delta\omega_e - K_s \sin(2\Delta\phi_e) \quad (3.12)$$

where  $\Delta\omega_e = \omega_e/2 - \omega$ . Analysing the fixed points under the assumption  $\Delta\omega_e = 0$ , it can easily be shown that this equation has four fixed points at  $\Delta\phi_{e,1}^* = 0$  and

$\Delta\phi_{e,2}^* = \pi$ , which are stable, and  $\Delta\phi_{e,3}^* = \pi/2$  and  $\Delta\phi_{e,4}^* = 3/2\pi$ , which are unstable. This is further demonstrated graphically in Fig. 3.7 (a) where (3.12) is plotted for  $K = 2\Delta\omega_e$  showing four points where  $d\Delta\phi_e/dt = 0$ . Finally, Fig. 3.7(b) presents numerical simulations of (3.12) for two different initial conditions of the phase difference  $\Delta\phi_e$ , showing that the phase approaches either 0 or  $\pi$ , consistent with the previous analysis. This characteristic is critical for the realization of oscillator-based IMs where SHIL is employed to phase binarize the system, as it will be discussed in the following section.

### 3.1.6 Oscillator-based Ising Machines

Oscillator-based IMs are implemented by combining the two previously discussed techniques, a network of coupled oscillators perturbed at the second harmonic,  $\omega_e = 2\omega$ . Moreover, the coupling,  $K_{i,j}$ , in the network is assumed to be controllable between oscillators  $i$  and  $j$ . In this case, the modified Kuramoto model can be written as:

$$\frac{d\phi_i}{dt} = \omega + K_s \sin(2\omega t - 2\phi_i) + \sum_{j=1, j \neq i}^N K_{ij} \sin(\phi_j - \phi_i) \quad (3.13)$$

where all oscillators operate at the same frequency,  $\omega$ . Similarly to the analysis performed for SHIL, (3.13) can be written in the rotating frame of the external signal  $\omega_e = 2\omega$ , to extract the phase difference  $\Delta\phi_i = \omega t - \phi_i$ :

$$\frac{d\Delta\phi_i}{dt} = -K_s \sin(2\Delta\phi_i) - \sum_{j=1, j \neq i}^N K_{ij} \sin(\Delta\phi_i - \Delta\phi_j) \quad (3.14)$$

As it is proven in [21], (3.14) has a global Lyapunov function that the oscillator network tries to minimize. The global Lyapunov function can be written as [21]:

$$E(\vec{\Delta\phi}) = -K_s \sum_{i=1}^N \cos(2\Delta\phi_i) - \sum_{i,j, i \neq j}^N K_{ij} \cos(\Delta\phi_i - \Delta\phi_j) \quad (3.15)$$

where  $\vec{\Delta\phi} = [\Delta\phi_1, \dots, \Delta\phi_N]^T$ . In the case when all oscillators are perturbed by the SHIL signal  $\cos(2\Delta\phi_i)$  (as is the case in (3.15)), they are forced to settle at discrete phase values of either 0 or  $\pi$ . Under these conditions, the first term on the right hand side of (3.15) becomes a constant ( $-N \cdot K_s$ ) since  $\cos(2\Delta\phi_i) = 1$ . Mapping the phase values of the second term on the right hand side as  $\Delta\phi_i = 0$  to  $s_i = 1$ , and  $\Delta\phi_i = \pi$  to  $s_i = -1$ , (3.15) can be written as [21]:

$$E(\vec{\Delta\phi}) = -N \cdot K_s - \sum_{i,j, i \neq j}^N K_{ij} s_i s_j \quad (3.16)$$

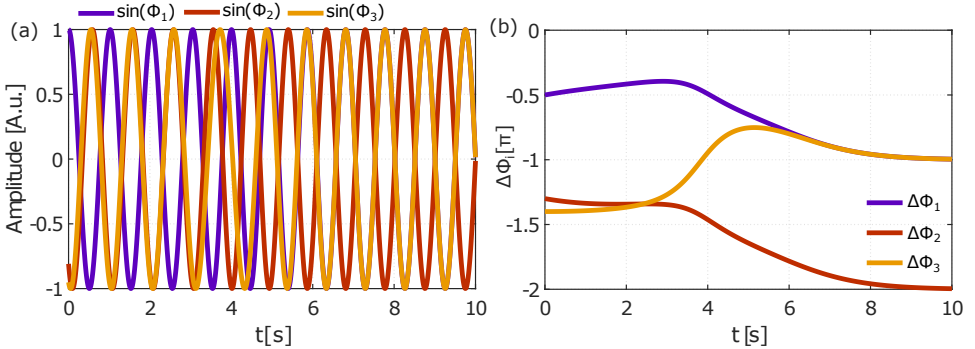


Figure 3.8: Numerical simulation results of a network of three coupled oscillators solving the Max-Cut example in Fig. 3.3(a) in the stationary frame and (b) the rotating frame.

This equation directly corresponds to the Ising Hamiltonian in (3.2) when  $K_{ij} = J_{ij}$  with a constant offset of  $(-N \cdot K_s)$ . As it is highlighted in [21], the constant offset does not change the Hamiltonian but only shifts all the  $E(\vec{\Delta\phi})$  values by the same amount. However, the SHIL plays an important role in the dynamics since it guarantees that the oscillators eventually settle at discrete values of the phase, at  $\Delta\phi_i = 0/\pi$ . This property allows for the substitution of values leading the representation of  $E(\vec{\Delta\phi})$  which is equivalent to the Ising Hamiltonian in (3.16). In the absence of the SHIL term  $\cos(2\Delta\phi_i)$ , there is no guarantee that the oscillators settle at  $\Delta\phi = 0/\pi$  and the equivalence to the Ising Hamiltonian is lost, especially for large networks [21].

To demonstrate the dynamics of the DEs describing the oscillator-based IM, the three node Max-Cut problem in Fig. 3.3(a) is solved using numerical simulations of a network of coupled oscillators. The oscillators are initialized with random initial phases,  $\phi_{i,0}$ , and the SHIL term is linearly ramped up as a function of time to force the oscillators to settle to 0 or  $\pi$ . This ramping of the SHIL signal acts as a sort of "annealing" to search for the ground state of the Ising Hamiltonian, as it has been shown in literature [21]. The coupling  $K_{ij} = K J_{ij}$  in the network is determined by the  $J_{ij}$  in Fig. 3.3 (a), but additionally scaled by a factor  $K$ . Therefore, (3.13) becomes:

$$\frac{d\phi_i}{dt} = \omega + K_s \frac{t}{t_{end}} \sin(2\omega t - 2\phi_i) + K \sum_{j=1, j \neq i}^N J_{ij} \sin(\phi_j - \phi_i) \quad (3.17)$$

where  $\omega = 2\pi \text{ rad/s}$ ,  $K_s = 0.2\pi \text{ rad/s}$ ,  $t_{end}$  is the simulation time (10 seconds for this example) and  $K = K_s$ . The simulation results are presented in Fig. 3.8 both in the stationary frame using (3.17) and in the rotating frame in terms of  $\Delta\phi_i$  (similar to (3.14)). As expected, the network settles to the ground state

of the Ising Hamiltonian or equivalently, to the Max-Cut solution corresponding to  $\phi_1$  and  $\phi_3$  in one set, and  $\phi_2$  in the other set. It is worth highlighting that from a practical point of view, to implement  $J_{i,j} = -1$  (or equivalently, negative coupling  $K_{i,j} < 0$ ), the signal is simply shifted by  $\pi$  before being injected into another oscillator since  $-\sin(\phi_j - \phi_i) = \sin(\phi_j - \phi_i - \pi)$ . This corresponds to the previously discussed AFM coupling.

The previously presented analysis shows that the phase dynamics of a network of coupled oscillators under SHIL as presented in (3.13) naturally tends to minimize the Ising Hamiltonian in (3.2). Consequently, an IM can be readily realized using a network of coupled oscillators. It is worth highlighting that the field term that was present in the original Ising Hamiltonian (3.1) can be introduced in the oscillator-based IM by also applying a signal (which is at the oscillator fundamental), with a phase of 0 or  $\pi$ , to the oscillators. This biases the oscillator to prefer either the phase state  $\Delta\phi = 0$  or  $\Delta\phi = \pi$ . However, for the remainder of the thesis, the biasing term  $h_i$  will be ignored since it is not relevant for the results presented in [Paper III, IV and V]. Specifically, in these papers the Max-Cut problem is used to demonstrate the functionality and for this problem, the field term is irrelevant and fixed to zero.

## 3.2 Spintronic Oscillator-based Ising Machine

Networks of coupled oscillators are a promising approach to realize large scale IMs. However, for this approach to be successful, the oscillators, used to implement the spins in the Hamiltonian, need to have a small footprint and be energy efficient. Moreover, as it is shown in [193], the performance of oscillator-based IMs is expected to improve with increasing operating frequency. Spintronic oscillators exhibit characteristics which are desirable for implementing oscillator-based IMs: 1) spintronic oscillators generally occupy a small area of approximately  $100\text{ nm} \times 100\text{ nm}$  [210], 2) SHNOs/STNOs have the potential to be synchronized in large networks [86, 102] and 3) spintronic oscillators generally operate at  $\text{GHz}$  [210] or even tens of  $\text{GHz}$  frequencies [74]. Inspired by these promising characteristics, the possibility of implementing spintronic oscillator-based IMs was explored in [Paper III]. Spintronic oscillators are generally strongly nonlinear since the operating frequency  $\omega_p(p)$  and both the negative and positive damping rates  $\Gamma_+/\Gamma_-$  are all a function of the power  $p = |c|^2$  [81]. Consequently, spintronic oscillators exhibit qualitatively different characteristics than many of the CMOS oscillators that have been explored for IMs. Consequently, as a first step towards demonstrating spintronic oscillator IMs, we investigated whether spintronic oscillators exhibit the fundamental characteristics needed to realize IMs. Specifically, these include in-phase (FM coupling) and out-of-phase (AFM coupling) synchronization and phase binarization using SHIL. In [Paper III] this is explored using numerical simulations of the universal auto-oscillator model DEs (2.7), extended to include SHIL and coupling to other oscillators operating in a network [81]. Com-

pared to conventional electronic oscillators that can be coupled only by electrical means, spintronic oscillators can be synchronized using different coupling mechanisms, such as dipolar [94, 211], direct exchange [86, 96, 212], spin-wave [213–215] and electrical [95, 102, 216]. The choice of coupling mechanism can have a significant impact on how a spintronic IM would be physically implemented. However, the study performed in [Paper III] is independent of the underlying coupling mechanism since the analysis is focused on exploring whether spintronic oscillators exhibit the previously mentioned characteristics for IMs.

### 3.2.1 Impact of Nonlinearity on the Phase Dynamics of Coupled Spintronic Oscillators

The DEs describing a network of coupled spintronic oscillators under SHIL, studied in [Paper III], can be written in terms of the universal auto-oscillator model as (all parameters are described in detail in [Paper III]) [81, 217]:

$$\begin{aligned}
 \frac{dc_j}{dt} + i\omega_j(p_j)c_j + \Gamma_{+,j}(p_j)c_j - \Gamma_{-,j}(p_j)c_j \\
 = K_e e^{-i\omega_e t} c_j^* + \sum_{j'} \Omega_{j,j'} e^{i\beta_{j,j'}} c_{j'}
 \end{aligned} \tag{3.18}$$

To gain insight into the differences between the ideal oscillator-based IM as in (3.13) and the spintronic oscillator IM, it is convenient to write (3.18) in terms of the power  $p = |c|^2$  and the phase  $\phi = \arg(c)$ . While this will require two coupled DEs, one for  $p$  and one for  $\phi$ , to describe each STNO, it allows for a direct comparison with the Kuramoto model. The DEs for  $p$  and  $\phi$  can be derived from (3.18) as:

$$\begin{aligned}
 \frac{dp_j}{dt} = -2p_j[\Gamma_{+,j}(p_j) - \Gamma_{-,j}(p_j)] + 2K_e p_j \cos(\omega_e t + 2\phi_j) \\
 + 2 \sum_{j,j'} \Omega_{j,j'} \sqrt{p_j p_{j'}} \cos(\phi_j - \phi_{j'} - \beta_{j,j'})
 \end{aligned} \tag{3.19a}$$

$$\begin{aligned}
 \frac{d\phi_j}{dt} = -\omega_j(p_j) - K_e \sin(\omega_e t + 2\phi_j) \\
 + \sum_{j,j'} \Omega_{j,j'} \sqrt{p_{j'}/p_j} \sin(\phi_{j'} - \phi_j + \beta_{j,j'})
 \end{aligned} \tag{3.19b}$$

There is a minor, but important difference when comparing the phase (3.19b) with the phase dynamics of the oscillator-based IM in the Kuramoto framework (3.13). Note that in (3.18)–(3.19) the notations are slightly different compared to (3.13) to keep the equations consistent with [Paper III]. Specifically, the operating frequency  $\omega(p)$  and the coupling strength to other STNOs depend on

the power  $p$  described by (3.19a). To get an intuition for how the dynamics of (3.19b) differ from (3.13), the system can be analyzed assuming a weak coupling both to the SHIL and between oscillators (i.e.  $K_e \rightarrow 0$  and  $\Omega_{j,j'} \rightarrow 0$ ) and that the power deviation is small. Specifically,  $\delta p = p - p_0$  is assumed small, where  $p_0$  represent the power of the free running oscillator and  $p$  the power of the perturbed oscillator, as described by (3.19a). Under these assumptions, (3.19) can be expanded using Taylor series and written in terms of the effective nonlinear auto-oscillator phase,  $\tilde{\phi}_j$ , as it is performed in [81] (although for fundamental injection locking, the procedure here is similar):

$$\begin{aligned} \frac{d\tilde{\phi}_j}{dt} = & -\omega_j(p_{0,j}) - \sqrt{1 + \nu^2} K_e \sin(\omega_e t + 2\tilde{\phi}_j - \tan^{-1}(\nu)) + \\ & \sum_{j,j'} \sqrt{1 + \nu^2} \Omega_{j,j'} \sqrt{p_{0,j'}/p_{0,j}} \sin(\tilde{\phi}_{j'} - \tilde{\phi}_j + \beta_{j,j'} - \tan^{-1}(\nu)) \end{aligned} \quad (3.20)$$

where  $\nu$  is the normalized nonlinear frequency shift coefficient, which characterizes the nonlinearity of the oscillators, and it can be found according to the macrospin approximation [81]. The phase  $\tilde{\phi}_j$  is now only dependent on the free running oscillation power  $p_{0,j}$ . This expression can be further simplified assuming that all oscillators have identical operating frequencies  $\omega(p_0)$  and power  $p_0$ . Moreover, it can be written in the rotating frame  $\Delta\tilde{\phi}_j = \omega(p_0)t + \tilde{\phi}_j - \tan^{-1}(\nu)/2$  assuming  $\omega_e = 2\omega(p_0)$  (similar to how it was done for the Kuramoto model), to arrive at:

$$\begin{aligned} \frac{d\Delta\tilde{\phi}_j}{dt} = & -\sqrt{1 + \nu^2} K_e \sin(2\Delta\tilde{\phi}_j) - \\ & \sum_{j,j'} \sqrt{1 + \nu^2} \Omega_{j,j'} \sin(\Delta\tilde{\phi}_j - \Delta\tilde{\phi}_{j'} - \beta_{j,j'} + \tan^{-1}(\nu)) \end{aligned} \quad (3.21)$$

This form of (3.21) closely resembles the form of the Kuramoto model in (3.14) and the impact of the nonlinearity can be directly observed. Specifically, the nonlinearity increases the coupling strength between oscillators and to the SHIL signal by a factor of  $\sqrt{1 + \nu^2}$ , and introduces a phase shift of  $\tan^{-1}(\nu)$ . For spintronic oscillators, the normalized nonlinear frequency shift coefficient  $|\nu|$  is generally  $> 1$  and consequently, it modifies the phase dynamics of the system. The phase-shift,  $\tan^{-1}(\nu)$ , introduced in the coupling function between oscillators, is of significant importance for implementing IMs. Specifically, this additional phase shift can introduce unwanted behaviour in the phase dynamics. For a strongly nonlinear spintronic oscillator, the phase shift introduced by the nonlinearity approaches  $\pm\pi/2$  since  $\tan^{-1}(\nu) \rightarrow \pm\pi/2$  for  $|\nu| \gg 1$ . Consequently, the fixed points of the SHIL (the first term on the right hand side of (3.21)) are different from the fixed points of the second term, which is a qualitatively different dynamical system than the phase dynamics of the conventional oscillator-based IM, as described by (3.14). As it is discussed in [Paper III], the impact of the phase shift introduced by the nonlinearity can be accounted for, by introducing an

additional phase shift  $\beta_{j,j'}$ , such that the effective (or total) phase shift becomes  $\tilde{\beta}_{j,j'} = \beta_{j,j'} - \tan^{-1}(\nu)$ . By tuning  $\beta_{j,j'}$ , a total phase shift of 0 or  $\pi$  can be achieved, depending if a FM or AFM coupling is desired.

While this analysis is based on the previously mentioned assumptions, it provides some intuition on how the phase dynamic of the spintronic oscillator IM differ from the oscillator-based IM based on the Kuramoto framework. To further verify these conclusions, in [Paper III] numerical simulations of coupled STNOs and STNOs under SHIL are performed using the non-simplified DEs (3.18). The results of these numerical simulations are discussed in the following sections.

### 3.2.2 Numerical Simulation Approach

In this section, the methods used for the numerical simulations presented in [Paper III] are briefly presented. All the numerical simulations are performed using Python with the 'odeint' solver within the 'scipy' package [218]. More specifically, 'odeintw', which is a wrapper of odeint that can also handle complex numbers, was employed. This solver is based on 'lsoda' from Fortran and it is a dynamical solver that automatically detects the stiffness of the problem and switches between a stiff solver and a non-stiff solver, both of which are linear multistep methods [219]. The tolerance of the solver was chosen well below any meaningful changes in the phase  $\phi$  or power  $p$  and was fixed to  $10^{-5}$  for all the numerical simulations. To speed up the numerical simulations, multiprocessor scheduling was employed in combination with Numba [220], which is based on the LLVM compiler library and can accelerate python code such that it approaches speeds of C/Fortran.

To characterize the behaviour of the spintronic oscillator-based IM, various Max-Cut problems were solved in [Paper III]. The Möbius ladder graphs of different sizes (used in [Paper III]) were generated by a simple python script since these graphs follow simple rules and are easily generated for arbitrary size. The cubic random graph and other graphs, presented below, were generated using "Rudy", a commonly used graph generator developed by G. Rinaldi. Finally, to determine the Max-Cut solution of the generated graphs, a commercially available optimization tool LocalSolver was employed [221].

### 3.2.3 Simulation Results

As a first step towards demonstrating that spintronic oscillators exhibit the desired characteristics to realize IMs, numerical simulations of the DEs describing a single STNO perturbed by a SHIL signal were performed in [Paper III]. The main results of these numerical simulations are presented in Fig. 1 (b) in [Paper III], where the frequency of the STNO as a function of the SHIL frequency  $\omega_e/2$  (or equivalently  $f_e/2$ ) is presented. This graph was plotted by extracting the phase  $\phi = \arg(c)$  from numerical simulations of the universal auto-oscillator model DEs and taking the FFT to analyse the frequency content of the per-

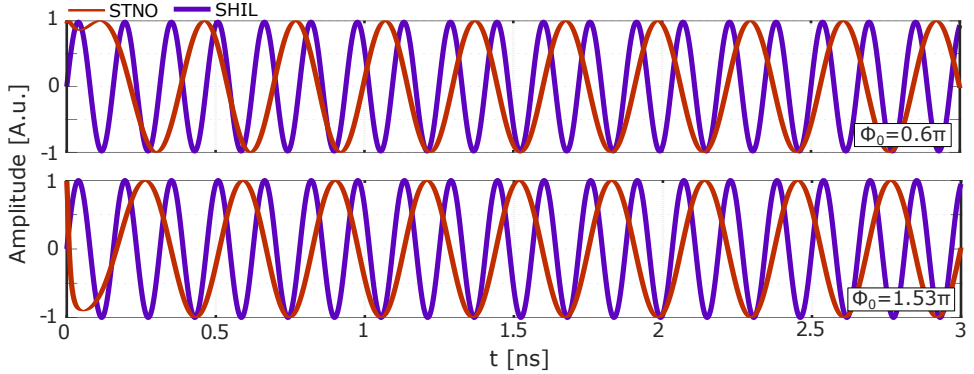


Figure 3.9: Transient of a STNO under SHIL for two different initial conditions.

turbed STNO. The FFT was performed with a resolution bandwidth (RBW) of  $f_{RBW} = 10 \text{ MHz}$ . The results in Fig. 1 (b) in [Paper III] show that the STNO synchronizes in frequency to  $\omega_e/2$  over a locking bandwidth of approximately  $200 \text{ MHz}$  (from  $3.1 \text{ GHz}$  to  $3.3 \text{ GHz}$ ) when  $K_e = 50 \text{ MHz}$ . Specifically, the maximum frequency difference  $\Delta\omega = \omega_e/2 - \omega(p)$  is  $\approx 100 \text{ MHz}$ , while still synchronizing in frequency. For the MTJ STNO modeled in [Paper III]  $\nu$  is  $\approx -2.64$  which explains why the locking bandwidth  $\Delta\omega$  is much larger than  $K_e$ . Specifically,  $\nu$  increases the coupling strength to the SHIL by a factor  $\sqrt{1 + \nu^2}$  as it was shown in Section 3.2.1, leading to  $\sqrt{1 + \nu^2} K_e \approx 140 \text{ MHz}$ . Moreover, the simulated STNO can synchronize to the SHIL signal at two distinct phase differences as presented in Fig. 3.9. As it was discussed in detail in Section 3.1.5, this phenomena is called phase binarization and for Kuramoto oscillators these two steady states correspond to a phase difference of 0 and  $\pi$ . However, in spintronic oscillators, the qualitatively different nonlinearity introduces a phase-shift between the SHIL signal and the STNO (as it was discussed in relation to 3.19b), which approaches  $\pi/2$ , this behaviour is confirmed with the numerical simulations presented in Fig. 3.9.

Subsequently, the synchronization dynamics of two coupled spintronic oscillators were analysed in [Paper III]. The impact of the coupling strength  $\Omega_{j,j'}$  and the coupling phase  $\beta_{j,j'}$  for different values was explored. As it can be observed from these simulation results, the phase coupling significantly modifies the synchronization properties of STNOs. Specifically, the oscillators can even synchronize at frequencies which are not a combination of their independent free-running frequencies. However, this undesired property can be mitigated by introducing an additional phase shift of  $\beta_{j,j'} \approx -\pi/2(-1.5\pi)$ , as it is shown in Fig. 1 (d)-(g) and (f)-(h), in [Paper III]. Consequently, by introducing this additional phase shift, spintronic oscillators exhibit all the desired characteristics needed to implement IMs.

To further verify that spintronic oscillators can be employed to realize oscillator-

based IMs, numerical simulations of the DEs (3.18) solving various Max-Cut problems were performed in [Paper III]. As a first step, Möbius ladder graphs were employed to demonstrate that a system of coupled spintronic oscillators under SHIL do indeed operate as an IM. Next, it was verified that SHIL can be used to improve the performance of the proposed IM, similar to conventional oscillator-based IM [21]. Finally, the probability of finding the Max-Cut solution for various randomly generated cubic graphs was explored. Additionally, in Fig. 3.10, simulation results demonstrating the impact of varying the simulation time  $t_{end}$  and the SHIL strength  $K_e$  for different graphs is presented. It is worth highlighting that these numerical simulations are performed for a linear annealing schedule where  $K_e$  is linearly ramped as a function of time, i.e.  $K_e = K_{e,end} \cdot t/t_{end}$ . While the square-wave annealing employed in [Paper III] has improved the performance of the IM significantly, the used linear schedule allows for a simpler comparison between different simulation times and graph sizes. These results provide some intuition on how the performance of the spintronic oscillator-based IM depends on different parameters and how an improper annealing schedule can degrade the performance of the IM.

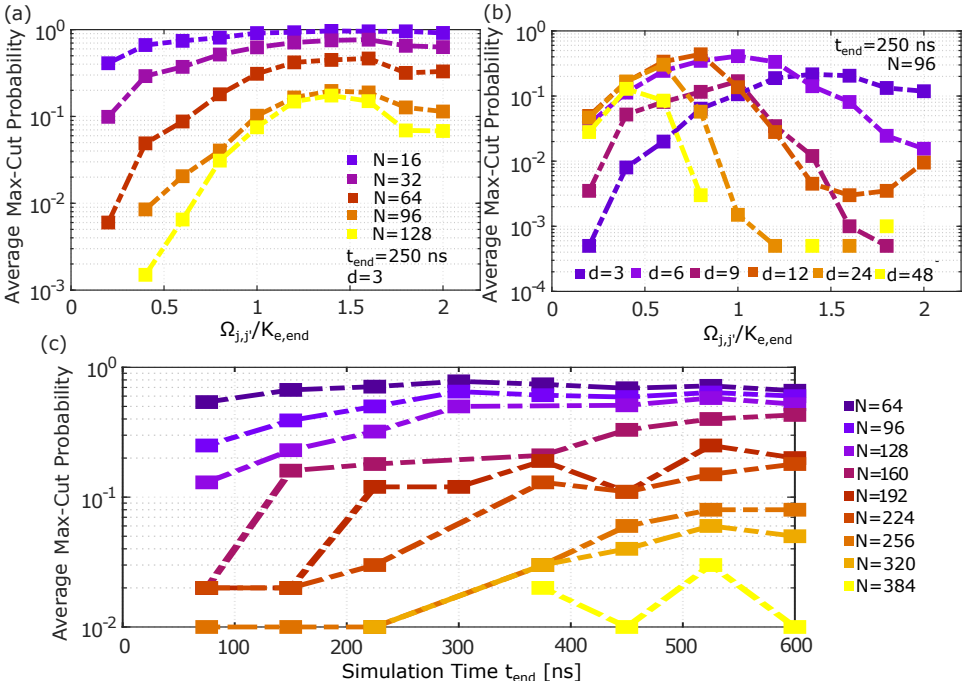


Figure 3.10: Max-Cut probability (normalized to one) as a function of the coupling strength  $\Omega_{j,j'}$  for (a) different problem sizes and (b) different graph densities. (c) Max-Cut probability for different sizes of Möbius Ladder graphs as a function of simulation time  $t_{end}$ .

In Figure 3.10(a), the average probability of finding the Max-Cut solution for 20 randomly generated cubic graphs of sizes  $N = [16, 32, 64, 96, 128]$  is presented. The mean Max-Cut probability is presented as a function of  $\Omega_{j,j'}/K_{e,end}$ , where  $\Omega_{j,j'}$  is swept and  $K_{e,end}$  is fixed to 25 MHz. There are some interesting conclusions that can be made based on these numerical simulations. Firstly, for a fixed simulation time  $t_{end} = 200$  ns, the probability of finding the Max-Cut solution for smaller graphs is relatively unaffected by the ratio of  $\Omega_{j,j'}/K_{e,end}$ . The effect of a proper choice of the ratio  $\Omega_{j,j'}/K_{e,end}$  becomes more apparent as the graph size increases, showing a constant peak probability around  $\Omega_{j,j'}/K_{e,end} \approx 1.5$ . Extrapolating this behaviour to larger graphs, it is expected that the peak becomes more pronounced for larger graphs, which consequently makes the choice of a proper  $\Omega_{j,j'}/K_{e,end}$  ratio more important. Similarly, by increasing (reducing) the simulation time, the choice of  $\Omega_{j,j'}/K_{e,end}$  becomes less (more) important for the same graph size. Based on these characteristics, it can be speculated that the SHIL term acts as an "accelerator", accelerating the phase dynamics and consequently, increasing the probability of finding the optimal solution during a fixed annealing/simulation time. However, as it can also be seen from Fig. 3.10, the performance deteriorates significantly if  $\Omega_{j,j'}/K_{e,end}$  is too small. Consequently, the correct choice of  $\Omega_{j,j'}/K_{e,end}$  is imperative. To further explore the impact of  $\Omega_{j,j'}/K_{e,end}$ , the Max-Cut probability for random graphs of size  $N = 96$ , but now varying the degree of the graph,  $d$  is presented in Fig. 3.10(b). The degree  $d$  determines the number of edges (couplings) connected to each node (oscillator), e.g. cubic graphs and Möbius ladder graphs both have  $d = 3$ . As it is shown in 3.10(b), the peak Max-Cut probability shifts to lower values of  $\Omega_{j,j'}/K_{e,end}$  with higher densities. Moreover, the peak becomes more pronounced with increasing densities, making the choice of a correct  $\Omega_{j,j'}/K_{e,end}$  more important. Consequently, the optimal  $\Omega_{j,j'}/K_{e,end}$  is strongly dependent on the density of the graph to be solved. Finally, in Fig. 3.10 (c), the probability of finding the Max-Cut solution as a function of the simulation/annealing time  $t_{end}$  for different sizes of Möbius ladder graphs is presented. As expected, the probability increases with the annealing time, which is a fundamental characteristic of many IMs and also resembles the behaviour observed in algorithmic approaches such as SA. Based on these results, it can be concluded that the optimal annealing schedule (at least for the linear ramp used here) is highly dependent on the problem to be solved and an incorrect choice can significantly deteriorate the performance of the IM. While the IM proposed here is based on spintronic oscillators, it is expected that a similar behaviour will be observed for conventional oscillator-based IMs. The optimal choice of annealing schedule for oscillator-based IMs is relatively unexplored in literature, however as it was shown here, it is a very important research direction for optimizing the operation of oscillator-based IMs.

### 3.2.4 Limitations and Future Work

In this section, limitations and opportunities to implement oscillator-based IMs using spintronic oscillators are discussed, complementing [Paper III]. It has been demonstrated that spintronic oscillators exhibit all the required fundamental characteristics needed to develop an oscillator-based IMs. Moreover, it was shown that networks of coupled spintronic oscillators can be employed to solve various Max-Cut problems and that the choice of the annealing schedule highly impacts the performance of oscillator-based IMs.

However, as it was discussed in detail in this chapter, the nonlinearity introduces a phase delay in the coupling which approaches  $\pi/2$ . Consequently, to achieve the same phase dynamics as in the ideal Kuramoto oscillator-based IM an additional phase delay needs to be introduced to cancel this term. The most straightforward way to achieve this experimentally, is by electrically coupling together spintronic oscillators and introducing a phase delay of  $\beta_{j,j'}$  between them, similar to what was done in [95]. Similarly, other coupling mechanisms, such as spin-wave or direct exchange, could also potentially address this issue with less overhead by properly engineering the physical interface between spintronic oscillators. However, to the author knowledge, this has not been yet explored for tuning the phase or strength of the coupling between oscillators. Therefore, more research is needed to experimentally realize large scale oscillator-based IMs using spintronic oscillators. However, spintronic oscillators are being continuously developed and their functionality extended/improved through e.g. gated control [115, 222] and even new phenomena, such as memristive properties [116], are incorporated into their operation. Consequently, spintronic oscillator-based IMs could be a good candidate for realizing future IMs. In the last year, extensive research on spintronic oscillator-based IMs has been performed, theoretically, using electrically coupled three-terminal SHNOs [107], and experimentally, using four coupled nanoconstriction SHNOs [108].

## 3.3 Reconfigurable Ring Oscillator-based Ising Machine

One of the major challenges associated with developing large scale IMs is the number of interconnects/coupling elements that are required. As it can be seen from the Ising Hamiltonian, the Ising problem consists of  $N$  spins, where each spin is coupled to at most  $(N - 1)$  other spins. Consequently, for an IM of size  $N$ , at least  $N(N - 1)/2$  coupling elements are needed such that the IM can solve arbitrary problems of size  $N$ . Moreover, if the coupling elements are unidirectional (as it is often the case), this number increases to  $N(N - 1)$ . To get some perspective on this scaling, an IM with  $N = 1000$  spins will require  $\approx 50000$  coupling elements. For IMs based on CMOS technology, these coupling elements are generally implemented with resistors or capacitors physically connecting the circuits realizing the spins in the Ising Hamiltonian. It is evident that this is a major design challenge, even for moderately large IMs consisting of a couple

of thousand spins. Moreover, for a general purpose IM, the coupling between spins needs to be reconfigurable, i.e. can be turned on/off, and have a tunable (multibit) magnitude with the possibility of realizing positive and negative values. These design constraints present a major design challenge for realizing practically relevant large scale IMs.

The possibility of realizing a highly tunable and reconfigurable coupling scheme between phase coupled oscillators has been explored in literature [223]. This idea was originally proposed as a potential implementation of oscillatory neurocomputers in [223] and it was later experimentally demonstrated in [40]. The idea is based on a network of weakly coupled oscillators operating at different frequencies. By modulating the coupling strength with a pseudo-periodic function, an arbitrary coupling between oscillators in the network can be achieved even though all oscillators are connected to a single common node. The coupling in the network is purely determined by the harmonic content of the modulation signal. Inspired by this idea, in [**Paper IV**], the possibility of using the same approach to realize a highly reconfigurable oscillator-based IM was explored. As a first step, the proposed approach was analyzed using numerical simulations of the Kuramoto model. Subsequently, the limitations of the proposed approach were identified and a potential solution was proposed. Finally, a proof of concept was demonstrated through circuit simulations of a network of coupled ring oscillators.

In this section, additional analysis of the proposed architecture in [**Paper IV**] is presented and the limitations of this approach are discussed. Additionally, the potential of employing graph embedding to realize arbitrary graphs in the proposed architecture is briefly discussed.

### 3.3.1 Proposed Architecture

As it is discussed in detail in [**Paper IV**], the proposed architecture is based on a network of coupled oscillators operating at distinct operating frequencies  $\omega_i$ , where each oscillator is perturbed by a SHIL signal  $2\omega_i$ . Moreover, the coupling strength  $K$  is chosen much smaller than the minimum difference between operating frequencies  $\omega_{diff,min}$  in the system and consequently, oscillators do not synchronize in frequency. On the contrary, all oscillator-based IMs discussed until now have in common that the oscillators in the network are assumed to operate at the same frequency (and consequently are synchronized in frequency).

As it is detailed in [**Paper III**], all oscillators are assumed to be connected to a single common node, and consequently, there is a global coupling  $K$  among all oscillators in the network. Moreover, it is assumed that the global coupling can be modulated with a quasi-periodic function  $a(t)$ . The DEs describing the phase dynamics of this system can be written in a rotating frame relative to the external signal (note that this is the same procedure as it was performed when extracting  $\Delta\phi$  for conventional oscillator-based IMs). Here, the phase in the rotating frame is written in terms of  $\theta$ , instead of  $\Delta\phi$  as it was previously done (although they

are equivalent), to keep the notations consistent with [Paper IV]:

$$\frac{d\theta_i}{dt} = -K_{s,i} \sin(2\theta_i) - K a(t) \sum_{j=1, j \neq i}^N \sin((\omega_i - \omega_j)t + \theta_i - \theta_j) \quad (3.22)$$

where  $a(t)$  is the modulation signal which modulates the coupling  $K$  at frequencies equal to the difference in operating frequency between oscillator  $i$  and  $j$ . Specifically,  $a(t)$  can be written as:

$$a(t) = \sum_{i=1}^N \sum_{j=1}^N c_{i,j} \cos((\omega_j - \omega_i)t) \quad (3.23)$$

As it is shown in [Paper IV], the average phase dynamics of this system can be simplified to:

$$\frac{d\theta_i}{dt} \approx -K_{s,i} \sin(2\theta_i) - K \sum_{j=1}^N \frac{c_{i,j} + c_{j,i}}{2} \sin(\theta_i - \theta_j) \quad (3.24)$$

when all frequency differences  $(\omega_j - \omega_i)$  are assumed to be different (i.e. the operating frequencies form a Golomb ruler). The simplified averaged expression for the phase dynamics matches exactly the phase dynamics of a conventional oscillator-based IM (when  $c_{i,j} = c_{j,i}$ ), as presented in (3.14). This simplification or averaging of the phase dynamics can be performed by separating the time scales of the fast and slow phase dynamics, as it is detailed in [Paper IV]. The validity of this assumption can be easily verified by comparing the numerical simulations of (3.22) and (3.24), as presented in Fig. 3.11. These numerical simulations are performed using ODE45 in Matlab for two coupled oscillators with  $\omega_1 = 2\pi \text{ rad/s}$  and  $\omega_2 = 1.3 \cdot 2\pi \text{ rad/s}$ ,  $K = (\omega_2 - \omega_1)/10$  and  $c_{1,2} = c_{2,1} = -1$  corresponding to

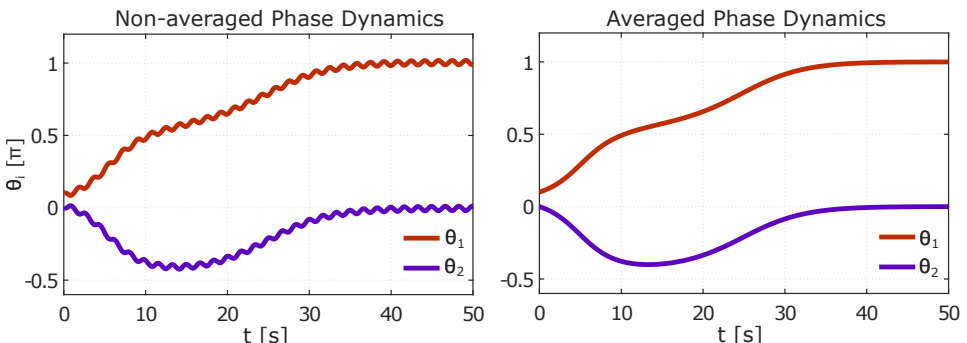


Figure 3.11: Comparison of the non-averaged phase dynamics using (3.22) - (3.23) and the averaged phase dynamics using (3.24).

AFM coupling. Additionally,  $K_s$  is linearly ramped from 0 to  $(\omega_2 - \omega_1)/10$  as a function of the simulation time. As it can be seen from these simulation results, the averaging only removes small ripples that happen on the fast time scale and do not impact the overall phase dynamics on the slow time scale. However, it is worth highlighting that all numerical simulations presented in [Paper IV] are performed using the non-averaged equations.

### 3.3.2 Comparison with Conventional Oscillator-based IMs

The distinguishing feature of the proposed approach from the conventional oscillator-based IM is that coupling between oscillators is determined by the amplitudes of the modulation signals  $c_{i,j}$ , but not the physical connectivity between oscillators. This difference and its impact on the physical implementation of oscillator-based IMs is depicted in Fig. 2 in [Paper IV], but also in Fig. 3.12. Specifically, instead of  $N(N - 1)$  physical interconnects, only  $N$  connections to a common medium (i.e. an element that implements the global coupling among oscillators and it can be modulated as a function of time) are needed. Consequently, the common node (medium) serves as a bus where the coupling among oscillators can be individually tuned by changing the amplitudes of the modulation signals through  $c_{i,j}$ . This is presented in Fig. 3.12, where it is shown how an example graph of size  $N = 4$  is mapped to both conventional oscillator-based IMs (with resistive coupling) and the proposed implementation. The disadvantage of this method is that the coupling in the network needs to be kept much smaller than  $\omega_{diff,min}$ , which leads to longer convergence, as it is discussed in detail in [Paper IV]. If this condition is not met, the phase dynamics of the system are not dominated by (3.24) anymore and the desired functionality is lost. The impact

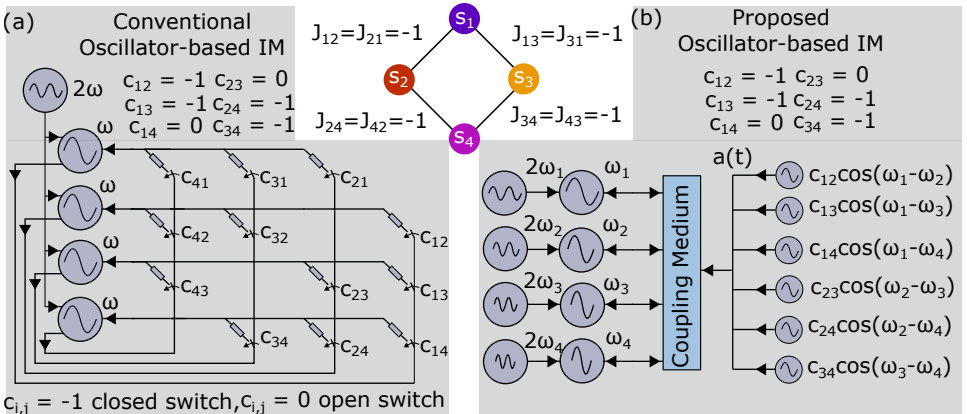


Figure 3.12: Comparison of conventional oscillator-based IMs and the proposed implementation.

of this condition can be clearly observed by comparing the phase dynamics of a conventional oscillator-based IM as in (3.14) to the phase dynamics of (3.22), as presented in Fig. 3.13. These numerical simulations were performed using a similar setup as the numerical simulations in the manuscript and were performed for six all-to-all AFM ( $c_{i,j} = -1$ ) coupled oscillators using ODE45 from Matlab. Specifically, the operating frequency of the oscillators are distributed according to a Golomb ruler between  $5\text{ MHz}$  and  $10\text{ MHz}$ , and  $K_s = 0.5K \cdot t/t_{end}$  where  $t_{end} = 200\text{ }\mu\text{s}$  is the simulation time. As it can be observed from Figs. 3.13 (a) and (b), the dynamics of the proposed implementation based on quasi-periodically modulated coupling strength match almost exactly the ones of the conventional oscillator-based IMs, if  $K$  is chosen as  $0.05\omega_{diff,min}$ , where  $2\pi\omega_{diff,min} \approx 0.3\text{ MHz}$ . Moreover, both IMs settle to an optimal solution of this simple 6 node graph, which corresponds to three oscillators in one set and three oscillators in the other set. By increasing  $K$  to  $0.5\omega_{diff,min}$ , discrepancies in the phase dynamics of the two implementations start to appear. However, both implementations still settle to a solution corresponding to the Max-Cut solution (although the two solutions are different, they are both equally valid). Finally, by increasing  $K$  to  $2\omega_{diff,min}$ , the phase dynamics of the proposed implementation are completely destroyed and the proposed implementation doesn't function anymore as an IM. The reason for this is that since  $K$  has become larger than the minimum frequency

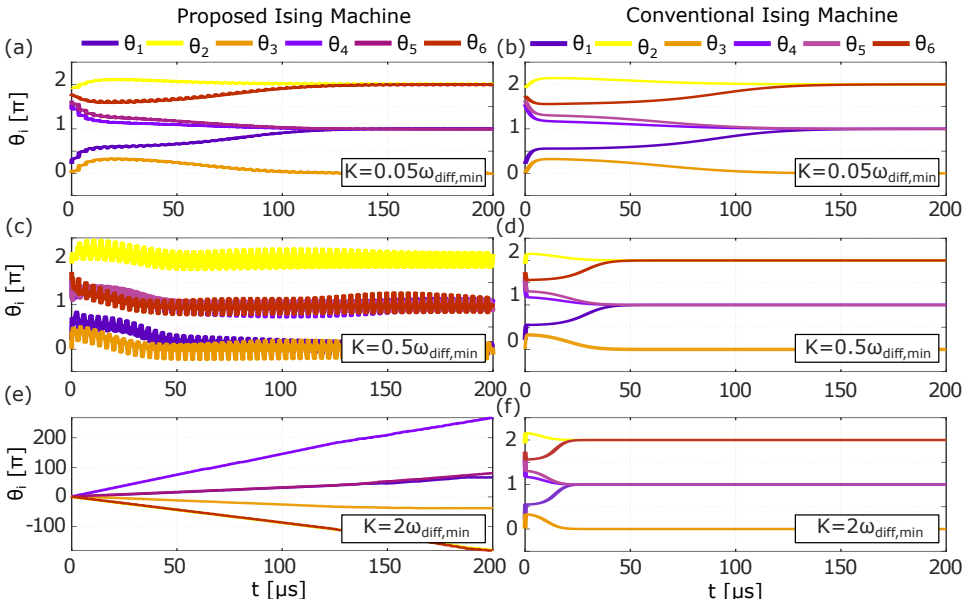


Figure 3.13: Comparison of the phase dynamics of the proposed implementation and conventional oscillator-based IMs.

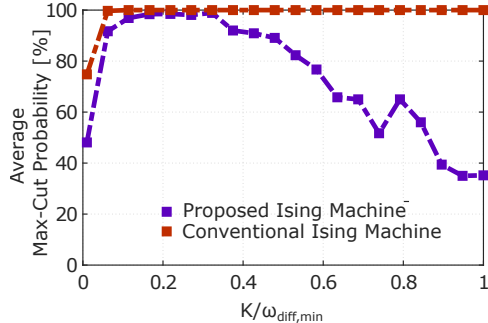


Figure 3.14: Max-Cut probability as a function of  $K/\omega_{\text{diff},\text{min}}$  for conventional oscillator-based IMs and the proposed implementation.

difference in the system, the oscillators are starting to synchronize (or pull each other) in frequency. Consequently, for correct operation of the proposed implementation, it is important that  $K$  is kept much smaller than  $\omega_{\text{diff},\text{min}}$ , such that the phase dynamics are dominated by the average of (3.22) (i.e. (3.24)).

To further characterize the impact of choosing  $K$  correctly, additional numerical simulations were performed. Fig. 3.14 shows the average Max-Cut probability of 10 randomly generated graphs of size  $N = 6$  (each simulated 100 times with different initial conditions) as a function of  $K$  normalized to  $\omega_{\text{diff},\text{min}}$ . The simulation results are presented for both, the conventional oscillator-based IM and the proposed implementation. For  $K/\omega_{\text{diff},\text{min}}$  in the range  $0.01 - 0.3$ , both implementations show a similar behaviour. Specifically, for a small ratio  $K/\omega_{\text{diff},\text{min}} < 0.05$ , the average Max-Cut probability for both implementations decreases because of the weak coupling in the network. This is a consequence of the phase dynamics being unable to converge within the fixed simulation time of  $t_{\text{end}} = 200 \mu\text{s}$ , resulting in a lower probability of finding the optimal solution. This behaviour is consistent with the one for the spintronic oscillator-based IM shown in Fig. 3.10(c), where the Max-Cut probability decreases as a function of the simulation time, for a fixed  $K$  (or equivalently reducing  $K$  while keeping  $t_{\text{end}}$  fixed). For  $0.05 < K/\omega_{\text{diff},\text{min}} < 0.3$ , both implementations find the Max-Cut solution with  $\approx 100\%$  probability, which corresponds to the optimal range of  $K$  for the proposed implementation, for this set of graphs with size  $N = 6$  and  $t_{\text{end}} = 200 \mu\text{s}$ . By further increasing  $K/\omega_{\text{diff},\text{min}}$  beyond 0.3, the performance of the proposed implementation drastically decreases. This is consistent with the transient simulations presented in Fig. 3.12, where it was observed that the phase dynamics of the conventional oscillator-based IM and the proposed implementation started to show qualitatively different phase dynamics around  $K = 0.5\omega_{\text{diff},\text{min}}$ . As it is confirmed with these numerical simulations, choosing  $K$  correctly and much smaller than  $\omega_{\text{diff},\text{min}}$  is critical for optimal performance of the proposed implementation.

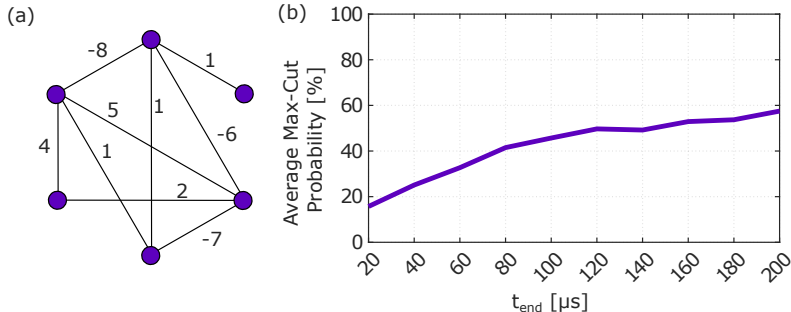


Figure 3.15: (a) An example of weighted Max-Cut problem and (b) the average Max-Cut probability as a function of simulation time  $t_{end}$ .

### 3.3.3 Weighted Graphs

In [Paper IV], the discussion is limited to unweighted Max-Cut graphs. Specifically, all the Max-Cut instances discussed in the manuscript are unweighted since the edges have a binary value of  $w_{i,j} = 1$  or  $w_{i,j} = 0$ . A more general case of the Max-Cut problem is the weighted Max-Cut where edges can have an arbitrary weight and sign, e.g. a 4-bit signed number. An example graph of size  $N = 6$  is presented in Fig. 3.15(a). Solving weighted problems on conventional oscillator-based IMs requires replacing the resistances in Fig. 3.12(a) with tunable resistances and additionally, introducing the possibility of inverting the signals to realize the sign (introducing a phase shift of  $\pi$  in the coupling function) of the weight. This could potentially introduce significant complexity in the coupling network of conventional oscillator-based IMs, especially considering that  $N(N - 1)$  coupling elements are needed. The proposed implementation can easily be used to solve weighted problems by simply extending the functionality such that the amplitude of the modulation signals  $c_{i,j}$  can take an arbitrary value within  $[-1, 1]$ . This does not introduce any additional complexity in the oscillator network itself, only in the generation of the modulation signals (i.e. they need to have a tunable amplitude). Numerical simulations demonstrating that the proposed oscillator-based IM can solve weighted Max-Cut problems are presented in Fig. 3.15. Similarly to the previously discussed simulation results, these Max-Cut problems are for a size of  $N = 6$ , but with signed weighted edges (integers from  $-8$  to  $7$ ). The numerical simulation results presented in Fig. 3.15 represent the average Max-Cut probability of 10 randomly generated weighted Max-Cut problems where each graph is solved 100 times (for each simulation time  $t_{end}$ ) by numerically simulating the DEs (3.22). While the Max-Cut probability is reduced compared to the unweighted problems, the proposed IM is able to consistently find the optimal solution of the weighted problems.

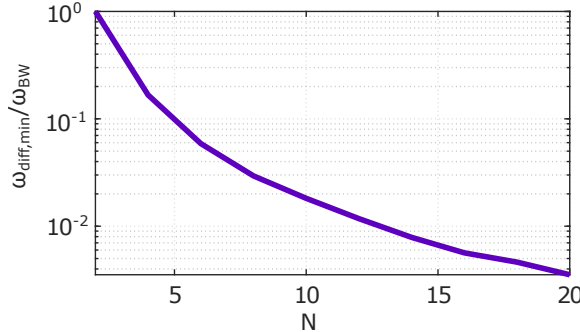


Figure 3.16:  $\omega_{diff,min}$  as a function of the number of oscillators  $N$  distributed in a bandwidth  $\omega_{BW} = \omega_{max} - \omega_{min}$ .

### 3.3.4 Scalability

The proposed approach allows for a highly reconfigurable oscillator-based IMs, where tunability and reconfigurability are achieved by simply changing the amplitudes of the modulation signals. However, the disadvantages of this method are also highlighted in [Paper IV]. There are two major considerations. Firstly, the operating frequencies are distributed according to a Golomb ruler to guarantee that the difference between any frequencies ( $\omega_i - \omega_j$ ) is unique. For a fixed bandwidth (assumed to be  $[\omega_{min}, \omega_{max}] = 2\pi[5 \text{ MHz}, 10 \text{ MHz}]$  in [Paper IV] for practical reasons), the minimum difference between any pair of oscillators  $\omega_{diff,min}$  scales exponentially with increasing number of oscillators. This trend is presented in Fig. 3.16. Consequently, as  $N$  increases, the design of the oscillators from a practical point (considering e.g. variability) becomes increasingly challenging for larger networks. Secondly, since  $\omega_{diff,min}$  scales with  $N$ , the coupling in the network needs to be reduced to fulfill the requirement that  $K \ll \omega_{diff,min}$ , which leads to longer convergence times. To overcome these challenges, a potential solution is explored which consists of interconnecting together cells of six oscillators sharing a common medium as presented in Fig. 4(a) in [Paper IV]. While the proposed implementation is limited to relatively sparse graphs, as it is discussed in detail in [Paper IV], graph-embedding could potentially address this issue and allow for arbitrary graphs to be mapped to the proposed architecture. Graph-embedding is a technique used to reduce the required number of interconnects and is most commonly employed in quantum annealers [173, 224]. In this approach, the graph of the problem to be solved and the graph of the hardware architecture are considered as two separate graphs. For clarity, the spins and couplings defining the problem (graph) to be solved will be referred to as "logical spins", while the graph defining interconnects of the circuits representing the spins and couplings will be called "physical spins". When graph-embedding is employed, the IM architecture is designed such that physical spin  $i$  is only con-

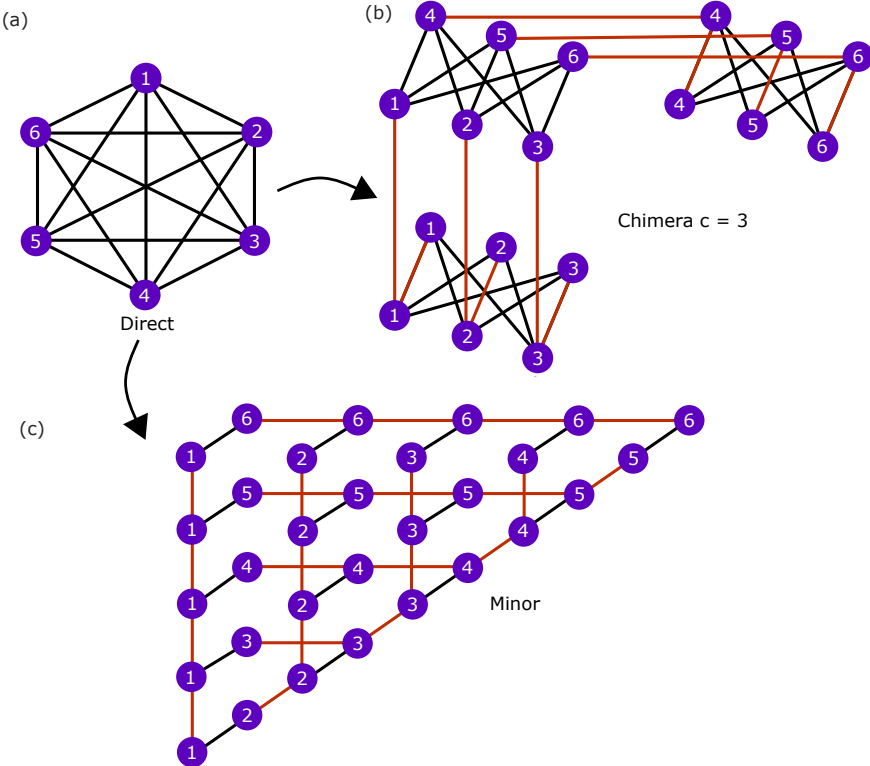


Figure 3.17: Illustration of graph embedding for chimera and minor embedding.

nected to  $M \ll N(N - 1)$  neighbouring physical spins. To represent an arbitrary graph of this architecture, a logical spin having more than  $M$  couplings to other logical spins needs to be mapped to more than a single physical spin. A simple example is presented in Fig. 3.17, which is a modified illustration from [224]. In this example, an all-to-all connected graph defining the couplings between logical spins is mapped to physical spins having a sparser connectivity. While the highest degree of the spins in the logical graph is 5, the highest degree of the physical spins is reduced to 4 and 3 in Fig. 3.17(b) and (c), respectively. Moreover, the physical graph in Fig. 3.17(b) has very few long range couplings between so called "unit cells", while they are more densely connected within unit cells. This eliminates the need for long range interactions, e.g. between spins on the opposite sites of the physical chip. As it can be observed from this example, a single logical spin, e.g. spin 1, is mapped to three physical spins which are strongly coupled (indicated by red interconnects). These strongly coupled spins effectively act like a single logical spin, allowing the physical architecture to realize  $N > 4$ , even though the physical architecture has at most  $M = 4$  ( $M = 3$ ) couplings to neigh-

bouring physical spins in Fig. 3.17(b) (3.17(c)). Graph embedding can be seen as a compiler step which introduces a significant computational overhead, especially for large graphs. Moreover, the need for multiple physical spins to represent a single logical spin also introduces a hardware overhead. For example, in D-Wave 2000Q which is based on a Chimera graph, 2000 physical q-bits are required to solve a problem of 64 logical spins with all-to-all couplings [173]. In spite of these disadvantages, graph-embedding has been used to address the lack of long range reliable couplings between superconducting qubits in quantum annealers [224].

While the examples presented here are based on the Chimera graph and minor embedding [174, 225, 226], other similar techniques based on different graphs, such as the Lechner-Hauke-Zoller (LHZ) scheme [227] or using Pegasus [228] and Zephyr graphs [229] for the physical layout of spins, have been explored. These techniques have mostly been explored in the context of quantum annealing, but are also applicable to other IMs. Therefore, the proposed architecture could potentially be used to realize the densely interconnected unit cells, such as in the Chimera graph (other graph embedding techniques have similar equivalents in terms of a unit cell). However, it was recently shown that using graph-embedding for quantum annealers might diminish the advantages of quantum annealers compared to software-based approaches [224, 230]. Consequently, more research is needed to explore the potential of using graph embedding and if this will diminish the advantages of the proposed architecture.

### 3.3.5 Proof-of-Concept, Limitations and Future Work

To further demonstrate that the proposed approach can be utilized to implement highly reconfigurable oscillator-based IMs, a proof-of-concept implementation was demonstrated in **[Paper IV]**. While this implementation consists of relatively simplistic elements and it is not optimized, it demonstrates the feasibility of the proposed approach. Moreover, in supplementary material of **[Paper IV]**, it is shown how the DEs describing the operation principles of the ring oscillators can be simplified to a form similar to (3.22).

However, to fully characterize the proposed approach, further analysis is needed. Specifically, analysing the impact of variability is an important next step. While conventional oscillator-based IMs have been shown to be relatively resilient to variability in operating frequencies, it is currently unclear if this property translates to the proposed implementation. Additionally, the impact of noise and other non-idealities needs to be further studied.

## 3.4 Duffing Oscillator-based Ising Machines

Over the last few years, oscillator-based IMs based on phase binarization and phase coupled oscillators have received a widespread interest, as it was already discussed in the previous sections. However, other dynamical systems have also

been extensively explored to realize IMs [190, 231–234]. One of these approaches is the previously discussed SB algorithm [189, 190]. As the name suggests, this approach is based on simulating the dynamics of a system exhibiting bifurcations. Bifurcations are qualitative changes in the dynamics of a system, which are generally induced by a small and smooth change of a control parameter (the bifurcation parameter). Although many different types of bifurcations exist, under certain conditions these qualitative changes can be used to realize a dynamical system that tries to find the ground state of the Ising Hamiltonian. The SB algorithm is based on these principles and has shown promising performance as an algorithmic approach to solve the Ising model. Moreover, when it is implemented on FPGAs/graphics processing units (GPUs), as in [189, 190, 235], this approach outperforms many of the state-of-the-art IMs, making it a promising approach. Additionally, modeling of dynamical systems using analog circuits has been extensively explored in literature [236–240]. These systems include e.g. Duffing oscillators [239] and Chua’s circuit [237, 238], which exhibit various interesting characteristics, including bifurcations and chaos. The combination of the SB algorithm with the use of analog circuits for modeling dynamical systems opens up the possibility of realizing IMs based on bifurcations in analog circuits, as it was proposed in **[Paper V]**. To demonstrate this approach, an analog Duffing oscillator-based IM was proposed in **[Paper V]**.

In this section, the most important characteristics of Duffing oscillators for realizing IMs are discussed in detail and a background on the operation principles of the SB algorithm presented. Additionally, details on the circuit implementation of the Duffing oscillator in **[Paper V]** are provided. Finally, a proof-of-concept, built using prototyping boards, is presented along with the corresponding experimental results that further support the proposal in **[Paper V]**.

### 3.4.1 Duffing Oscillators

The conventional driven damped Duffing equation is generally written as [241, 242]:

$$\frac{d^2}{dt^2}x + \delta \frac{d}{dt}x + \alpha x + \beta x^3 = \gamma \sin(\omega t) \quad (3.25)$$

where  $x$  is the displacement,  $\delta$  is a damping term,  $\alpha$  is a stiffness parameter,  $\beta$  determines the nonlinearity in the system,  $\gamma$  is the amplitude of the driving signal and  $\omega$  the driving frequency. Equivalently, this system can be written as two first order equations as in [242]:

$$\frac{d}{dt}x = y \quad (3.26a)$$

$$\frac{d}{dt}y = F(x) - \delta y + \gamma \sin(\omega t) \quad (3.26b)$$

where  $F(x) = -\alpha x - \beta x^3$ . Depending on the choice of  $\alpha$  and  $\beta$ , the dynamics

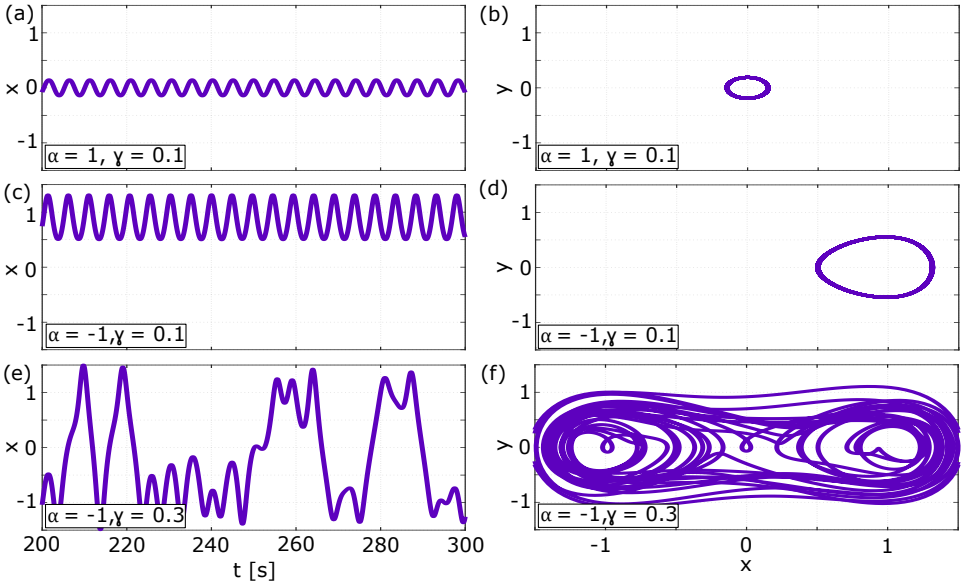


Figure 3.18: Numerical simulations of the Duffing oscillator transient and phase portrait for different values of the stiffness  $\alpha$  and the driving strength  $\gamma$ .

of the system can exhibit a number of characteristics. For example, for  $\alpha, \beta > 0$ , the system has a single fixed point, while for  $\alpha < 0$  and  $\beta > 0$ , there are two stable and one unstable fixed points [242, 243]. Numerical simulations of the DEs (3.26) showing the transient and the phase portrait for these two cases are presented in Figs. 3.18 (a)-(d) for  $\delta = 0.1$ ,  $\omega = 1.3 \text{ rad/s}$ , and assuming  $\beta = 1$  for different values of  $\alpha$ . These numerical simulations are performed using ODE45 from Matlab. It is worth highlighting that for  $\alpha = -1$ , the oscillation can center around either  $-1$  or  $1$  depending on the initial condition. Moreover, by increasing the external signal  $\gamma$  to  $0.3$ , as presented in Fig. 3.18 (e)-(f), the dynamics become chaotic. The transition, from a single stable fixed point around the origin to two new stable fixed points, highlights that a bifurcation takes place when  $\alpha = 0$  as is well known for the Duffing oscillator. To demonstrate this, the fixed points (i.e.  $dx/dt = dy/dt = 0$ ) of (3.26), assuming  $\delta = \gamma = 0$ , can be found as  $(x^*, y^*) = (0, 0)$  and [242]:

$$(x^*, y^*) = (\pm \sqrt{\frac{-\alpha}{\beta}}, 0) \quad (3.27)$$

if  $\alpha$  and  $\beta$  have opposite signs (i.e. (3.27) has a real solution). By further analysing the fixed points, it can be shown that  $(0, 0)$  is stable for  $\alpha > 0$  and unstable for  $\alpha < 0$ , while (3.27) is stable for  $\alpha < 0$ . These characteristics are summarized in Fig. 3.19(a), which highlights that the Duffing oscillator goes

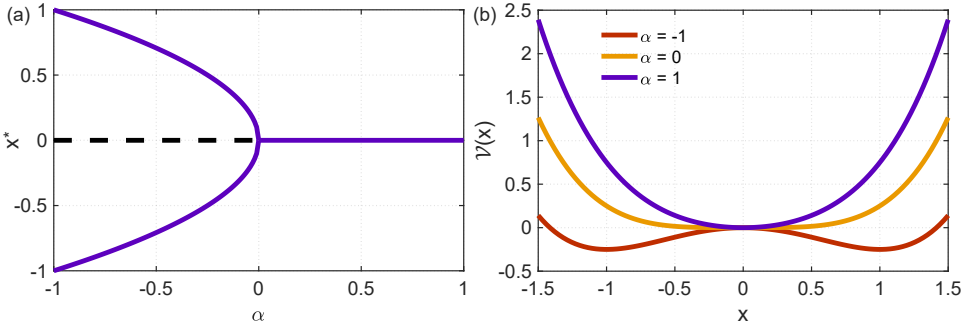


Figure 3.19: (a) Bifurcation diagram of a Duffing oscillator as a function of  $\alpha$  with  $\beta = 1$ , solid lines represent stable fixed points and dotted lines unstable fixed points. (b) The potential  $V(x)$  for three different values of  $\alpha$ .

through typical pitchfork bifurcation when  $\alpha$  changes sign [242]. Alternatively, the pitchfork bifurcation can be understood by analysing the potential, assuming again  $\delta = \gamma = 0$ :

$$V(x) = - \int F(x)dx = \alpha \frac{x^2}{2} + \beta \frac{x^4}{4} \quad (3.28)$$

Plotting this potential, as presented in Fig. 3.19(b), it becomes apparent that as  $\alpha$  changes from 1 to  $-1$ , the fixed point at  $x^* = 0$  disappears when  $\alpha = 0$  and two new fixed points appear at (3.27). Moreover, in Fig. 3.19(b) it can also be seen that the depth of the minima (fixed-points) depends on  $\alpha$  for  $\alpha < 0$ . These rich dynamics of the Duffing equation are the basis for realizing IMs based on bifurcations as it is discussed in the following section.

### 3.4.2 Simulated Bifurcation

Simulated Bifurcation is a recently proposed algorithm targeted at solving the Ising model. The algorithm is inspired by the equations describing a quantum annealer/IM, consisting of a network of coupled Kerr-nonlinear parametric oscillators [244]. In [190], H. Goto, et al. derive a set of simplified classical DEs from the quantum Hamiltonian, written as:

$$\frac{d}{dt}x_i = y_i \quad (3.29a)$$

$$\frac{d}{dt}y_i = -x_i^3 - \alpha x_i + c_0 \sum_{j=1}^N J_{i,j}x_j \quad (3.29b)$$

where  $x_i$  and  $y_i$  are the position and momentum of a particle,  $c_0$  is a constant,  $\alpha$  is the stiffness and the last term on the right hand-side of (3.29b) is a coupling

term. Comparing these DEs to the Duffing equations (3.26), it is apparent that it is simply a network of coupled Duffing oscillators with  $\beta = 1$  and  $\delta = \gamma = 0$ . By numerically simulating the dynamics of (3.29), where  $\alpha$  is gradually changed such that the Duffing oscillators pass the bifurcation point, this system can be used as an algorithm for solving the Ising model. In this approach, the position of the particle  $x_i$ , after the bifurcation, represents the spin state in the Ising Hamiltonian. Specifically,  $\sqrt{-\alpha}$  represents a spin state +1 and  $-\sqrt{-\alpha}$  the spin state -1. The functionality is best explained with a simple example. Consider two AFM coupled spins, so (3.29) can then be written as:

$$\frac{d}{dt}x_1 = y_1 \quad (3.30a)$$

$$\frac{d}{dt}y_1 = -x_1^3 - \alpha x_1 + c_0 J_{1,2} x_2 \quad (3.30b)$$

$$\frac{d}{dt}x_2 = y_2 \quad (3.30c)$$

$$\frac{d}{dt}y_2 = -x_2^3 - \alpha x_2 + c_0 J_{2,1} x_1 \quad (3.30d)$$

where  $J_{1,2} = J_{2,1} = -1$  to achieve AFM coupling between the two oscillators/spins. To solve this simple two spin problem,  $c_0$  is chosen as 0.2 and  $\alpha$  is linearly ramped from 1 to -1, resulting in bifurcations. The numerical simulation results for the DEs (3.30) are presented in Fig. 3.20(a). For  $\alpha < 0$ , only a single stable fixed point at  $x^* = 0$  exists and consequently, the Duffing oscillators are both initially centered around zero. As  $\alpha$  passes the bifurcation point around

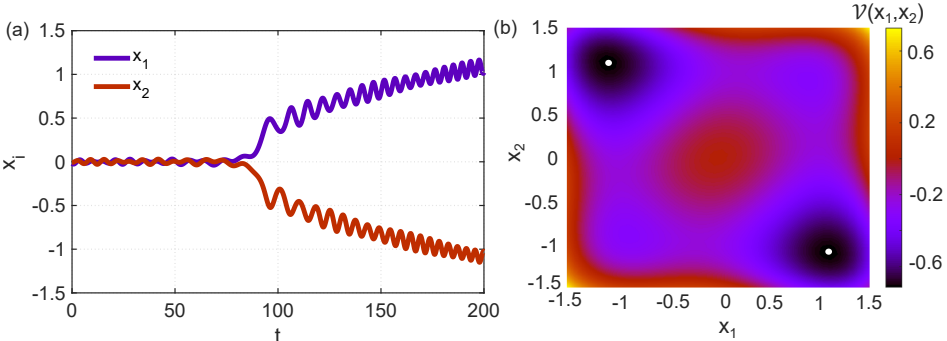


Figure 3.20: (a) Numerical simulations of two AFM coupled Duffing oscillators and (b) the potential  $V(x_1, x_2)$  for two AFM coupled Duffing oscillators when  $\alpha = -1$ . The potential minima are marked with a white circle.

$\alpha = 0$ , the fixed point around zero becomes unstable and two fixed points appear at  $x^* = \pm\sqrt{-\alpha}$ , similar to what was discussed in the previous section. However, since the oscillators are coupled together through the term  $J_{i,j}x_j$ , they affect the dynamics of each other. The impact of the coupling can be understood by analysing the potential  $\mathcal{V}(x_1, x_2)$  of the coupled equations (3.30), which can be written as [190]:

$$\mathcal{V}(x_1, x_2) = \frac{x_1^4}{4} + \alpha \frac{x_1^2}{2} + \frac{x_2^4}{4} + \alpha \frac{x_2^2}{2} - \frac{c_0}{2} J_{1,2} x_1 x_2 - \frac{c_0}{2} J_{2,1} x_2 x_1 \quad (3.31)$$

for the two spin example. This potential is plotted as a function of the positions  $x_1$  and  $x_2$  in Fig. 3.20(b), for  $\alpha = -1$  (after the bifurcation). As it can be observed from the potential, the oscillators prefer to settle to opposite fixed points, i.e.  $(x_1, x_2) = (\sqrt{-\alpha}, -\sqrt{-\alpha})$  or  $(x_1, x_2) = (-\sqrt{-\alpha}, \sqrt{-\alpha})$ , as a consequence of the coupling between them. These preferred states represent the ground state of the Ising model for this simple two spin example with AFM coupling. Similarly, for FM coupling ( $J = 1$ ), the states  $(x_1, x_2) = (\sqrt{-\alpha}, \sqrt{-\alpha})$  and  $(x_1, x_2) = (-\sqrt{-\alpha}, -\sqrt{-\alpha})$  become the potential minima. Finally, for the uncoupled case ( $J=0$ ), the oscillators are uncoupled and all combinations of  $(x_1, x_2) = (\pm\sqrt{-\alpha}, \pm\sqrt{-\alpha})$  have equal potentials.

For larger Ising models, consisting of  $N$  spins, the potential in Fig. 3.20(b) becomes  $N$  dimensional with a potential minima (ground state) that is set by the coupling coefficients  $J_{i,j}$ . Consequently, a network of Duffing oscillators can be used as an IM by utilizing their bifurcation properties. This approach was demonstrated in [190] by implementing the algorithm on a FPGA and benchmarking it against a CIM and SA on a 2000 node graph. The results showed that SB outperforms both approaches in computational speed, specifically SA by around 100x and CIM 10x. Later, in [189], the SB algorithm was further optimized and compared to various FPGA implementations, ASICs, CIM and QA, demonstrating again that the SB algorithm outperforms many of the above implementations, on many different problems. Consequently, SB is a promising approach for realizing next generation IMs. Inspired by this approach, we explored an alternative implementation based on analog circuits that emulate the dynamics of SB. This approach is discussed in the following sections.

### 3.4.3 Analog Circuit Implementation of Duffing Oscillators

Circuit implementations of dynamical systems exhibiting various characteristics have been extensively studied in literature. For instance, in [239], a simple electrical circuit emulating the dynamics of the Duffing oscillator (3.26), for testing chaos control techniques, is presented. The analog implementation of the SB algorithm using Duffing oscillators, is inspired by this proposal. However, the implementation in [239] lacks the possibility of tuning  $\alpha$  as it is required to realize the bifurcations (as discussed in the previous section). To address this aspect, the implementation in [239] was modified slightly by introducing a voltage controlled

negative resistance. The schematic of the proposed implementation is presented in Fig. 1(a) in [Paper V] and the DEs describing the voltage  $V_c$  on the capacitor  $C$  and the current  $I_L$  through the inductor  $L$ , can be written as [239]:

$$C \frac{dV_c}{dt} = I_L \quad (3.32a)$$

$$L \frac{dI_L}{dt} = F_E(V_c) - I_L R_2 + \frac{R_3}{R_4} V_{in} \quad (3.32b)$$

where  $F_E(V_c)$  is a piecewise function, approximated as:

$$F_E(V_c) = \begin{cases} -V_c - kV^* & V_c < -V^* \\ (k-1)V_c & -V^* \leq V_c \leq V^* \\ -V_c + kV^* & V_c > V^* \end{cases} \quad (3.33)$$

where  $V^*$  is the voltage drop across an open diode,  $V_{in} = A\sin(\omega t)$ ,  $k = 1 + R_3/R_4 + R_3/R_5(t)$  and  $R_5(t)$  is the voltage controlled negative resistance. An in-depth analysis of (3.32) and (3.33) is presented in [Paper V]. Here we will focus on demonstrating that (3.32) closely resembles the general Duffing oscillator presented in (3.26) and highlight the differences and implications this might have. The following dimensionless variables and parameters are introduced in (3.32) (similar to what is done in [239]):

$$\begin{aligned} x &= \frac{V_c}{kV^*}, & y &= \frac{\rho I_L}{kV^*}, & \frac{t}{\sqrt{LC}} &\rightarrow t, \\ \omega\sqrt{LC} &\rightarrow \omega, & \gamma &= \frac{R_3}{R_4} \frac{A}{kV^*}, & \delta &= \frac{R}{\rho}, & \rho &= \sqrt{\frac{L}{C}} \end{aligned}$$

then (3.32) becomes:

$$\frac{dx}{dt} = y \quad (3.34a)$$

$$\frac{dy}{dt} = F_E(x) - \delta y + \gamma \sin(\omega t) \quad (3.34b)$$

where  $F_E(x)$  is now:

$$F_E(x) = \begin{cases} -(x+1) & x < -1/k \\ (k-1)x & -1/k \leq x \leq 1/k \\ -(x-1) & x > 1/k \end{cases} \quad (3.35)$$

This transformation allows for a direct comparison of (3.26) and (3.34), while in [Paper V] all analysis is directly performed using (3.32). It is clear that

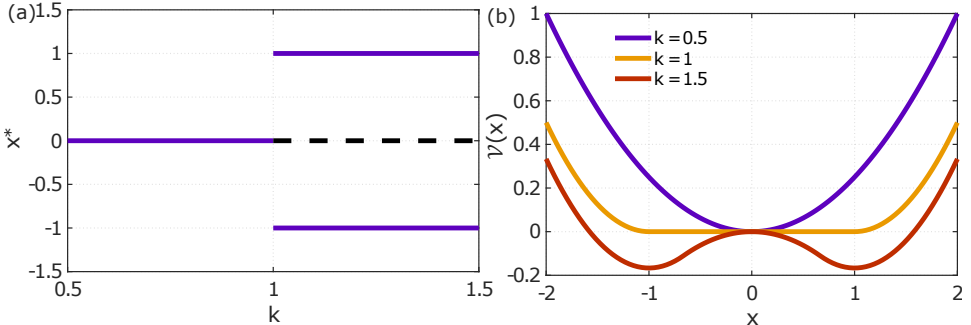


Figure 3.21: (a) The bifurcation diagram of the electrical Duffing oscillator and (b) the potential  $V(x)$  for different values of  $k$  ( $R_5$ ).

(3.26) and (3.34) are equivalent but the resemblance between  $F_E(x)$  in (3.35) and  $F(x) = -\alpha x - \beta x^3$  is less clear. However, by analysing the fixed points of (3.35), it can be shown that they exhibit similar properties, where  $k$  serves a similar role as  $\alpha$  in  $F(x)$ . Considering again the case  $\delta = \gamma = 0$ , the fixed points of (3.34) can be written as:

$$(x^*, y^*) = (0, 0), \quad (x^*, y^*) = (-1, 0), \quad (x^*, y^*) = (1, 0)$$

However, the non-zero fixed points only exist under the conditions that  $k > 1$ . Moreover, by analysing the derivatives, it can be shown that  $(x^*, y^*) = (0, 0)$  is stable for  $k \leq 1$ , but becomes unstable for  $k > 1$ . Since  $k = 1 + R_3/R_4 + R_3/R_5(t)$  (where  $R_5(t)$  is the voltage controlled negative resistance),  $R_5(t)$  (i.e.  $k$ ) can be used as the control parameter for the bifurcations, similar to  $\alpha$  in (3.26). This analysis is summarized in Fig. 3.21 (a) where the bifurcation diagram is presented. Compared to the pitchfork bifurcations in ideal Duffing oscillators (Fig. 3.19), the bifurcations present in this circuit is clipped since the fixed points do not gradually emerge from zero, but instead spontaneously appear at  $\pm 1$ , as  $k$  crosses 1, the bifurcation point. Finally, for completeness, the potential of the proposed Duffing oscillator can be written as (for the transformed form as presented in (3.34) and (3.35)):

$$V(x) = - \int F_E(x) dx = \frac{1}{2} \begin{cases} x^2 + 2x + 1/k & x < -1/k \\ -(k-1)x^2 & -1/k \leq x \leq 1/k \\ x^2 - 2x + 1/k & x > 1/k \end{cases} \quad (3.36)$$

which is presented in Fig. 3.21 (b). Although both, the bifurcation and the potential, have a slightly different form compared to the ideal Duffing oscillator, the overall behaviour and dynamics are accurately captured by the circuit implementation, when  $R_5(t)$  is introduced. Moreover, this is further demonstrated in [Paper V] based on numerical simulations of the DEs. Moreover, in [Paper

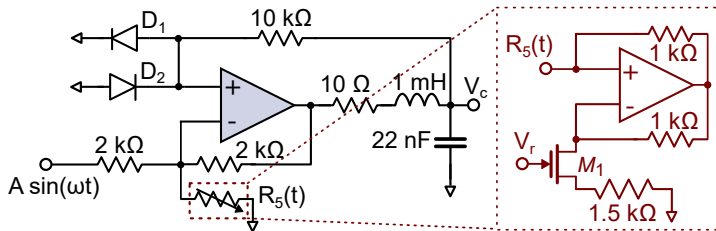


Figure 3.22: Analog implementation of the Duffing oscillator with a tunable  $k$  ( $R_5$ )

[V], the analysis performed above is extended to networks of coupled Duffing oscillators and it is shown that the behaviour closely resemble the SB algorithm. Finally, numerical simulations of DEs describing large Duffing oscillator networks (up to  $N = 2000$ ) were performed, where various Max-Cut problems were used to verify the functionality.

### 3.4.4 Proof-of-Concept Prototype and Experimental Results

The above analysis has been based on relatively idealized descriptions and numerical simulations of DEs. To proof the functionality of analog Duffing oscillator-based IMs, a proof-of-concept prototype was developed. Since the proposed approach can be easily implemented using on-the-shelf components, the prototype was built on a breadboard. The circuit implementation is presented in Fig. 3.22, where the tunable negative resistance  $R_5(t)$  is implemented with a negative impedance converter. Measurement results, demonstrating the functionality of a single Duffing oscillator are presented in Fig. 3.23, for an applied signal with  $\omega = 2\pi \cdot 31 \text{ kHz}$ , while varying the amplitude  $A$  and the resistance  $R_5(t)$ . It is worth mentioning that for the purpose of the measurements presented in Fig. 3.23,  $M_1$  was replaced with a resistor (since there is no need to continuously change  $R_5(t)$  for these 'static' measurements). According to the analysis of the electrical Duffing oscillator in the previous section (or equivalently in [Paper V]), the bifurcation point is ideally at  $R_5(t) = -2 \text{ k}\Omega$ , which is when  $k = 1$ . In Fig. 3.23 (a) the transient and (b) the phase portrait for  $R_5(t) = R_5 = -1.7 \text{ k}\Omega$  and  $A = 100 \text{ mV}$  are presented. As expected, the oscillations center around  $V_c = 0 \text{ V}$ . By further decreasing  $R_5$  to  $-1.9 \text{ k}\Omega$  the dynamics cross the bifurcation point and settle around  $V_c \approx -0.3 \text{ V}$ , as shown in Fig. 3.23 (c)-(d). Ideally, the bifurcation should take place at  $R_5 = -2 \text{ k}\Omega$  but due to non-idealities (e.g. resistor tolerances and diode conductance) this point is slightly shifted to  $-1.9 \text{ k}\Omega$ . This measurement was repeated multiple times and the Duffing oscillator always settled around  $V_c \approx -0.3 \text{ V}$ , but never at the other fixed point  $V_c \approx 0.3 \text{ V}$ . For an ideal Duffing oscillator, it should be equally likely that the Duffing oscillator settles at either of the fixed points after the bifurcation point. However, by adding a DC offset of  $\approx 5 \text{ mV}$  to the input signal  $V_{in}$ , the oscillations

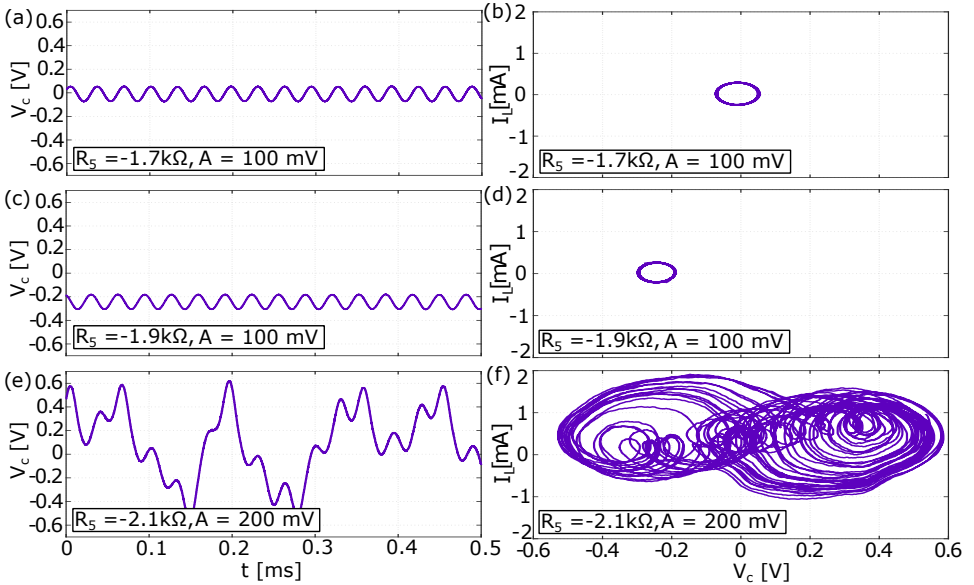


Figure 3.23: Measured transients and phase portraits for different values of  $R_5(t)$  ( $k$ ) and the amplitude  $A$ , for a single Duffing oscillator.

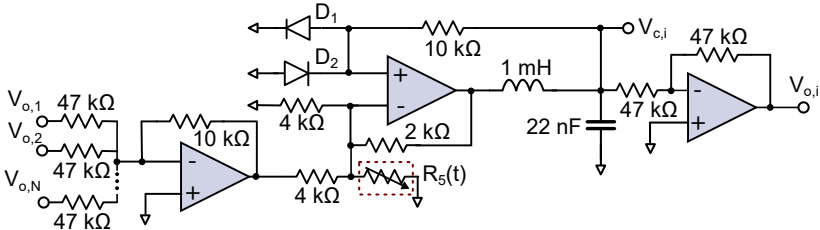


Figure 3.24: A single electrical Duffing oscillator  $i$  and the additional circuitry required to couple it to  $N$  other oscillators.

settle around  $V_c \approx 0.3 \text{ V}$  (not shown here), confirming that both fixed points are present. Finally, by decreasing  $R_5$  to  $-2.1 \text{ k}\Omega$  and  $A = 200 \text{ mV}$ , the dynamics become chaotic, as presented in Fig. 3.23 (e)-(f). By comparing the measurement results with the ideal Duffing oscillator in Fig. 3.18, it can be concluded that the circuit implementation shows very similar dynamical properties.

As a first step towards experimentally demonstrating the functionality of a Duffing oscillator-based IM, the simplest possible example is considered. This example consists of two AFM coupled spins, similar to the previously presented example for the SB algorithm. Each oscillator is designed as shown in Fig. 3.24. Note that the design presented in Fig. 3.24 is for a general network of  $N$  oscillators. The experimental implementation is similar to the one presented in [Paper]

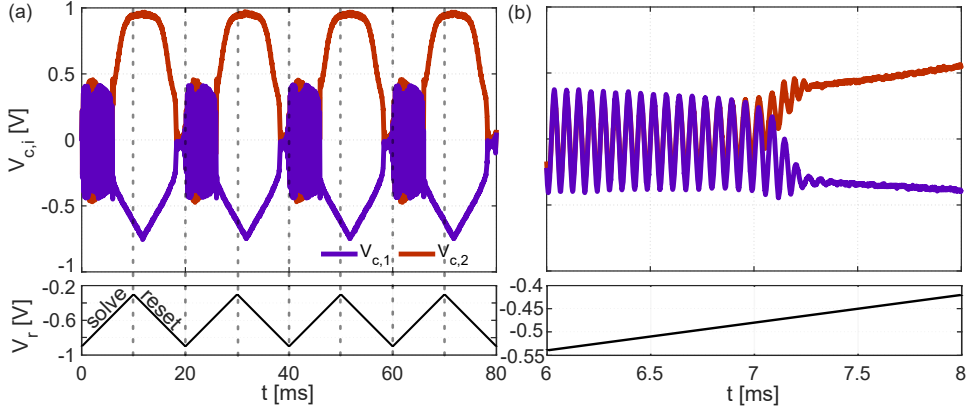


Figure 3.25: Measurement results of (a) two coupled Duffing oscillators over four periods of the triangular waveform applied to  $V_r$  and (b) a zoomed in version of (a) highlighting the bifurcation point.

$\mathbf{V}$ ], but  $R_2 = 10 \Omega$  resistor has been removed since in practice, the inductor has an internal resistance which is a few ohms. This parasitic resistance introduces the damping  $\delta$  and there is no need for an additional resistance  $R_2$ . Additionally, for simplicity, an inverting unity gain amplifier is used at the output instead of a comparator as in [Paper V]. The comparator is expected to improve the performance of the IM, but for the small networks considered here this improvement is negligible. The purpose of the amplifier is simply to invert the signal such that the oscillators are AFM coupled (i.e.  $J_{i,j} < 0$ ). Finally, a summing amplifier that is connected to the outputs  $V_{o,j}$  of other Duffing oscillators in the networks, introducing the necessary coupling between oscillators, is added at the input. The measurement results for two AFM coupled Duffing oscillators are presented in Fig. 3.25. The negative resistance  $R_5(t)$  is ramped by linearly changing the gate voltage of the JFET  $V_r$  from  $-0.9 \text{ V}$  to  $-0.3 \text{ V}$ , over  $10 \text{ ms}$ . As it is shown in Fig. 3.25 (a)-(b), this induces bifurcations in the Duffing oscillators and they settle to opposite states, corresponding to the ground state of this simple example. To reset the system,  $V_r$  is linearly ramped again to  $-0.9 \text{ V}$ , which resets the oscillators back to zero. Since finding the ground state of large spin networks is a statistical process, a triangular wave is applied to  $V_r$ . The solution for each run is then read by analysing which  $V_{c,i} > 0$  at the peak of the triangular wave. As presented in Fig. 3.25 (a), the same solution is found in each of these four runs, specifically, the solution  $[V_{c,1}, V_{c,2}] \approx [0.5 \text{ V}, -0.5 \text{ V}]$ , which corresponds to a spin alignment  $[s_1, s_2] = [1, -1]$  in the Ising Hamiltonian. By further analysing the behaviour for 100 runs, it was observed that the same solution is always found, but the degenerate ground state solution  $[-1, 1]$  is never found. The reason for this is suspected to be the input offsets of the opamps, which makes each spin (i.e. oscillator) favor a certain spin state over the other. This is an important

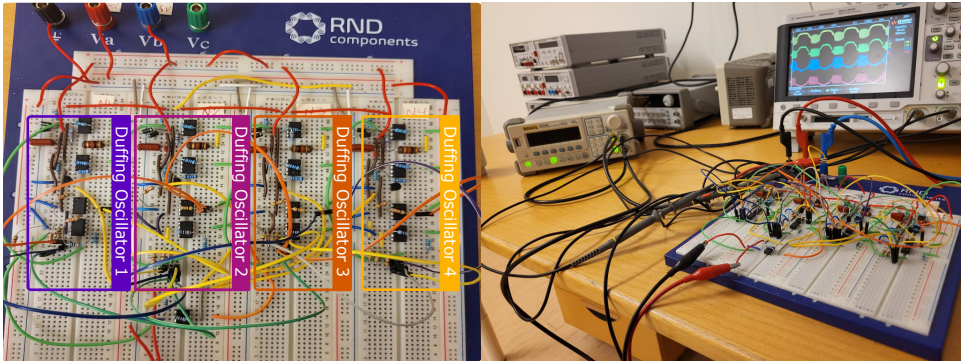


Figure 3.26: Experimental setup of four coupled Duffing oscillators on a prototyping board.

observation that will need to be further explored in the future and the impact this might have on large networks.

To further demonstrate that a network of coupled Duffing oscillators can be used as an IM, measurements on a small network consisting of  $N = 4$  coupled Duffing oscillators were performed, as presented in Fig. 3.26. To demonstrate the functionality of the Duffing oscillator-based IM, small Max-Cut problems are mapped to the architecture. An example is presented in Fig. 3.27(a) and (b), where a graph of four all-to-all connected nodes with uniform weights  $w_{i,j} = w = 1$  is solved. This graph is mapped to the architecture by connecting all oscillators to each other with a coupling  $J_{i,j} \propto -w_{i,j}$  (corresponding to 4 all-to-all AFM coupled oscillators). Similarly to the two spin problem, the Max-Cut solution is found by ramping the gate voltage of the JFET  $V_r$  from  $-0.9$  V

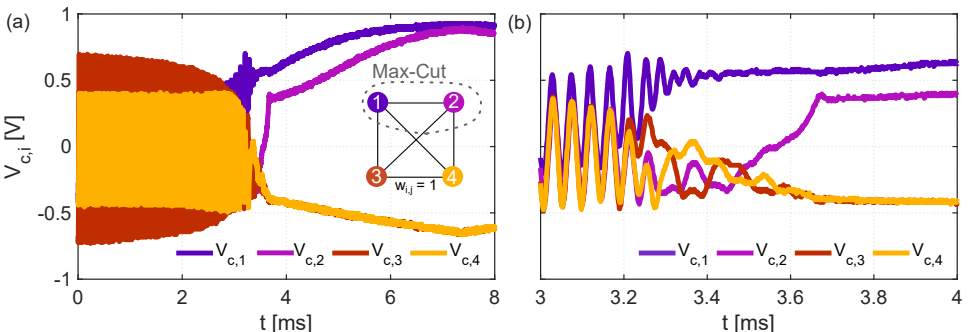


Figure 3.27: Measurement results of (a) four coupled Duffing oscillators solving a small Max-Cut problem (inset: the four node graph with one of the Max-Cut solutions highlighted) and (b) a zoom of the results in (a).

to  $-0.3$  V, over 10 ms. A transient response of the Duffing oscillator network passing the bifurcation point is presented in Fig. 3.27. This simple Max-Cut problem has six solutions, which consist of any two oscillators in set 1, while the other two are in set 2. Any other solution has a lower cut value than the Max-Cut = 4. As it is shown in Figs. 3.27(a)-(b), the network quickly settles to a solution corresponding to  $[V_{c,1}, V_{c,2}, V_{c,3}, V_{c,4}] = [0.5$  V, 0.5 V,  $-0.5$  V,  $-0.5$  V] or equivalently,  $[s_1, s_2, s_3, s_4] = [1, 1, -1, -1]$ . To further characterize the performance of the Duffing oscillator-based IM, the results of 100 independent runs are extracted by applying the triangular waveform for 2 seconds. The results are presented in Fig. 3.28 (a), where the Max-Cut solution is found in 99 out of the 100 runs. Similar behaviour as for the two-spin problem was observed here. The IM is unable to find all ground states during these 100 runs, indicating again that there is a significant bias towards certain solutions in the network. To analyse if this behaviour impacts the performance of the proposed IM, three other graphs were mapped to the architecture as presented in Fig 3.28(b)-(d). To map these graphs to the architectures, the connections between oscillators corresponding to the absent edges are simply removed. For example, in Fig. 3.28(b), the edge  $w_{1,4}$  has been removed. This means that the connection from  $V_{o,1}$  to the summing amplifier of  $V_{o,4}$  is removed and the corresponding summing amplifier terminal is connected to ground (and vice versa for  $V_{o,4}$  to the summing amplifier of  $V_{o,1}$ ). From the results presented in Figs. 3.28(b)-(d), the Duffing oscillator-based IM is able to consistently find the Max-Cut solution for all of these graphs. Consequently, the impact of the bias towards certain solutions is not enough to result in incorrect solutions, in such small graphs. However, as it

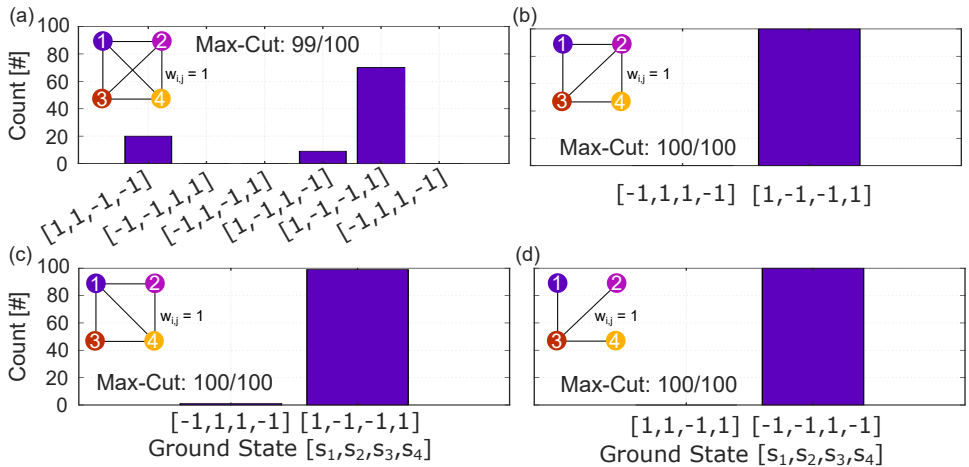


Figure 3.28: Distribution of the ground states in 100 runs for different graphs of size  $N = 4$ . Note that each of the plotted solution corresponds to a ground state/Max-Cut solution.

was mentioned earlier, the impact of the offset voltage on larger networks will need to be further explored in the future.

### **3.4.5 Limitations and Future Work**

This work is the first step towards analog IMs based on bifurcations. As a proof-of-concept, the Duffing oscillator was employed in this study since its behaviour resembles the simplified classical equations describing a quantum annealer. This approach brings opportunities, but also challenges, especially when implementing large networks. Consequently, future work could include exploring other electrical circuits, which can be more easily scaled to large networks, while exhibiting similar behaviour to the bifurcation properties of the Duffing oscillator.

## Chapter 4

# Conclusions and Future Work

In this thesis, the possibility of employing both emerging spintronic and established electronic oscillators, in applications extending beyond their conventional use, have been explored. While spintronic oscillators exhibit many desirable characteristics for communication systems, magnetic field detection, neuromorphic computing and even Ising machines, they currently exhibit various major challenges that need to be overcome. So, extensive research is still required on this technology until spintronic oscillators can reach a widespread use in electronic systems for those applications.

Three-terminal SHNOs are emerging spintronic oscillators that could potentially combine the advantages of STNOs (high output power) and nanoconstriction SHNOs (synchronization in large arrays). Consequently, as a first step towards the exploration of applications based on three-terminal SHNOs, a behavioural model compatible with EDA tools was developed. The proposed behavioural model captures the most important characteristics of three-terminal SHNOs, such as output power, phase noise, DC operating point, operating frequency and voltage controlled magnetic anisotropy. Additionally, the behavioural model was verified against experimental results from literature. Depending on the development of the three-terminal SHNOs the behavioural model could be extended to allow for simulations of three-terminal SHNO networks together with CMOS circuits.

An interesting characteristic of spintronic oscillators is the substantial multi *GHz* change in the operating frequency as a function of relatively small changes in the external magnetic field. Consequently, the possibility of using this unique property to realize time-based magnetic field sensors has been explored. It was shown that spintronic oscillator-based magnetic field sensors can in theory lead to performance similar to state-of-the-art magnetic field sensors of similar size. It was also shown that the achievable performance is largely limited by the phase noise characteristics of the modeled spintronic oscillator. Future work could further explore the performance of the proposed architecture, by tailoring the spin-

tronic oscillator materials and geometry to maximize  $K_{STNO}$ . Alternatively, employing synchronized spintronic oscillator arrays to reduce the phase noise and improve the performance is also a promising direction.

Solving hard CO problems using oscillator-based IMs, which has various applications including logistics, machine learning, material science etc., has also been explored in this thesis. Spintronic oscillators with their extremely small size, high operating frequency and unique coupling mechanism are an interesting candidate for this application. However, spintronic oscillators exhibit qualitatively different characteristics compared to conventional electronic oscillators. Consequently, the first step toward spintronic oscillator IMs was to confirm that they exhibit all the required characteristics needed for IMs. This was verified in [Paper III] with numerical simulations of spintronic oscillator networks operating as IMs. However, this work did not consider the different types of coupling mechanisms (electrical, exchange, spin-wave) and the benefits or challenges associated with each. The different types of coupling mechanisms are a unique characteristic of spintronic oscillators, which open new possibilities compared to CMOS oscillators (which can only be coupled together using electrical means). Considering that IMs require a large amount of couplings between spins (oscillators), an important future work is to explore if spintronic oscillators with their unique coupling mechanism can overcome the challenges related to large scale oscillator-based IMs implementation.

An alternative approach to realizing oscillator-based IMs was also explored. The proposed approach allows for highly reconfigurable and tunable coupling strength which can potentially address some of the challenges associated with IMs. However, the proposed approach based on quasiperiodically modulated coupling strength also comes with various challenges which need to be further investigated. These challenges include the need to have a weak coupling in the network leading to longer convergence times, and the potential need for graph embedding that could introduce a computational overhead. However, it is still an open research question if the disadvantages observed with graph embedding in quantum annealers translate to oscillator-based IMs. Consequently, the proposed architecture needs to be further explored and benchmarked on standard Max-Cut problems to allow for comparison with other IMs. Moreover, the impact of noise and variability are important considerations that need to be explored in future work.

Lastly, the potential of realizing an analog IMs based on bifurcations in networks of Duffing oscillators was explored. This proposal was numerically investigated and evaluated, and later validated by a small proof-of-concept prototype. This approach was inspired by the SB algorithm, which is based on simplified dynamical equations describing a quantum annealer. The SB algorithm has shown promising performance and the proposed approach is a first step towards realizing IMs based on bifurcations in analog circuits. Future work could focus on investigating and developing circuits that exhibit similar characteristics, but are better suited to realize large scale IMs and can take advantage of integrated CMOS

technology.

This thesis has successfully addressed the objectives listed in section 1.3. However, the possibility of utilizing oscillators in applications beyond their conventional use, e.g. for sensing or computing applications, is still a relatively unexplored field. Consequently, there is an immense amount of room to further explore the potential of utilizing emerging and established oscillators in these applications.



# References

- [1] G. E. Moore, “Cramming more components onto integrated circuits, reprinted from electronics, volume 38, number 8, april 19, 1965, pp.114 ff.,” *IEEE Solid-State Circuits Society Newsletter*, vol. 11, no. 3, pp. 33–35, 2006.
- [2] W. Arden, M. Brillouët, P. Cogez, M. Graef, B. Huizing, and R. Mahnkopf, “More-than-moore white paper,” *International Technology Roadmap for Semiconductors*, vol. 1, p. 14, 2010.
- [3] J. Shalf, “The future of computing beyond Moore ’ s Law,” *Philosophical Transactions Royal Society*, vol. 378, no. 20190061, pp. 1–14, 2020.
- [4] N. Singh, A. Agarwal, L. Bera, T. Liow, R. Yang, S. Rustagi, C. Tung, R. Kumar, G. Lo, N. Balasubramanian, and D.-L. Kwong, “High-performance fully depleted silicon nanowire (diameter /spl les/ 5 nm) gate-all-around cmos devices,” *IEEE Electron Device Letters*, vol. 27, no. 5, pp. 383–386, 2006.
- [5] “Samsung Begins Chip Production Using 3nm Process Technology With GAA Architecture” (2022, June 3) retrieved 30 november 2022 from <https://news.samsung.com/global/samsung-begins-chip-production-using-3nm-process-technology-with-gaa-architecture>,
- [6] S. Das, A. Chen, and M. Marinella, “Beyond cmos,” in *2021 IEEE International Roadmap for Devices and Systems Outbriefs*, pp. 01–129, 2021.
- [7] A. M. Ionescu and H. Riel, “Tunnel field-effect transistors as energy-efficient electronic switches,” *Nature*, vol. 479, no. 7373, pp. 329–337, 2011.
- [8] X. Wang, J. Zhou, J. Song, J. Liu, N. Xu, and Z. L. Wang, “Piezoelectric field effect transistor and nanoforce sensor based on a single ZnO nanowire,” *Nano Letters*, vol. 6, no. 12, pp. 2768–2772, 2006.
- [9] I. Žutić, J. Fabian, and S. Das Sarma, “Spintronics: Fundamentals and applications,” *Rev. Mod. Phys.*, vol. 76, pp. 323–410, Apr 2004.
- [10] D. B. Strukov, G. S. Snider, D. R. Stewart, and R. S. Williams, “The missing memristor found,” *Nature*, vol. 453, pp. 80–83, May 2008.

- [11] I. Vourkas and G. C. Sirakoulis, "Emerging memristor-based logic circuit design approaches: A review," *IEEE Circuits and Systems Magazine*, vol. 16, no. 3, pp. 15–30, 2016.
- [12] S. Ikegawa, F. B. Mancoff, J. Janesky, and S. Aggarwal, "Magnetoresistive Random Access Memory: Present and Future," *IEEE Transactions on Electron Devices*, vol. 67, no. 4, pp. 1407–1419, 2020.
- [13] G. Gielen, L. Hernandez-Corporales, and P. Rombouts, *Overview of VCO-ADC Architectures*. Cham: Springer International Publishing, 2022.
- [14] K. Kim and C. Yoo, "Time-domain operational amplifier with voltage-controlled oscillator and its application to active-rc analog filter," *IEEE Transactions on Circuits and Systems II: Express Briefs*, vol. 67, no. 3, pp. 415–419, 2020.
- [15] H. Osman and E. S.-S. Life, "A pvt-resilient, highly-linear fifth-order ring-oscillator-based filter," *IEEE Transactions on Circuits and Systems I: Regular Papers*, vol. 67, no. 12, pp. 4295–4308, 2020.
- [16] A. Sayal, S. S. T. Nibhanupudi, S. Fathima, and J. P. Kulkarni, "A 12.08- $\text{tops/w}$  all-digital time-domain cnn engine using bi-directional memory delay lines for energy efficient edge computing," *IEEE Journal of Solid-State Circuits*, vol. 55, no. 1, pp. 60–75, 2020.
- [17] G. Csaba and W. Porod, "Coupled oscillators for computing: A review and perspective," *Applied Physics Reviews*, vol. 7, no. 1, 2020.
- [18] A. Raychowdhury, A. Parihar, G. H. Smith, V. Narayanan, G. Csaba, M. Jerry, W. Porod, and S. Datta, "Computing with networks of oscillatory dynamical systems," *Proceedings of the IEEE*, vol. 107, no. 1, pp. 73–89, 2019.
- [19] D. E. Nikonov, P. Kurahashi, J. S. Ayers, H. Li, T. Kamgaing, G. C. Dogiamis, H.-J. Lee, Y. Fan, and I. A. Young, "Convolution inference via synchronization of a coupled cmos oscillator array," *IEEE Journal on Exploratory Solid-State Computational Devices and Circuits*, vol. 6, no. 2, pp. 170–176, 2020.
- [20] C. Delacour, S. Carapezzi, G. Boschetto, M. Abernot, T. Gil, and A. Todri-Sanial, "A mixed-signal oscillatory neural network for scalable analog computations in phase domain," tech. rep., Eindhoven University of Technology, Jan. 2023. preprint.
- [21] T. Wang and J. Roychowdhury, "OIM: Oscillator-Based Ising Machines for Solving Combinatorial Optimisation Problems," *Lecture Notes in Computer Science (including subseries Lecture Notes in Artificial Intelligence and Lecture Notes in Bioinformatics)*, vol. 11493 LNCS, pp. 232–256, 2019.

- [22] B. Razavi, *Design of Analog CMOS Integrated Circuits*. McGraw-Hill, first ed., 2001.
- [23] S. C. Bera, *Microwave Active Devices and Circuits for Communication*. Springer Singapore, 2019.
- [24] L. Atzori, A. Iera, and G. Morabito, “The Internet of Things: A survey,” *Computer Networks*, vol. 54, no. 15, pp. 2787–2805, 2010.
- [25] L. D. Xu, W. He, and S. Li, “Internet of things in industries: A survey,” *IEEE Transactions on Industrial Informatics*, vol. 10, no. 4, pp. 2233–2243, 2014.
- [26] H. S. Choi, S. Y. Kang, S. J. Cho, I. Y. Oh, M. Shin, H. Park, C. Jang, B. C. Min, S. I. Kim, S. Y. Park, and C. S. Park, “Spin nano-oscillator-based wireless communication,” *Scientific Reports*, vol. 4, pp. 1–7, 2014.
- [27] R. Sharma, P. Dürrenfeld, M. Ranjbar, R. K. Dumas, J. Åkerman, and P. K. Muduli, “Modulation Rate Study in a Spin-Torque Oscillator-Based Wireless Communication System,” *IEEE Transactions on Magnetics*, vol. 51, no. 11, pp. 2–5, 2015.
- [28] M. Kreisig, S. Witrock, F. Protze, R. Lebrun, K. J. Merazzo, M. C. Cyrille, R. Ferreira, P. Bortolotti, U. Ebels, V. Cros, and F. Ellinger, “Hybrid PLL system for spin torque oscillators utilizing custom ICs in 0.18  $\mu\text{m}$  BiCMOS,” *Midwest Symposium on Circuits and Systems*, vol. 2017-August, pp. 910–913, 2017.
- [29] A. Ruiz-Calaforra, A. Purbawati, T. Brächer, J. Hem, C. Murapaka, E. Jiménez, D. Mauri, A. Zeltser, J. A. Katine, M. C. Cyrille, L. D. Budapejbeanu, and U. Ebels, “Frequency shift keying by current modulation in a MTJ-based STNO with high data rate,” *Applied Physics Letters*, vol. 111, no. 8, 2017.
- [30] A. S. Jenkins, L. S. E. Alvarez, P. P. Freitas, and R. Ferreira, “Digital and analogue modulation and demodulation scheme using vortex-based spin torque nano-oscillators,” *Scientific Reports*, vol. 10, no. 1, pp. 1–7, 2020.
- [31] T. Chen, R. K. Dumas, A. Eklund, P. K. Muduli, A. Houshang, A. A. Awad, P. Dürrenfeld, B. G. Malm, A. Rusu, and J. Åkerman, “Spin-Torque and Spin-Hall Nano-Oscillators,” *Proceedings of the IEEE*, vol. 104, no. 10, pp. 1919–1945, 2016.
- [32] M. Bowles, “U.s. technological enthusiasm and british technological scepticism in the age of the analog brain,” *IEEE Annals of the History of Computing*, vol. 18, no. 4, pp. 5–15, 1996.

- [33] B. Ulmann, *Analog Computing*. Berlin, Boston: De Gruyter Oldenbourg, 2022.
- [34] W. Haensch, T. Gokmen, and R. Puri, “The next generation of deep learning hardware: Analog computing,” *Proceedings of the IEEE*, vol. 107, no. 1, pp. 108–122, 2019.
- [35] B. V. Benjamin, P. Gao, E. McQuinn, S. Choudhary, A. R. Chandrasekaran, J.-M. Bussat, R. Alvarez-Icaza, J. V. Arthur, P. A. Merolla, and K. Boahen, “Neurogrid: A mixed-analog-digital multichip system for large-scale neural simulations,” *Proceedings of the IEEE*, vol. 102, no. 5, pp. 699–716, 2014.
- [36] N. Mohseni, P. L. McMahon, and T. Byrnes, “Ising machines as hardware solvers of combinatorial optimization problems,” *Nature Reviews Physics*, vol. 4, no. 6, pp. 363–379, 2022.
- [37] T. Wang and J. Roychowdhury, “Phlogon: Phase-based logic using oscillatory nano-systems,” in *Unconventional Computation and Natural Computation* (O. H. Ibarra, L. Kari, and S. Kopecki, eds.), (Cham), pp. 353–366, Springer International Publishing, 2014.
- [38] G. Csaba and W. Porod, “Noise immunity of oscillatory computing devices,” *IEEE Journal on Exploratory Solid-State Computational Devices and Circuits*, vol. 6, no. 2, pp. 164–169, 2020.
- [39] V. Pourahmad, S. Manipatruni, D. Nikonov, I. Young, and E. Afshari, “Non-boolean Pattern Recognition Using Chains of Coupled CMOS Oscillators as Discriminant Circuits,” *IEEE Journal on Exploratory Solid-State Computational Devices and Circuits*, vol. 3, no. February, pp. 1–9, 2017.
- [40] R. W. Hözel and K. Krischer, “Pattern recognition with simple oscillating circuits,” *New Journal of Physics*, vol. 13, 2011.
- [41] E. Corti, B. Gotsmann, K. Moselund, I. Stolichnov, A. Ionescu, and S. Karg, “Resistive coupled vo2 oscillators for image recognition,” in *2018 IEEE International Conference on Rebooting Computing (ICRC)*, pp. 1–7, 2018.
- [42] D. Vodenicarevic, N. Locatelli, F. Abreu Araujo, J. Grollier, and D. Querlioz, “A Nanotechnology-Ready Computing Scheme based on a Weakly Coupled Oscillator Network,” *Scientific Reports*, vol. 7, no. November 2016, pp. 1–13, 2017.
- [43] M. Riou, J. Torrejon, B. Garitaine, F. Abreu Araujo, P. Bortolotti, V. Cros, S. Tsunegi, K. Yakushiji, A. Fukushima, H. Kubota, S. Yuasa, D. Querlioz, M. Stiles, and J. Grollier, “Temporal pattern recognition with delayed-feedback spin-torque nano-oscillators,” *Physical Review Applied*, vol. 12, p. 024049, Aug 2019.

- [44] T. Jackson, S. Pagliarini, and L. Pileggi, “An Oscillatory Neural Network with Programmable Resistive Synapses in 28 Nm CMOS,” *2018 IEEE International Conference on Rebooting Computing, ICRC 2018*, pp. 1–7, 2019.
- [45] E. Corti, J. A. Cornejo Jimenez, K. M. Niang, J. Robertson, K. E. Moselund, B. Gotsmann, A. M. Ionescu, and S. Karg, “Coupled VO<sub>2</sub> Oscillators Circuit as Analog First Layer Filter in Convolutional Neural Networks,” *Frontiers in Neuroscience*, vol. 15, no. February, pp. 1–12, 2021.
- [46] J. Shamsi, M. J. Avedillo, B. Linares-Barranco, and T. Serrano-Gotarredona, “Hardware Implementation of Differential Oscillatory Neural Networks Using VO<sub>2</sub>-Based Oscillators and Memristor-Bridge Circuits,” *Frontiers in Neuroscience*, vol. 15, no. July, pp. 1–14, 2021.
- [47] S. Carapezzi, G. Boschetto, C. Delacour, E. Corti, A. Plews, A. Nejim, S. Karg, and A. Todri-Sanial, “Advanced design methods from materials and devices to circuits for brain-inspired oscillatory neural networks for edge computing,” *IEEE Journal on Emerging and Selected Topics in Circuits and Systems*, vol. 11, no. 4, pp. 586–596, 2021.
- [48] D. Vodenicarevic, N. Locatelli, J. Grollier, and D. Querlioz, “Nano-oscillator-based classification with a machine learning-compatible architecture,” *Journal of Applied Physics*, vol. 124, no. 15, 2018.
- [49] A. Ross, N. Leroux, A. de Riz, D. Marković, D. Sanz-Hernández, J. Trastoy, P. Bortolotti, D. Querlioz, L. Martins, L. Benetti, M. S. Claro, P. Anacleto, A. Schulman, T. Taris, J.-B. Begueret, S. Saighi, A. S. Jenkins, R. Ferreira, A. F. Vincent, A. Mizrahi, and J. Grollier, “Multilayer spintronic neural networks with radio-frequency connections,” Nov 2022. preprint.
- [50] A. Mallick, M. K. Bashar, D. S. Truesdell, B. H. Calhoun, and N. Shukla, “Overcoming the accuracy vs. performance trade-off in oscillator ising machines,” in *2021 IEEE International Electron Devices Meeting (IEDM)*, pp. 40.2.1–40.2.4, 2021.
- [51] M. K. Bashar, A. Mallick, D. S. Truesdell, B. H. Calhoun, S. Joshi, and N. Shukla, “Experimental demonstration of a reconfigurable coupled oscillator platform to solve the max-cut problem,” *IEEE Journal on Exploratory Solid-State Computational Devices and Circuits*, vol. 6, no. 2, pp. 116–121, 2020.
- [52] S. Bonetti, P. Muduli, F. Mancoff, and J. Åkerman, “Spin torque oscillator frequency versus magnetic field angle: The prospect of operation beyond 65 GHz,” *Applied Physics Letters*, vol. 94, 03 2009. 102507.
- [53] A. Parihar, N. Shukla, S. Datta, and A. Raychowdhury, “Exploiting synchronization properties of correlated electron devices in a non-boolean computing fabric for template matching,” *IEEE Journal on Emerging and Selected Topics in Circuits and Systems*, vol. 4, no. 4, pp. 450–459, 2014.

- [54] R. Cheng, D. Xiao, and A. Brataas, “Terahertz antiferromagnetic spin hall nano-oscillator,” *Physical Review Letters*, vol. 116, p. 207603, May 2016.
- [55] N. Shukla, A. Parihar, E. Freeman, H. Paik, G. Stone, V. Narayanan, H. Wen, Z. Cai, V. Gopalan, R. Engel-Herbert, D. G. Schlom, A. Raychowdhury, and S. Datta, “Synchronized charge oscillations in correlated electron systems,” *Scientific Reports*, vol. 4, no. May, 2014.
- [56] D. Lee, J. Lee, S. Lee, C. Lee, S. Heo, and H. Hwang, “Nonvolatile Frequency-Programmable Oscillator With NbO<sub>2</sub>and Li-Based Electro-Chemical Random Access Memory for Coupled Oscillators-Based Temporal Pattern Recognition System,” *IEEE Electron Device Letters*, vol. 43, no. 7, pp. 1041–1044, 2022.
- [57] J. Slonczewski, “Current-driven excitation of magnetic multilayers,” *Journal of Magnetism and Magnetic Materials*, vol. 159, no. 1-2, pp. L1–L7, 1996.
- [58] L. Berger, “Emission of spin waves by a magnetic multilayer traversed by a current,” *Physical Review B*, vol. 54, pp. 9353–9358, Oct 1996.
- [59] M. Tsoi, A. G. M. Jansen, J. Bass, W.-C. Chiang, M. Seck, V. Tsoi, and P. Wyder, “Excitation of a magnetic multilayer by an electric current,” *Physical Review Letters*, vol. 80, pp. 4281–4284, May 1998.
- [60] E. B. Myers, D. C. Ralph, J. A. Katine, R. N. Louie, and R. A. Buhrman, “Current-induced switching of domains in magnetic multilayer devices,” *Science*, vol. 285, no. 5429, pp. 867–870, 1999.
- [61] S. I. Klselev, J. C. Sankey, I. N. Krivorotov, N. C. Emley, R. J. Schoelkopf, R. A. Buhrman, and D. C. Ralph, “Microwave oscillations of a nanomagnet driven by a spin-polarized current,” *Nature*, vol. 425, no. 6956, pp. 380–383, 2003.
- [62] B. Rodmacq, A. Schuhl, P. Gambardella, S. Bandiera, S. Auffret, M. V. Costache, P.-J. Zermatten, G. Gaudin, K. Garello, and I. M. Miron, “Perpendicular switching of a single ferromagnetic layer induced by in-plane current injection,” *Nature*, vol. 476, pp. 189–193, 2011.
- [63] J. A. Katine, F. J. Albert, R. A. Buhrman, E. B. Myers, and D. C. Ralph, “Current-driven magnetization reversals and spin-wave excitations in Co/Cu/Co pillars,” *Physical Review Letters*, vol. 84, no. 14, pp. 3149–3152, 2000.
- [64] H. Kubota, K. Yakushiji, A. Fukushima, S. Tamaru, M. Konoto, T. Nozaki, S. Ishibashi, T. Saruya, S. Yuasa, T. Taniguchi, H. Arai, and H. Imamura, “Spin-torque oscillator based on magnetic tunnel junction with a perpendicularly magnetized free layer and in-plane magnetized polarizer,” *Applied Physics Express*, vol. 6, p. 103003, sep 2013.

- [65] W. H. Rippard, M. R. Pufall, S. Kaka, S. E. Russek, and T. J. Silva, “Direct-current induced dynamics in  $\text{co}_{90}\text{fe}_{10}/\text{ni}_{80}\text{fe}_{20}$  point contacts,” *Physical Review Letters*, vol. 92, p. 027201, Jan 2004.
- [66] H. Maehara, H. Kubota, Y. Suzuki, T. Seki, K. Nishimura, Y. Nagamine, K. Tsunekawa, A. Fukushima, A. M. Deac, K. Ando, and S. Yuasa, “Large emission power over 2  $\mu\text{w}$  with high q factor obtained from nanocontact magnetic-tunnel-junction-based spin torque oscillator,” *Applied Physics Express*, vol. 6, p. 113005, oct 2013.
- [67] L. Liu, C. F. Pai, D. C. Ralph, and R. A. Buhrman, “Magnetic oscillations driven by the spin hall effect in 3-terminal magnetic tunnel junction devices,” *Physical Review Letters*, vol. 109, no. 18, pp. 1–5, 2012.
- [68] V. E. Demidov, S. Urazhdin, A. Zholud, A. V. Sadovnikov, and S. O. Demokritov, “Nanoconstriction-based spin-Hall nano-oscillator,” *Applied Physics Letters*, vol. 105, no. 17, 2014.
- [69] V. E. Demidov, S. Urazhdin, H. Ulrichs, V. Tiberkevich, A. Slavin, D. Baither, G. Schmitz, and S. O. Demokritov, “Magnetic nano-oscillator driven by pure spin current,” *Nature Materials*, vol. 11, no. 12, pp. 1028–1031, 2012.
- [70] J. E. Hirsch, “Spin Hall Effect,” *Physical Review Letters*, vol. 83, no. 9, pp. 1834–1837, 1999.
- [71] A. Hoffmann, “Spin Hall Effects in Metals,” *IEEE Trans. Magn.*, vol. 49, no. 10, pp. 5172–5193, 2013.
- [72] W. Thomson, “Xix. on the electro-dynamic qualities of metals:—effects of magnetization on the electric conductivity of nickel and of iron,” *Proceedings of the Royal Society of London*, vol. 8, pp. 546–550, 1857.
- [73] J. Lenz and A. S. Edelstein, “Magnetic sensors and their applications,” *IEEE Sensors Journal*, vol. 6, no. 3, pp. 631–649, 2006.
- [74] M. Zahedinejad, H. Mazraati, H. Fulara, J. Yue, S. Jiang, A. A. Awad, and J. Åkerman, “CMOS compatible W/CoFeB/MgO spin Hall nano-oscillators with wide frequency tunability,” *Applied Physics Letters*, vol. 112, no. 13, pp. 1–5, 2018.
- [75] M. N. Baibich, J. M. Broto, A. Fert, F. N. Van Dau, F. Petroff, P. Etienne, G. Creuzet, A. Friederich, and J. Chazelas, “Giant magnetoresistance of (001)fe/(001)cr magnetic superlattices,” *Physical Review Letters*, vol. 61, pp. 2472–2475, Nov 1988.
- [76] G. Binasch, P. Grünberg, F. Saurenbach, and W. Zinn, “Enhanced magnetoresistance in layered magnetic structures with antiferromagnetic interlayer exchange,” *Physical Review B*, vol. 39, pp. 4828–4830, Mar 1989.

- [77] J. C. Slonczewski, “Conductance and exchange coupling of two ferromagnets separated by a tunneling barrier,” *Physical Review B*, vol. 39, no. 10, pp. 6995–7002, 1989.
- [78] J. G. J. Zhu and C. Park, “Magnetic tunnel junctions,” *Materials Today*, vol. 9, no. 11, pp. 36–45, 2006.
- [79] S. S. P. Parkin, C. Kaiser, A. Panchula, P. M. Rice, B. Hughes, M. Samant, and S.-h. Yang, “Giant tunnelling magnetoresistance at room temperature with MgO (100) tunnel barriers,” *Nature Materials*, vol. 3, no. December, pp. 2–7, 2004.
- [80] S. Ikeda, J. Hayakawa, Y. Ashizawa, Y. M. Lee, K. Miura, H. Hasegawa, M. Tsunoda, F. Matsukura, and H. Ohno, “Tunnel magnetoresistance of 604% at 300 K by suppression of Ta diffusion in CoFeB/MgO/CoFeB pseudo-spin-valves annealed at high temperature,” *Applied Physics Letters*, vol. 93, no. 8, pp. 1–4, 2008.
- [81] A. Slavin and V. Tiberkevich, “Nonlinear auto-oscillator theory of microwave generation by spin-polarized current,” *IEEE Transactions on Magnetics*, vol. 45, no. 4, pp. 1875–1918, 2009.
- [82] G. V. Karakashian, L. L. Lutz-Nagey, and R. Anderson, *Magnetization Oscillation and Waves*. No. 1, CRC Press, 1987.
- [83] L. Berger, “Emission of spin waves by a magnetic multilayer traversed by a current,” *Physical Review B*, vol. 54, pp. 9353–9358, Oct 1996.
- [84] T. Chen, A. Eklund, E. Iacobca, S. Rodriguez, B. G. Malm, J. Åkerman, and A. Rusu, “Comprehensive and macrospin-based magnetic tunnel junction spin torque oscillator model-Part I: Analytical Model of the MTJ STO,” *IEEE Transactions on Electron Devices*, vol. 62, no. 3, pp. 1037–1051, 2015.
- [85] E. H. Hall, “On a New Action of the Magnet on Electric Currents,” *American Journal of Mathematics*, vol. 2, no. 3, p. 287, 1879.
- [86] M. Zahedinejad, A. A. Awad, S. Muralidhar, R. Khymyn, H. Fulara, H. Mazraati, M. Dvornik, and J. Åkerman, “Two-dimensional mutually synchronized spin Hall nano-oscillator arrays for neuromorphic computing,” *Nature Nanotechnology*, vol. 15, no. 1, pp. 47–52, 2020.
- [87] S. Tsunegi, K. Yakushiji, A. Fukushima, S. Yuasa, and H. Kubota, “Microwave emission power exceeding 10  $\mu$  W in spin torque vortex oscillator,” *Applied Physics Letters*, vol. 109, no. 25, 2016.
- [88] P. Talatchian, *Bio-inspired computing leveraging the synchronization of magnetic nano-oscillators*. Theses, Université Paris Saclay (COmUE), Jan. 2019.

- [89] P. Dürrenfeld, A. A. Awad, A. Houshang, R. K. Dumas, and J. Åkerman, “A 20 nm spin Hall nano-oscillator,” *Nanoscale*, vol. 9, no. 3, pp. 1285–1291, 2017.
- [90] M. Tarequzzaman, T. Böhnert, M. Decker, J. D. Costa, J. Borme, B. Lacoste, E. Paz, A. S. Jenkins, S. Serrano-Guisan, C. H. Back, R. Ferreira, and P. P. Freitas, “Spin torque nano-oscillator driven by combined spin injection from tunneling and spin Hall current,” *Communications Physics*, vol. 2, no. 1, pp. 1–8, 2019.
- [91] Z. Zeng, G. Finocchio, B. Zhang, P. K. Amiri, J. A. Katine, I. N. Krivorotov, Y. Huai, J. Langer, B. Azzeroni, K. L. Wang, and H. Jiang, “Ultralow-current-density and bias-field-free spin-transfer nano-oscillator,” *Scientific Reports*, vol. 3, pp. 1–5, 2013.
- [92] W. Zhang, Y. Zhang, B. Jiang, B. Fang, H. Zhong, H. Li, Z. M. Zeng, S. S. Yan, G. Han, G. Liu, S. Yu, and S. Kang, “Bias-field-free high frequency microwave emission of spin-transfer nano-oscillator with magnetizations all in-plane,” *Applied Physics Letters*, vol. 118, no. 1, 2021.
- [93] S. Jiang, S. Chung, Q. T. Le, P. K. J. Wong, W. Zhang, and J. Åkerman, “Field-Free High-Frequency Exchange-Spring Spin-Torque Nano-Oscillators,” *Nano Letters*, 2022.
- [94] N. Locatelli, A. Hamadeh, F. Abreu Araujo, A. D. Belanovsky, P. N. Skirdkov, R. Lebrun, V. V. Naletov, K. A. Zvezdin, M. Muñoz, J. Grollier, O. Klein, V. Cros, and G. De Loubens, “Efficient Synchronization of Dipolarly Coupled Vortex-Based Spin Transfer Nano-Oscillators,” *Scientific Reports*, vol. 5, pp. 1–10, 2015.
- [95] R. Lebrun, S. Tsunegi, P. Bortolotti, H. Kubota, A. S. Jenkins, M. Romera, K. Yakushiji, A. Fukushima, J. Grollier, S. Yuasa, and V. Cros, “Mutual synchronization of spin torque nano-oscillators through a long-range and tunable electrical coupling scheme,” *Nature Communications*, vol. 8, no. May, 2017.
- [96] A. A. Awad, P. Dürrenfeld, A. Houshang, M. Dvornik, E. Iacocca, R. K. Dumas, and J. Åkerman, “Long-range mutual synchronization of spin Hall nano-oscillators,” *Nature Physics*, vol. 13, no. 3, pp. 292–299, 2017.
- [97] S. Tsunegi, T. Taniguchi, R. Lebrun, K. Yakushiji, V. Cros, J. Grollier, A. Fukushima, S. Yuasa, and H. Kubota, “Scaling up electrically synchronized spin torque oscillator networks,” *Scientific Reports*, vol. 8, no. 1, pp. 2–8, 2018.
- [98] S. Tamaru, H. Kubota, K. Yakushiji, S. Yuasa, and A. Fukushima, “Extremely Coherent Microwave Emission from Spin Torque Oscillator Stabilized by Phase Locked Loop,” *Scientific Reports*, vol. 5, no. November, pp. 1–6, 2015.

- [99] N. Leroux, A. Mizrahi, D. Marković, D. Sanz-Hernández, J. Trastoy, P. Bortolotti, L. Martins, A. Jenkins, R. Ferreira, and J. Grollier, “Hardware realization of the multiply and accumulate operation on radio-frequency signals with magnetic tunnel junctions,” *Neuromorphic Computing and Engineering*, vol. 1, no. 1, p. 011001, 2021.
- [100] N. Leroux, A. D. Riz, D. Sanz-Hernández, D. Marković, A. Mizrahi, and J. Grollier, “Convolutional neural networks with radio-frequency spintronic nano-devices,” *Neuromorphic Computing and Engineering*, vol. 2, p. 034002, jul 2022.
- [101] J. Torrejon, M. Riou, F. A. Araujo, S. Tsunegi, G. Khalsa, D. Querlioz, P. Bortolotti, V. Cros, K. Yakushiji, A. Fukushima, H. Kubota, S. Yuasa, M. D. Stiles, and J. Grollier, “Neuromorphic computing with nanoscale spintronic oscillators,” *Nature*, vol. 547, no. 7664, pp. 428–431, 2017.
- [102] M. Romera, P. Talatchian, S. Tsunegi, F. Abreu Araujo, V. Cros, P. Bortolotti, J. Trastoy, K. Yakushiji, A. Fukushima, H. Kubota, S. Yuasa, M. Ernoult, D. Vodenicarevic, T. Hirtzlin, N. Locatelli, D. Querlioz, and J. Grollier, “Vowel recognition with four coupled spin-torque nano-oscillators,” *Nature*, vol. 563, no. 7730, pp. 230–234, 2018.
- [103] D. Marković, N. Leroux, M. Riou, F. Abreu Araujo, J. Torrejon, D. Querlioz, A. Fukushima, S. Yuasa, J. Trastoy, P. Bortolotti, and J. Grollier, “Reservoir computing with the frequency, phase, and amplitude of spin-torque nano-oscillators,” *Applied Physics Letters*, vol. 114, no. 1, p. 012409, 2019.
- [104] M. Romera, P. Talatchian, S. Tsunegi, K. Yakushiji, A. Fukushima, H. Kubota, S. Yuasa, V. Cros, P. Bortolotti, M. Ernoult, D. Querlioz, and J. Grollier, “Binding events through the mutual synchronization of spintronic nano-neurons,” *Nature Communications*, vol. 13, no. 1, pp. 1–7, 2022.
- [105] R. Fiorelli, E. Peralás, R. Méndez-Romero, M. Rajabali, A. Kumar, M. Zahedinejad, J. Åkerman, F. Moradi, T. Serrano-Gotarredona, and B. Linares-Barranco, “CMOS Front End for Interfacing Spin-Hall Nano-Oscillators for Neuromorphic Computing in the GHz Range,” *Electronics (Switzerland)*, vol. 12, no. 1, pp. 1–18, 2023.
- [106] D. I. Albertsson, M. Zahedinejad, A. Houshang, R. Khymyn, J. Åkerman, and A. Rusu, “Ultrafast ising machines using spin torque nano-oscillators,” *Applied Physics Letters*, vol. 118, no. 11, p. 112404, 2021.
- [107] B. C. McGoldrick, J. Z. Sun, and L. Liu, “Ising machine based on electrically coupled spin hall nano-oscillators,” *Physical Review Applied*, vol. 17, p. 014006, Jan 2022.

- [108] A. Houshang, M. Zahedinejad, S. Muralidhar, R. Khymyn, M. Rajabali, H. Fulara, A. A. Awad, J. Åkerman, J. Chęciński, and M. Dvornik, "Phase-Binarized Spin Hall Nano-Oscillator Arrays: Towards Spin Hall Ising Machines," *Physical Review Applied*, vol. 17, no. 1, pp. 1–13, 2022.
- [109] M. Takagishi, N. Narita, Y. Nakagawa, T. Nagasawa, R. Osamura, T. Maeda, and K. Yamada, "Microwave assisted magnetic Recording: Physics and application to hard disk drives," *Journal of Magnetism and Magnetic Materials*, vol. 563, no. April, p. 169859, 2022.
- [110] P. M. Braganca, B. A. Gurney, B. A. Wilson, J. A. Katine, S. Maat, and J. R. Childress, "Nanoscale magnetic field detection using a spin torque oscillator," *Nanotechnology*, vol. 21, no. 23, 2010.
- [111] T. Chen, S. Rodriguez, J. Åkerman, and A. Rusu, "An inductorless wideband Balun-LNA for spin torque oscillator-based field sensing," *2014 21st IEEE International Conference on Electronics, Circuits and Systems, ICECS 2014*, pp. 36–39, 2015.
- [112] B. Ramaswamy, J. M. Algarin, I. N. Weinberg, Y. J. Chen, I. N. Krivorotov, J. A. Katine, B. Shapiro, and E. Waks, "Wireless current sensing by near field induction from a spin transfer torque nano-oscillator," *Applied Physics Letters*, vol. 108, no. 24, 2016.
- [113] R. Saha, K. Wu, D. Su, and J. P. Wang, "Spin current nano-oscillator (SCNO) as a potential frequency-based, ultra-sensitive magnetic biosensor: A simulation study," *Nanotechnology*, vol. 31, no. 37, 2020.
- [114] A. Kumar, M. Rajabali, V. H. González, M. Zahedinejad, A. Houshang, and J. Åkerman, "Fabrication of voltage-gated spin Hall nano-oscillators," *Nanoscale*, vol. 14, no. 4, pp. 1432–1439, 2022.
- [115] V. H. González, R. Khymyn, H. Fulara, A. A. Awad, and J. Åkerman, "Voltage control of frequency, effective damping, and threshold current in nano-constriction-based spin Hall nano-oscillators," *Applied Physics Letters*, vol. 121, no. 25, 2022.
- [116] M. Zahedinejad, H. Fulara, R. Khymyn, A. Houshang, M. Dvornik, S. Fukami, S. Kanai, H. Ohno, and J. Åkerman, "Memristive control of mutual spin Hall nano-oscillator synchronization for neuromorphic computing," *Nature Materials*, vol. 21, no. 1, pp. 81–87, 2022.
- [117] T. Taniguchi, "Synchronization of Spin Torque Oscillators through Spin Hall Magnetoresistance," *IEEE Transactions on Magnetics*, vol. 53, no. 11, pp. 1–7, 2017.

- [118] M. Carpentieri, S. Vergura, R. Tomasello, A. Giordano, V. Puliafito, and G. Siracusano, “Micromagnetic modelling of synchronized three terminal magnetic tunnel junctions,” in *2015 IEEE 1st International Forum on Research and Technologies for Society and Industry Leveraging a better tomorrow (RTSI)*, pp. 238–242, 2015.
- [119] R. Tomasello, M. Carpentieri, and G. Finocchio, “Dynamical properties of three terminal magnetic tunnel junctions: Spintronics meets spin-orbitronics,” *Applied Physics Letters*, vol. 103, no. 25, 2013.
- [120] T. Chen, A. Eklund, E. Iacocca, S. Rodriguez, B. G. Malm, J. Åkerman, and A. Rusu, “Comprehensive and macrospin-based magnetic tunnel junction spin torque oscillator model-Part II: Verilog-A model implementation,” *IEEE Transactions on Electron Devices*, vol. 62, no. 3, pp. 1045–1051, 2015.
- [121] P. K. Muduli, O. G. Heinonen, and J. Åkerman, “Bias dependence of perpendicular spin torque and of free- and fixed-layer eigenmodes in MgO-based nanopillars,” *Physical Review B - Condensed Matter and Materials Physics*, vol. 83, no. 18, pp. 1–10, 2011.
- [122] F.-f. Li, Z.-z. Li, M.-w. Xiao, J. Du, W. Xu, A. Hu, and J. Q. Xiao, “Bias dependent tunneling in ferromagnetic junctions and inversion of the tunneling magnetoresistance from a quantum mechanical point of view,” *Journal of Applied Physics*, vol. 95, pp. 7243–7245, 05 2004.
- [123] M. Madec, J.-B. Kammerer, and L. Hébrard, “Compact modeling of a magnetic tunnel junction—part ii: Tunneling current model,” *IEEE Transactions on Electron Devices*, vol. 57, no. 6, pp. 1416–1424, 2010.
- [124] A. M. Deac, A. Fukushima, H. Kubota, H. Maehara, Y. Suzuki, S. Yuasa, Y. Nagamine, K. Tsunekawa, D. D. Djayaprawira, and N. Watanabe, “Bias-driven high-power microwave emission from MgO-based tunnel magnetoresistance devices,” *Nature Physics*, vol. 4, no. 10, pp. 803–809, 2008.
- [125] N. M. Blachman and S. H. Mousavinezhad, “Trigonometric approximations for bessel functions,” *IEEE Transactions on Aerospace and Electronic Systems*, vol. AES-22, no. 1, pp. 2–7, 1986.
- [126] A. Eklund, S. Bonetti, S. R. Sani, S. Majid Mohseni, J. Persson, S. Chung, S. Amir Hossein Banuazizi, E. Iacocca, M. Östling, J. Åkerman, and B. Gunnar Malm, “Dependence of the colored frequency noise in spin torque oscillators on current and magnetic field,” *Applied Physics Letters*, vol. 104, no. 9, 2014.
- [127] S. Wittrock, P. Talatchian, S. Tsunegi, D. Crété, K. Yakushiji, P. Bortolotti, U. Ebels, A. Fukushima, H. Kubota, S. Yuasa, J. Grollier, G. Cibiel, S. Galloiu, E. Rubiola, and V. Cros, “Influence of flicker noise and nonlinearity on

- the frequency spectrum of spin torque nano-oscillators,” *Scientific Reports*, vol. 10, no. 1, pp. 1–10, 2020.
- [128] M. Quinsat, D. Gusakova, J. F. Sierra, J. P. Michel, D. Houssameddine, B. Delaet, M. C. Cyrille, U. Ebels, B. Dieny, L. D. Buda-Prejbeanu, J. A. Katine, D. Mauri, A. Zeltser, M. Prigent, J. C. Nallatamby, and R. Sommet, “Amplitude and phase noise of magnetic tunnel junction oscillators,” *Applied Physics Letters*, vol. 97, no. 18, pp. 5–8, 2010.
- [129] P. K. Muduli, O. G. Heinonen, and J. Kerman, “Intrinsic frequency doubling in a magnetic tunnel junction-based spin torque oscillator,” *Journal of Applied Physics*, vol. 110, no. 7, pp. 108–111, 2011.
- [130] C. Reig and M.-D. Cubells-Beltrán, *Giant (GMR) and Tunnel (TMR) Magnetoresistance Sensors: From Phenomena to Applications*, pp. 35–64. Taylor & Francis Group, England, 10 2017.
- [131] U. Ausserlechner, “The optimum layout for giant magneto-resistive angle sensors,” *IEEE Sensors Journal*, vol. 10, no. 10, pp. 1571–1582, 2010.
- [132] S.-T. Wu, J.-Y. Chen, and S.-H. Wu, “A rotary encoder with an eccentrically mounted ring magnet,” *IEEE Transactions on Instrumentation and Measurement*, vol. 63, no. 8, pp. 1907–1915, 2014.
- [133] N. Zhang, L. Peng, Y. He, and C. Ye, “Flexible probe with array tunneling magnetoresistance sensors for curved structure inspection,” *IEEE Transactions on Instrumentation and Measurement*, vol. 71, pp. 1–9, 2022.
- [134] C. Zheng, K. Zhu, S. C. De Freitas, J. Y. Chang, J. E. Davies, P. Eames, P. P. Freitas, O. Kazakova, C. G. Kim, C. W. Leung, S. H. Liou, A. Ognev, S. N. Piramanayagam, P. Ripka, A. Samardak, K. H. Shin, S. Y. Tong, M. J. Tung, S. X. Wang, S. Xue, X. Yin, and P. W. Pong, “Magnetoresistive Sensor Development Roadmap (Non-Recording Applications),” *IEEE Transactions on Magnetics*, vol. 55, no. 4, 2019.
- [135] H. Chiriac, M. Tibu, A.-E. Moga, and D. D. Herea, “Magnetic gmi sensor for detection of biomolecules,” *Journal of Magnetism and Magnetic Materials*, vol. 293, no. 1, pp. 671–676, 2005. Proceedings of the Fifth International Conference on Scientific and Clinical Applications of Magnetic Carriers.
- [136] C. Dey, P. Yari, and K. Wu, “Recent advances in magnetoresistance biosensors : a short review,” *Nano Futures*, vol. 7, 2023.
- [137] P. Ripka and M. Janosek, “Advances in magnetic field sensors,” *IEEE Sensors Journal*, vol. 10, no. 6, pp. 1108–1116, 2010.

- [138] M. A. Khan, J. Sun, B. Li, A. Przybysz, and J. Kosel, "Magnetic sensors-A review and recent technologies," *Engineering Research Express*, vol. 3, no. 2, 2021.
- [139] K. Mizushima, K. Kudo, T. Nagasawa, and R. Sato, "Signal-to-noise ratios in high-signal-transfer-rate read heads composed of spin-torque oscillators," *Journal of Applied Physics*, vol. 107, no. 6, 2010.
- [140] R. Sato, K. Kudo, T. Nagasawa, H. Suto, and K. Mizushima, "Simulations and experiments toward high-data-transfer-rate readers composed of a spin-torque oscillator," *IEEE Transactions on Magnetics*, vol. 48, no. 5, pp. 1758–1764, 2012.
- [141] G. Albuquerque, S. Hernandez, M. T. Kief, D. Mauri, and L. Wang, "HDD Reader Technology Roadmap to an Areal Density of 4 Tbpsi and Beyond," *IEEE Transactions on Magnetics*, vol. 58, no. 2, 2022.
- [142] H. Xia, Q. Zheng, C. Mu, C. Song, C. Jin, Q. Liu, and J. Wang, "Micromagnetic simulation for detection of magnetic nanobeads by spin torque oscillator," *Journal of Magnetism and Magnetic Materials*, vol. 432, pp. 387–390, 2017.
- [143] Y. Xie, H. F. H. Cheung, and G. D. Fuchs, "Nanoscale magnetic field sensing with spin-hall nano-oscillator devices," March 2023. preprint.
- [144] O. Boulle, V. Cros, J. Grollier, L. G. Pereira, C. Deranlot, F. Petroff, G. Faini, J. Barnaś, and A. Fert, "Shaped angular dependence of the spin-transfer torque and microwave generation without magnetic field," *Nature Physics*, vol. 3, pp. 492–497, Jul 2007.
- [145] Y. Zhang and Z. Zhu, "Recent Advances and Trends in Voltage-Time Domain Hybrid ADCs," *IEEE Transactions on Circuits and Systems II: Express Briefs*, vol. 69, no. 6, pp. 2575–2580, 2022.
- [146] P. Harpe, "Successive approximation analog-to-digital converters: Improving power efficiency and conversion speed," *IEEE Solid-State Circuits Magazine*, vol. 8, no. 4, pp. 64–73, 2016.
- [147] M. Baert and W. Dehaene, "A 5-gs/s 7.2-enob time-interleaved vco-based adc achieving 30.5 fJ/cs," *IEEE Journal of Solid-State Circuits*, vol. 55, no. 6, pp. 1577–1587, 2020.
- [148] Chithra and N. Krishnapura, "A flexible 18-channel multi-hit time-to-digital converter for trigger-based data acquisition systems," *IEEE Transactions on Circuits and Systems I: Regular Papers*, vol. 67, no. 6, pp. 1892–1901, 2020.

- [149] Jaewook Kim, Tae-Kwang Jang, Young-Gyu Yoon, and SeongHwan Cho, “Analysis and Design of Voltage-Controlled Oscillator Based Analog-to-Digital Converter,” *IEEE Transactions on Circuits and Systems I: Regular Papers*, vol. 57, no. 1, pp. 18–30, 2010.
- [150] E. Sacco, J. Vergauwen, and G. Gielen, “From open-loop to closed-loop single-vco-based sensor-to-digital converter architectures: theoretical analysis and comparison,” in *2019 IEEE 8th International Workshop on Advances in Sensors and Interfaces (IWASI)*, pp. 29–34, 2019.
- [151] M. D. Ronny Frevert, Joachim Haase, Roland Jancke, Uwe Knöchel, Peter Schwarz, Ralf Kakerow, *Modeling and Simulation for RF System Design*, vol. 1. Springer New York, NY, 2006.
- [152] T. Chen, P. Dürrenfeld, S. Rodriguez, J. Åkerman, and A. Rusu, “A Highly Tunable Microwave Oscillator Based on MTJ STO Technology,” *Microwave And Optical Technology Letters*, vol. 56, no. 9, pp. 2092–2095, 2014.
- [153] A. Lucas, “Ising formulations of many NP problems,” *Frontiers in Physics*, vol. 2, no. February, pp. 1–14, 2014.
- [154] D.-z. Du, P. M. Pardalos, X. Hu, and W. Wu, *Introduction to Combinatorial Optimization*. Springer Cham, 1 ed., 2023.
- [155] A. Arigliano, G. Ghiani, A. Grieco, E. Guerriero, and I. Plana, “Time-dependent asymmetric traveling salesman problem with time windows: Properties and an exact algorithm,” *Discrete Applied Mathematics*, vol. 261, pp. 28–39, 2019. GO X Meeting, Rigi Kaltbad (CH), July 10–14, 2016.
- [156] S. Kirkpatrick, C. D. Gelatt, and M. P. Vecchi, “Optimization by simulated annealing,” *Science*, vol. 220, no. 4598, pp. 671–680, 1983.
- [157] E. G. Rieffel, D. Venturelli, B. O’Gorman, M. B. Do, E. M. Prystay, and V. N. Smelyanskiy, “A case study in programming a quantum annealer for hard operational planning problems,” *Quantum Inf Process*, vol. 14, pp. 1–36, Jan. 2015.
- [158] A. Guillaume, E. Y. Goh, M. D. Johnston, B. D. Wilson, A. Ramanan, F. Tibile, and B. Lackey, “Deep Space Network scheduling using Quantum Annealing,” *IEEE Transactions on Quantum Engineering*, vol. 3, no. January, pp. 1–16, 2022.
- [159] M. Benedetti, J. Realpe-Gómez, R. Biswas, and A. Perdomo-Ortiz, “Quantum-assisted learning of hardware-embedded probabilistic graphical models,” *Physical Review X*, vol. 7, p. 041052, Nov. 2017.

- [160] R. Y. Li, R. Di Felice, R. Rohs, and D. A. Lidar, “Quantum annealing versus classical machine learning applied to a simplified computational biology problem,” *npj Quantum Inf*, vol. 4, Feb. 2018.
- [161] M. Hernandez and M. Aramon, “Enhancing quantum annealing performance for the molecular similarity problem,” *Quantum Inf Process*, vol. 16, Apr. 2017.
- [162] R. Babbush, P. J. Love, and A. Aspuru-Guzik, “Adiabatic quantum simulation of quantum chemistry,” *Sci Rep*, vol. 4, Oct. 2014.
- [163] E. Ising, “Contribution to the Theory of Ferromagnetism,” *Z. Phys.*, vol. 31, pp. 253–258, 1925.
- [164] F. Barahona, “On the computational complexity of ising spin glass models,” *Journal of Physics A: Mathematical and General*, vol. 15, no. 10, pp. 3241–3253, 1982.
- [165] D. J. Earl and M. W. Deem, “Parallel tempering: Theory, applications, and new perspectives,” *Phys. Chem. Chem. Phys.*, vol. 7, pp. 3910–3916, 2005.
- [166] W. Wang, J. Machta, and H. G. Katzgraber, “Comparing monte carlo methods for finding ground states of ising spin glasses: Population annealing, simulated annealing, and parallel tempering,” *Physical Review E*, vol. 92, p. 013303, Jul 2015.
- [167] F. Barahona, M. Grötschel, M. Jünger, and G. Reinelt, “An application of combinatorial optimization to statistical physics and circuit layout design,” *Operations Research*, vol. 36, no. 3, pp. 493–513, 1988.
- [168] K. Chang and D.-C. Du, “Efficient algorithms for layer assignment problem,” *IEEE Transactions on Computer-Aided Design of Integrated Circuits and Systems*, vol. 6, no. 1, pp. 67–78, 1987.
- [169] J. Wang, T. Jebara, and S. F. Chang, “Semi-supervised learning using greedy max-cut,” *Journal of Machine Learning Research*, vol. 14, no. 1, pp. 771–800, 2013.
- [170] J. Poland and T. Zeugmann, “Clustering pairwise distances with missing data: Maximum cuts versus normalized cuts,” in *Discovery Science* (L. Todorovski, N. Lavrač, and K. P. Jantke, eds.), (Berlin, Heidelberg), pp. 197–208, Springer Berlin Heidelberg, 2006.
- [171] B. Apolloni, C. Carvalho, and D. de Falco, “Quantum stochastic optimization,” *Stochastic Processes and their Applications*, vol. 33, no. 2, pp. 233–244, 1989.

- [172] M. W. Johnson, M. H. Amin, S. Gildert, T. Lanting, F. Hamze, N. Dickson, R. Harris, A. J. Berkley, J. Johansson, P. Bunyk, E. M. Chapple, C. Enderud, J. P. Hilton, K. Karimi, E. Ladizinsky, N. Ladizinsky, T. Oh, I. Perminov, C. Rich, M. C. Thom, E. Tolkacheva, C. J. Truncik, S. Uchaikin, J. Wang, B. Wilson, and G. Rose, "Quantum annealing with manufactured spins," *Nature*, vol. 473, no. 7346, pp. 194–198, 2011.
- [173] P. Hauke, H. G. Katzgraber, W. Lechner, H. Nishimori, and W. D. Oliver, "Perspectives of quantum annealing: Methods and implementations," *Reports on Progress in Physics*, vol. 83, no. 5, 2020.
- [174] P. I. Bunyk, E. M. Hoskinson, M. W. Johnson, E. Tolkacheva, F. Altomare, A. J. Berkley, R. Harris, J. P. Hilton, T. Lanting, A. J. Przybysz, and J. Whittaker, "Architectural Considerations in the Design of a Superconducting Quantum Annealing Processor," *IEEE Transactions on Applied Superconductivity*, vol. 24, no. 4, pp. 1–10, 2014.
- [175] R. Harris, T. Lanting, A. J. Berkley, J. Johansson, M. W. Johnson, P. Bunyk, E. Ladizinsky, N. Ladizinsky, T. Oh, and S. Han, "Compound josephson-junction coupler for flux qubits with minimal crosstalk," *Physical Review B*, vol. 80, p. 052506, Aug 2009.
- [176] T. Albash and D. A. Lidar, "Adiabatic quantum computation," *Reviews of Modern Physics*, vol. 90, no. 1, 2018.
- [177] D-Wave, "The Most Connected and Powerful Quantum Computer Built for Business." <https://www.dwavesys.com/solutions-and-products/systems/>, 2023. [Online; accessed 8-March-2023].
- [178] A. Marandi, Z. Wang, K. Takata, R. L. Byer, and Y. Yamamoto, "Network of time-multiplexed optical parametric oscillators as a coherent Ising machine," *Nature Photonics*, vol. 8, no. 12, pp. 937–942, 2014.
- [179] T. Honjo, T. Sonobe, K. Inaba, T. Inagaki, T. Ikuta, Y. Yamada, T. Kazama, K. Enbusu, T. Umeki, R. Kasahara, K. I. Kawarabayashi, and H. Takesue, "100,000-spin coherent Ising machine," *Science Advances*, vol. 7, no. 40, 2021.
- [180] Y. Inui, M. D. S. H. Gunathilaka, S. Kako, T. Aonishi, and Y. Yamamoto, "Control of amplitude homogeneity in coherent Ising machines with artificial Zeeman terms," *Communications Physics*, vol. 5, no. 1, pp. 1–8, 2022.
- [181] Q. Cen, H. Ding, T. Hao, S. Guan, Z. Qin, J. Lyu, W. Li, N. Zhu, K. Xu, Y. Dai, and M. Li, "Large-scale coherent Ising machine based on optoelectronic parametric oscillator," *Light: Science and Applications*, vol. 11, no. 1, pp. 1–10, 2022.

- [182] C. Y. Takashi Takemoto, Kasho Yamamoto, M. Hayashi, H. S. Masafumi Tada, and M. Y. , Mayumi Mashimo, “A 144Kb Annealing System Composed of  $9 \times 16$ Kb Annealing Processor Chips with Scalable Chip-to-Chip Connections for,” *2021 IEEE International Solid-State Circuits Conference (ISSCC)*, vol. 64, pp. 64–65, 2021.
- [183] K. Yamamoto, T. Takemoto, C. Yoshimura, M. Mashimo, and M. Yamaoka, “A 1.3-Mbit Annealing System Composed of Fully-Synchronized 9-board  $\times$  9-chip  $\times$  16-kbit Annealing Processor Chips for Large-Scale Combinatorial Optimization Problems,” *Proceedings - A-SSCC 2021: IEEE Asian Solid-State Circuits Conference*, pp. 2021–2023, 2021.
- [184] M. Yamaoka, C. Yoshimura, M. Hayashi, T. Okuyama, H. Aoki, and H. Mizuno, “A 20k-spin Ising chip to solve combinatorial optimization problems with CMOS annealing,” *IEEE Journal of Solid-State Circuits*, vol. 51, no. 1, pp. 303–309, 2016.
- [185] T. Takemoto, M. Hayashi, C. Yoshimura, and M. Yamaoka, “2.6 A 2  $\times$  30k-Spin Multichip Scalable Annealing Processor Based on a Processing-In-Memory Approach for Solving Large-Scale Combinatorial Optimization Problems,” *Digest of Technical Papers - IEEE International Solid-State Circuits Conference*, vol. 2019-Febru, pp. 52–54, 2019.
- [186] Y. Su, H. Kim, and B. Kim, “CIM-Spin: A 0.5-to-1.2V Scalable Annealing Processor Using Digital Compute-In-Memory Spin Operators and Register-Based Spins for Combinatorial Optimization Problems,” *Digest of Technical Papers - IEEE International Solid-State Circuits Conference*, vol. 2020-Febru, pp. 480–482, 2020.
- [187] S. Xie, S. R. S. Raman, C. Ni, M. Wang, M. Yang, and J. P. Kulkarni, “Ising-cim: A reconfigurable and scalable compute within memory analog ising accelerator for solving combinatorial optimization problems,” *IEEE Journal of Solid-State Circuits*, vol. 57, no. 11, pp. 3453–3465, 2022.
- [188] K. Yamamoto, K. Ando, N. Mertig, T. Takemoto, M. Yamaoka, H. Teramoto, A. Sakai, S. Takamaeda-Yamazaki, and M. Motomura, “STATICa: A 512-Spin 0.25M-Weight Full-Digital Annealing Processor with a Near-Memory All-Spin-Updates-at-Once Architecture for Combinatorial Optimization with Complete Spin-Spin Interactions,” *Digest of Technical Papers - IEEE International Solid-State Circuits Conference*, vol. 2020-Febru, no. 5, pp. 138–140, 2020.
- [189] H. Goto, K. Endo, M. Suzuki, Y. Sakai, T. Kanao, Y. Hamakawa, R. Hidaka, M. Yamasaki, and K. Tatsumura, “High-performance combinatorial optimization based on classical mechanics,” *Science Advances*, vol. 7, no. 6, pp. 1–10, 2021.

- [190] H. Goto, K. Tatsumura, and A. R. Dixon, “Combinatorial optimization by simulating adiabatic bifurcations in nonlinear Hamiltonian systems,” *Science Advances*, vol. 5, no. 4, pp. 1–9, 2019.
- [191] D. Jiang, X. Wang, Z. Huang, Y. Yang, and E. Yao, “A network-on-chip-based annealing processing architecture for large-scale fully connected ising model,” *IEEE Transactions on Circuits and Systems I: Regular Papers*, pp. 1–13, 2023.
- [192] M. Erementchouk, A. Shukla, and P. Mazumder, “On computational capabilities of Ising machines based on nonlinear oscillators,” *Physica D: Nonlinear Phenomena*, vol. 437, p. 133334, 2022.
- [193] J. Chou, S. Bramhavar, S. Ghosh, and W. Herzog, “Analog Coupled Oscillator Based Weighted Ising Machine,” *Scientific Reports*, vol. 9, no. 1, pp. 1–10, 2019.
- [194] T. Wang, L. Wu, and J. Roychowdhury, “Late breaking results: New computational results and hardware prototypes for oscillator-based ising machines,” *Proceedings - Design Automation Conference*, vol. 2019, pp. 19–21, 2019.
- [195] I. Ahmed, P. W. Chiu, W. Moy, and C. H. Kim, “A Probabilistic Compute Fabric Based on Coupled Ring Oscillators for Solving Combinatorial Optimization Problems,” *IEEE Journal of Solid-State Circuits*, vol. 56, no. 9, pp. 2870–2880, 2021.
- [196] M. K. Bashar, A. Mallick, D. S. Truesdell, B. H. Calhoun, S. Joshi, and N. Shukla, “Experimental Demonstration of a Reconfigurable Coupled Oscillator Platform to Solve the Max-Cut Problem,” *IEEE Journal on Exploratory Solid-State Computational Devices and Circuits*, vol. 6, no. 2, pp. 116–121, 2020.
- [197] M. K. Bashar, A. Mallick, and N. Shukla, “Experimental investigation of the dynamics of coupled oscillators as ising machines,” *IEEE Access*, vol. 9, pp. 148184–148190, 2021.
- [198] R. Afoakwa, Y. Zhang, U. K. R. Vengalam, Z. Ignjatovic, and M. Huang, “BRIM: Bistable Resistively-Coupled Ising Machine,” *Proceedings - International Symposium on High-Performance Computer Architecture*, vol. 2021–Febru, pp. 749–760, 2021.
- [199] A. R. Muya Chang, Xunzhao Yin, Zoltan Toroczkai, Xiaobo Hu, “An Analog Clock-free Compute Fabric base on Continuous-Time Dynamical System for Solving Combinatorial Optimization Problems,” *IEEE CICC 2022*, no. 3, pp. 4–5, 2022.

- [200] J. H. Shin, Y. J. Jeong, M. A. Zidan, Q. Wang, and W. D. Lu, "Hardware Acceleration of Simulated Annealing of Spin Glass by RRAM Crossbar Array," *Technical Digest - International Electron Devices Meeting, IEDM*, vol. 2018-Decem, pp. 3.3.1–3.3.4, 2019.
- [201] F. Cai, S. Kumar, T. Van Vaerenbergh, X. Sheng, R. Liu, C. Li, Z. Liu, M. Foltin, S. Yu, Q. Xia, J. J. Yang, R. Beausoleil, W. D. Lu, and J. P. Strachan, "Power-efficient combinatorial optimization using intrinsic noise in memristor Hopfield neural networks," *Nature Electronics*, vol. 3, no. 7, pp. 409–418, 2020.
- [202] Y. Shim, A. Jaiswal, and K. Roy, "Ising computation based combinatorial optimization using spin-Hall effect (SHE) induced stochastic magnetization reversal," *Journal of Applied Physics*, vol. 121, no. 19, 2017.
- [203] J. Kaiser and S. Datta, "Probabilistic computing with p-bits," *Applied Physics Letters*, vol. 119, no. 15, 2021.
- [204] S. Dutta, A. Khanna, and S. Datta, "Understanding the Continuous-Time Dynamics of Phase-Transition Nano-Oscillator-Based Ising Hamiltonian Solver," *IEEE Journal on Exploratory Solid-State Computational Devices and Circuits*, vol. 6, no. 2, pp. 155–163, 2020.
- [205] S. Dutta, A. Khanna, A. S. Assoa, H. Paik, D. G. Schlom, Z. Toroczkai, A. Raychowdhury, and S. Datta, "An Ising Hamiltonian solver based on coupled stochastic phase-transition nano-oscillators," *Nature Electronics*, vol. 4, no. 7, pp. 502–512, 2021.
- [206] Y. Kuramoto, "Self-entrainment of a population of coupled non-linear oscillators," in *International Symposium on Mathematical Problems in Theoretical Physics* (H. Araki, ed.), (Berlin, Heidelberg), pp. 420–422, Springer Berlin Heidelberg, 1975.
- [207] F. A. Rodrigues, T. K. D. Peron, P. Ji, and J. Kurths, "The kuramoto model in complex networks," *Physics Reports*, vol. 610, pp. 1–98, 2016.
- [208] H. Rategh and T. Lee, "Superharmonic injection-locked frequency dividers," *IEEE Journal of Solid-State Circuits*, vol. 34, no. 6, pp. 813–821, 1999.
- [209] M. Tortarolo, B. Lacoste, J. Hem, C. Dieudonné, M. C. Cyrille, J. A. Katine, D. Mauri, A. Zeltser, L. D. Buda-Prejbeanu, and U. Ebels, "Injection locking at 2f of spin torque oscillators under influence of thermal noise," *Scientific Reports*, vol. 8, no. 1, pp. 1–7, 2018.
- [210] Z. M. Zeng, P. Upadhyaya, P. Khalili Amiri, K. H. Cheung, J. A. Katine, J. Langer, K. L. Wang, and H. W. Jiang, "Enhancement of microwave emission in magnetic tunnel junction oscillators through in-plane field orientation," *Applied Physics Letters*, vol. 99, no. 3, pp. 1–4, 2011.

- [211] A. D. Belanovsky, N. Locatelli, P. N. Skirdkov, F. A. Araujo, J. Grollier, K. A. Zvezdin, V. Cros, and A. K. Zvezdin, “Phase locking dynamics of dipolarly coupled vortex-based spin transfer oscillators,” *Physical Review B - Condensed Matter and Materials Physics*, vol. 85, no. 10, pp. 1–4, 2012.
- [212] A. Ruotolo, V. Cros, B. Georges, A. Dussaux, J. Grollier, C. Deranlot, R. Guillemet, K. Bouzehouane, S. Fusil, and A. Fert, “Phase-locking of magnetic vortices mediated by antivortices,” *Nature Nanotechnology*, vol. 4, no. 8, pp. 528–532, 2009.
- [213] S. Kaka, M. R. Pufall, W. H. Rippard, T. J. Silva, S. E. Russek, and J. A. Katine, “Mutual phase-locking of microwave spin torque nano-oscillators,” *Nature*, vol. 437, no. 7057, pp. 389–392, 2005.
- [214] F. B. Mancoff, N. D. Rizzo, B. N. Engel, and S. Tehrani, “Phase-locking in double-point-contact spin-transfer devices,” *Nature*, vol. 437, no. 7057, pp. 393–395, 2005.
- [215] A. Houshang, E. Iacocca, P. Dürrenfeld, S. R. Sani, J. Åkerman, and R. K. Dumas, “Spin-wave-beam driven synchronization of nanocontact spin-torque oscillators,” *Nature Nanotechnology*, vol. 11, no. 3, pp. 280–286, 2016.
- [216] J. Grollier, V. Cros, and A. Fert, “Synchronization of spin-transfer oscillators driven by stimulated microwave currents,” *Physical Review B*, vol. 73, p. 060409, Feb 2006.
- [217] S. Urazhdin, V. Tiberkevich, and A. Slavin, “Parametric excitation of a magnetic nanocontact by a microwave field,” *Physical Review Letters*, vol. 105, p. 237204, Dec 2010.
- [218] P. Virtanen, R. Gommers, T. E. Oliphant, M. Haberland, T. Reddy, D. Cournapeau, E. Burovski, P. Peterson, W. Weckesser, J. Bright, S. J. van der Walt, M. Brett, J. Wilson, K. J. Millman, N. Mayorov, A. R. J. Nelson, E. Jones, R. Kern, E. Larson, C. J. Carey, İ. Polat, Y. Feng, E. W. Moore, J. VanderPlas, D. Laxalde, J. Perktold, R. Cimrman, I. Henriksen, E. A. Quintero, C. R. Harris, A. M. Archibald, A. H. Ribeiro, F. Pedregosa, P. van Mulbregt, and SciPy 1.0 Contributors, “SciPy 1.0: Fundamental Algorithms for Scientific Computing in Python,” *Nature Methods*, vol. 17, pp. 261–272, 2020.
- [219] A. J. Salgado and S. M. Wise, *Classical Numerical Analysis: A Comprehensive Course*. Cambridge University Press, 2022.
- [220] S. K. Lam, A. Pitrou, and S. Seibert, “Numba: A llvm-based python jit compiler,” in *Proceedings of the Second Workshop on the LLVM Compiler Infrastructure in HPC*, pp. 1–6, 2015.
- [221] LocalSolver, “Max Cut.” <https://www.localsolver.com/docs/last/exampletour/maxcut.html>, 2023. [Online; accessed 11-March-2023].

- [222] H. Fulara, M. Zahedinejad, R. Khymyn, M. Dvornik, S. Fukami, S. Kanai, H. Ohno, and J. Åkerman, “Giant voltage-controlled modulation of spin Hall nano-oscillator damping,” *Nature Communications*, vol. 11, no. 1, pp. 1–7, 2020.
- [223] F. C. Hoppensteadt and E. M. Izhikevich, “Oscillatory neurocomputers with dynamic connectivity,” *Physical Review Letters*, vol. 82, no. 14, pp. 2983–2986, 1999.
- [224] M. S. Könz, W. Lechner, H. G. Katzgraber, and M. Troyer, “Embedding overhead scaling of optimization problems in quantum annealing,” *PRX Quantum*, vol. 2, p. 040322, Nov 2021.
- [225] T. Boothby, A. D. King, and A. Roy, “Fast clique minor generation in Chimera qubit connectivity graphs,” *Quantum Information Processing*, vol. 15, no. 1, pp. 495–508, 2016.
- [226] V. Choi, “Minor-embedding in adiabatic quantum computation: I. the parameter setting problem,” *Quantum Information Processing*, vol. 7, no. 5, pp. 193–209, 2008.
- [227] W. Lechner, P. Hauke, and P. Zoller, “A quantum annealing architecture with all-to-all connectivity from local interactions,” *Science Advances*, vol. 1, no. 9, pp. 1–6, 2015.
- [228] K. Boothby, P. Bunyk, J. Raymond, and A. Roy, “Next-Generation Topology of D-Wave Quantum Processors,” tech. rep., D-Wave Systems, 2020.
- [229] K. Boothby, A. D. King, and J. Raymond, “Zephyr Topology of D-Wave Quantum Processors,” tech. rep., D-Wave Systems, 2021.
- [230] R. Hamerly, T. Inagaki, P. L. McMahon, D. Venturelli, A. Marandi, T. Onodera, E. Ng, C. Langrock, K. Inaba, T. Honjo, K. Enbutsu, T. Umeki, R. Kasahara, S. Utsunomiya, S. Kako, K. I. Kawarabayashi, R. L. Byer, M. M. Fejer, H. Mabuchi, D. Englund, E. Rieffel, H. Takesue, and Y. Yamamoto, “Experimental investigation of performance differences between coherent Ising machines and a quantum annealer,” *Science Advances*, vol. 5, no. 5, pp. 1–11, 2019.
- [231] C. song Zhou and T. lun Chen, “Chaotic annealing for optimization,” *Physical Review E - Statistical Physics, Plasmas, Fluids, and Related Interdisciplinary Topics*, vol. 55, no. 3, pp. 2580–2587, 1997.
- [232] M. Ercsey-Ravasz and Z. Toroczkai, “Optimization hardness as transient chaos in an analog approach to constraint satisfaction,” *Nature Physics*, vol. 7, no. 12, pp. 966–970, 2011.

- [233] T. Leleu, Y. Yamamoto, S. Utsunomiya, and K. Aihara, “Combinatorial optimization using dynamical phase transitions in driven-dissipative systems,” *Physical Review E*, vol. 95, no. 2, pp. 4–6, 2017.
- [234] F. Böhm, T. V. Vaerenbergh, G. Verschaffelt, and G. Van der Sande, “Order-of-magnitude differences in computational performance of analog Ising machines induced by the choice of nonlinearity,” *Communications Physics*, vol. 4, no. 1, pp. 1–11, 2021.
- [235] K. Tatsumura, M. Yamasaki, and H. Goto, “Scaling out Ising machines using a multi-chip architecture for simulated bifurcation,” *Nature Electronics*, vol. 4, no. 3, pp. 208–217, 2021.
- [236] M. J. Hasler, “Electrical Circuits with Chaotic Behavior,” *Proceedings of the IEEE*, vol. 75, no. 8, pp. 1009–1021, 1987.
- [237] A. Rodríguez-Vázquez and M. Delgado-Restituto, “CMOS Design of Chaotic Oscillators Using State Variables: A Monolithic Chua’s Circuit,” *IEEE Transactions on Circuits and Systems II: Analog and Digital Signal Processing*, vol. 40, no. 10, pp. 596–613, 1993.
- [238] J. Cruz and L. Chua, “A cmos ic nonlinear resistor for chua’s circuit,” *IEEE Transactions on Circuits and Systems I: Fundamental Theory and Applications*, vol. 39, no. 12, pp. 985–995, 1992.
- [239] E. Tamaševičiūtė, A. Tamaševičius, G. Mykolaitis, and S. Bumelienė, “Analogue Electrical Circuit for Simulation of the Duffing-Holmes Equation,” *Nonlinear Analysis: Modelling and Control*, vol. 13, no. 2, pp. 241–252, 2008.
- [240] J. Kengne and F. Kenmogne, “On the modeling and nonlinear dynamics of autonomous Silva-Young type chaotic oscillators with flat power spectrum,” *Chaos*, vol. 24, no. 4, 2014.
- [241] F. Moon and P. Holmes, “A magnetoelastic strange attractor,” *Journal of Sound and Vibration*, vol. 65, no. 2, pp. 275–296, 1979.
- [242] P. H. John Guckenheimer, *Nonlinear Oscillations, Dynamical Systems, and Bifurcations of Vector Fields*, vol. 1. Springer New York, NY, 2013.
- [243] F. Moon, *Nonlinear Dynamics*, vol. 3. Encyclopedia of Physical Science and Technology, Elsevier Science Ltd., 2003.
- [244] H. Goto, “Bifurcation-based adiabatic quantum computation with a nonlinear oscillator network,” *Scientific Reports*, vol. 6, pp. 1–8, 2016.

